ESPOO 2004 VTT PUBLICATIONS 553

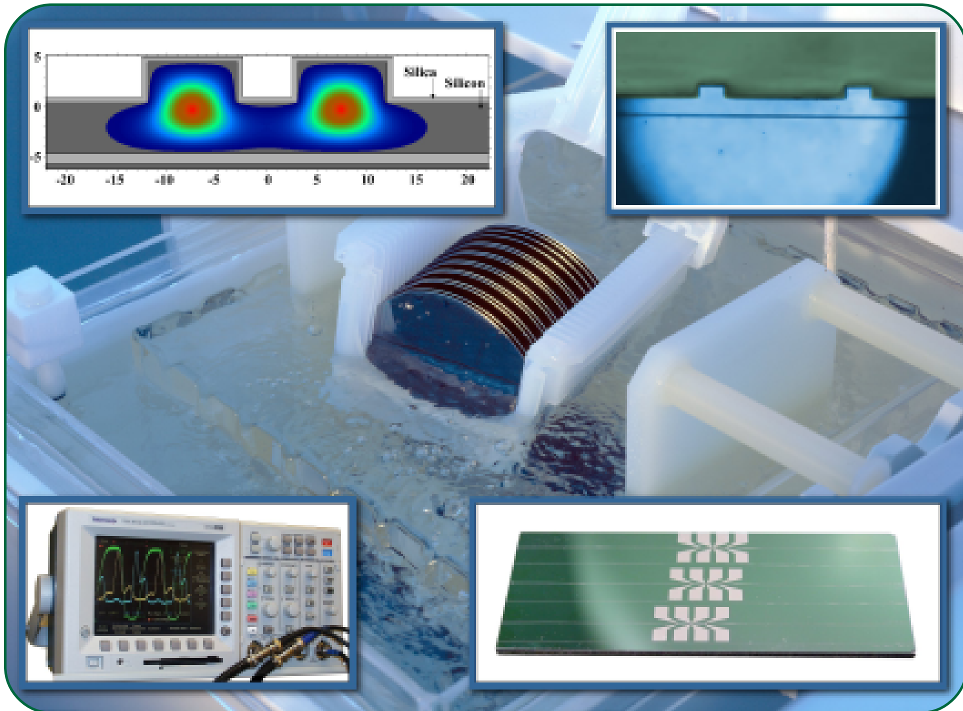

Timo Aalto

Microphotonic silicon waveguide components

VTT PUBLICATIONS 553

Microphotonic silicon waveguide components

Timo Aalto

VTT Information Technology

Dissertation for the degree of Doctor of Science in Technology to be presented with due permission of the Department of Electrical and Communications Engineering for public examination and debate in Auditorium AS1 at Helsinki University of Technology (Espoo, Finland) on the 10th of December, 2004, at 12 o'clock noon.

ISBN 951–38–6422–7 (soft back ed.)
ISSN 1235–0621 (soft back ed.)

ISBN 951–38–6423–5 (URL: http://www.vtt.fi/inf/pdf/)
ISSN 1455–0849 (URL: http://www.vtt.fi/inf/pdf/)

Copyright © VTT 2004

JULKAISIJA – UTGIVARE – PUBLISHER

VTT, Vuorimiehentie 5, PL 2000, 02044 VTT
puh. vaihde (09) 4561, faksi (09) 456 4374

VTT, Bergsmansvägen 5, PB 2000, 02044 VTT
tel. växel (09) 4561, fax (09) 456 4374

VTT Technical Research Centre of Finland, Vuorimiehentie 5, P.O.Box 2000, FIN–02044 VTT, Finland
phone internat. + 358 9 4561, fax + 358 9 456 4374

VTT Tietotekniikka, Tietotie 3, PL 1208, 02044 VTT
puh. vaihde (09) 4561, faksi (09) 456 7012

VTT Informationsteknik, Tietotie 3, PB 1208, 02044 VTT
tel. växel (09) 4561, fax (09) 456 7012

VTT Information Technology, Tietotie 3, P.O.Box 1208, FIN–02044 VTT, Finland
phone internat. + 358 9 4561, fax + 358 9 456 7012

Technical editing Leena Ukskoski

Otamedia Oy, Espoo 2004

Aalto, Timo. Microphotonic silicon waveguide components. Espoo 2004. VTT Publications 553. 78 p. + app. 73 p.

Keywords silicon microphotonics, integrated optics, silicon-on-insulator waveguides, SOI waveguides, waveguide bends, thermo-optical switching, multi-step patterning, polarisation maintaining fibers, polarisation extinction ratio

Abstract

This thesis describes the design, simulation, fabrication and characterisation of microphotonic silicon waveguide components on silicon-on-insulator (SOI) substrates. The focus is on approximately 10 µm thick and single-moded (SM) silicon rib waveguides. In particular, simulation results are given for straight and bent Si waveguides, directional couplers (DCs), thermo-optically (TO) modulated Mach-Zehnder interferometers (MZI), and waveguide gratings. A new analytical SM condition for Si rib waveguides is proposed and the development of a new grating simulation algorithm is reported. The theoretical part of the work also involves inventions relating to multi-step patterning of Si waveguides, modulation of interferometric devices, and measurement of polarisation axes from waveguides and polarisation maintaining (PM) fibers.

Clean room processing of waveguide chips is briefly described. Main process steps are photolithography, electron-beam lithography, thermal oxidation, oxide deposition, oxide dry etching and Si dry etching. Post-processing of the chips is also reported, including dicing, polishing, anti-reflection (AR) coating, fiber pigtailing and wire bonding. The development of fabrication processes for multi-step patterning, waveguide gratings and photonic crystal waveguides is reported, although the optical characterisation of devices based on these three processes is not included in the thesis.

Experimental results are given for Si rib waveguides with different thicknesses (H) and widths (W). The minimum fiber coupling loss with H = 9 µm was 1.3 dB/facet without an AR coating. The AR coating reduced the coupling loss by 0.7–0.8 dB/facet. Minimum propagation loss for a 114 cm long waveguide spiral with H = 9 µm and W = 7 µm was 0.13 dB/cm. With H = 9 µm, the birefringence varied from 0.00063 to <0.0001 depending on the cladding material, and the maximum polarisation extinction ratio for straight waveguides and directional couplers was >15 dB. Furthermore, fast modulation with 15 dB extinction ratio (ER) is reported for TO MZI switches by using both traditional (10 kHz) and novel (167 kHz) modulation methods. Rise and fall times for single switching operations were pushed below 750 ns with 9 dB ER. The setups and methods used in measurements are described in detail, including a novel method for measuring the polarisation axes of waveguides and PM fibers.

Preface

The work presented in this thesis was carried out during the years 1997–2004 at the Technical Research Centre of Finland (VTT) in Espoo, Finland. The name and the organisational status of the author's research group have changed more than once during this time. Presently it is called the Photonics group and it belongs to the Microelectronics research area of VTT Information Technology.

Most of the research work was performed in HILA, ELEOPTO-OPTIMI, OKSIDI and SOIWAVE projects. I thank the Academy of Finland, the European Space Agency (ESA), Tekniikan Edistämissäätiö and VTT for funding these projects and enabling my research work.

I thank my supervisor and former group leader at VTT, Prof. Matti Leppihalme, for encouraging and supporting me in my work during all these years. My present group leader Päivi Heimala deserves special compliments for originally introducing me to this fascinating research field and for conducting most of the actual clean room fabrication in this work. I also wish to express my gratitude to the former and present leaders of the Microelectronics Centre, Dr. Jouni Heleskivi and Dr. Ilkka Suni, for their interest and support in my research.

All my coauthors in the eight original publications helped me to build a solid foundation for this thesis, which is highly appreciated. I am particularly grateful to Mikko Harjanne for his invaluable help in simulations, image processing, programming, and electronics construction, as well as for his comments on the manuscript, and for our fruitful discussions. The work of Markku Kapulainen and Kimmo Solehmainen in device characterisation and clean-room fabrication, and their comments on the manuscript, is greatly acknowledged. The contributions from my former colleagues Sanna Yliniemi and Pekka Katila, and the collaborators from the University of Joensuu, are appreciated. I would also like to thank all my present and former colleagues at VTT for providing a pleasant working environment and for making numerous small contributions to my work.

I thank Dr. Ari Tervonen from Nokia Research Center and Dr. Jyrki Saarinen from Heptagon for carefully pre-examining the manuscript.

I thank all my friends and relatives for encouraging me in this work and for sometimes taking my thoughts out of this work. The latter applies particularly well to my two sons, Jaakko and Ville, with whom I wish to spend more time after the hectic finishing of the manuscript. Finally, I thank my beloved wife Maarit for standing besides me all these years and for her patience and support during this work.

Timo Aalto
Espoo, November 14, 2004

Contents

Abstract 3
Preface 4
Contents 5
List of original publications 7
Author's contribution 9
List of symbols and abbreviations 11
1. Introduction 15
1.1 Historical perspective 15
1.2 Silicon technology 15
1.3 Silicon microphotonics 18
1.4 Silicon-on-insulator (SOI) waveguide technology 21
1.5 Aims of the thesis 24
1.6 Organisation of the thesis 24
2. Theory, simulation and design 25
2.1 Electromagnetic theory of waveguides 25
2.2 Straight waveguides 27
2.3 Optical coupling of fibers and silicon waveguides 34
2.4 Bends and mirrors in Si waveguides 36
2.5 Directional couplers and interferometric switches 39
2.6 Multi-step patterning of silicon waveguides 43
2.7 Waveguide gratings 45
2.8 Polarisation cross-talk 46
3. Fabrication 49
3.1 Clean-room processing 49
3.2 Post-processing and fiber pigtailing 52
3.3 Waveguide gratings and photonic crystal structures 53
4. Experimental results 55
4.1 Construction of the measurement set-ups 55
4.2 Optical coupling of fibers and silicon waveguides 56
4.3 Propagation and bending losses of silicon waveguides 59
4.4 Polarisation characteristics of Si waveguides and directional couplers 61
4.5 Fast thermo-optic 2x2 MZI switch 63
5. Conclusions 67
References 69
Appendix A: Simulation tools
Publications I–VIII

Appendices II, III and VII of this publication are not included in the PDF version. Please order the printed version to get the complete publication (http://www.vtt.fi/inf/pdf/)

List of original publications

This thesis includes the following selection of publications, which are referred to in the text by Roman numerals I–VIII and briefly described below. Additional unpublished data is also presented.

I T. Aalto, M. Harjanne, M. Kapulainen, P. Heimala, and M. Leppihalme, "Development of silicon-on-insulator waveguide technology", Photonics West 2004, San Jose, USA, 26–29 January 2004. *Proceedings of SPIE*, Vol. 5355, pp. 81–95, 2004.

II M. Harjanne, T. Aalto, "Design of tight bends in silicon-on-insulator ridge waveguides", *Physica Scripta*, Vol. T114, pp. 209–212, 2004.

III T. Aalto, P. Heimala, and P. Katila, "Integrated optical switch based on SOI-technology", *Physica Scripta*, Vol. T79, pp. 123–126, 1999.

IV T. Aalto, M. Kapulainen, S. Yliniemi, P. Heimala, and M. Leppihalme, "Fast thermo-optical switch based on SOI waveguides", Photonics West 2003, San Jose, USA, 27–29 January, 2003. *Proceedings of SPIE*, Vol. 4987, pp. 149–159, 2003.

V M. Harjanne, M. Kapulainen, T. Aalto, and P. Heimala, "Sub-µs switching time in silicon-on-insulator Mach–Zehnder thermooptic switch", *Photonics Technology Letters*, Vol. 16, No. 9, pp. 2039–2041, 2004.

VI J. Tervo, M. Kuittinen, P. Vahimaa, J. Turunen, T. Aalto, P. Heimala, and M. Leppihalme, "Efficient Bragg waveguide-grating analysis by quasi-rigorous approach based on Redheffer's star product", *Optics Communications*, Vol. 198, pp. 265–272, 2001.

VII P. Heimala, T. Aalto, S. Yliniemi, J. Simonen, M. Kuittinen, J. Turunen, and M. Leppihalme, "Fabrication of Bragg grating structures in silicon", *Physica Scripta*, Vol. T101, pp. 92–95, 2002.

VIII T. Aalto, M. Harjanne, and M. Kapulainen, "Method for the rotational alignment of polarization-maintaining optical fibers and waveguides", *Optical Engineering*, Vol. 42, Issue 10, pp. 2861–2867, 2003.

Publication I covers the majority of the results obtained in the entire work. It starts with an introduction to slab-, strip-, and rib-types of Si waveguides, followed by simulation results for the single-mode limits and bending losses in rib waveguides. Experimental results are then given for the polarisation properties of rib waveguides and for thermo-optical switching. Finally, the multi-step patterning principle is proposed.

Publication II presents simulation results for bent Si rib waveguides with three thicknesses and with an optional groove. The results demonstrate the ability to significantly reduce the bending radius by using smaller waveguides or additional grooves. Numerical S-bend optimisation is also described.

Publication III presents the design and simulation of a thermo-optical switch based on Si rib waveguides in a 2×2 Mach–Zehnder interferometer layout. This early work led to a mask layout used to fabricate all the thermo-optical switches reported in this thesis.

Publication IV presents experimental results for the thermo-optical switch and introduces a novel modulation principle. Some introduction and background to optical switching is also given, and the switch fabrication is described in detail. Experimental results are presented for both traditional modulation (up to 10 kHz) and the new type of modulation (up to 167 kHz). Compromises of speed vs. power consumption are discussed.

Publication V presents the application of the novel modulation principle to the minimisation of single rise- and fall-times in a thermo-optical switch. The new method and the improved control electronics are described. Results with the traditional (rise- and fall-times 29–35 μs) and new modulation method (rise- and fall-times 0.7–0.73 μs) are given.

Publication VI introduces a computationally efficient, quasi-rigorous simulation method developed for the design of etched gratings on top of Si rib waveguides. Thorough description of the new method and a comparison to a traditional film-stack method are given. The new method is particularly useful for analysing deep gratings and the coupling of light between different waveguide modes.

Publication VII describes the fabrication of Si rib waveguides and grating structures. The design and simulation of gratings are summarised and the fabrication of rib waveguides is described. Then the fabrication of gratings on Si substrates by using electron-beam lithography and dry etching is reported. Finally, the process combination and the realisation of waveguide gratings and other nanostructures on top of waveguides is discussed.

Publication VIII introduces a novel method for measuring the rotational angle of a fiber's or a waveguide's polarisation axis. Alignment needs in polarisation maintaining (PM) optical systems, alternative methods and a detailed theory of the new method are described. Experimental results indicate an angular accuracy better than ±0.2°. The new method can be used e.g. to rotationally align PM fibers with respect to Si waveguides.

Author's contribution

The results presented in this thesis were obtained in collaboration with several other persons from VTT, the Helsinki University of Technology and the University of Joensuu. The author has written publications I, III, IV and VIII. He has participated actively in the writing of publications II and V, and somewhat in the writing of publications VI–VII. The author has been responsible for the overall guidance of work reported in publications I–II, IV–V and VIII, and participated in the guidance of work reported in publications III, VI and VII.

The author was responsible for the theory, simulation and design of all the waveguide components reported in publications I and III–V. He carried out all the simulations for these publications by himself, except for the bend simulations in publication I. In publication II, the author actively guided the work and participated in the writing of the paper, although most of the simulations were not carried out by him. He proposed the multistep patterning of silicon waveguides (publications I and II). He invented the new modulation principle and the new rotational alignment method, which are described and demonstrated in publications I, III–V, and VIII. He also designed all the lithographic masks (device layouts) used in the fabrication. In publications VI–VII, the author defined the target structures for simulation and fabrication, calculated the effective indices, and analysed the validity of the new simulation tool for this work. In publication VIII the author was responsible for all theoretical aspects.

With respect to fabrication (publications I, IV, and VII), the author typically had a smaller role and was not responsible for the actual clean-room fabrication. Nevertheless, he usually defined the targets for waveguide structures and processes, and suggested several new processing methods. He had a central role in the development of waveguide grating processes (publication VII) and post-processing steps (dicing, polishing, AR-coating, and wire bonding).

The author had a significant role in all measurements (I and VIII) and thermo-optical switching experiments (publications III–V). Many of them were actually carried out by others, but the author had a substantial impact in the guidance of all measurements, in the numerical post-processing of measured raw data, and particularly in the development of measurement and switching methods.

List of symbols and abbreviations

c	Speed of light in vacuum
c_1	Numerical variable for the proposed new SM limit (default -0.1)
d_{AR}	Thickness of a single-layer antireflection coating
$\boldsymbol{E}$	Electric field vector
h	Thickness of the silicon slab surrounding a rib
H	Waveguide thickness (total silicon thickness at the location of rib)
$\boldsymbol{H}$	Magnetic field vector
I	Intensity of light
n	Refractive index of a material
n_0	Refractive index of waveguide cladding (usually 1–1.5, default 1.46)
n_{AR}	Refractive index of a single-layer antireflection coating
n_{gap}	Refractive index of a material in a gap between a fiber and a waveguide
n_{Si}	Refractive index of silicon (3.48)
N	Number of propagating waveguide modes
n_{eff}	Effective index of a waveguide mode
P	Heating power (P_1 and P_2 for waveguides 1 and 2, respectively) or optical power (P_1 and P_2 for two orthogonal polarisations)
P_{ON}	Heating power needed for an ON state when only one heater is used
P_{bias}	Heating power used for both waveguides in a biased OFF state
Q	Correction term for the Soref's SM limit (Q_{TE} for TE and Q_{TM} for TM)
r	1/e field radius of a gaussian field (r_1 and r_2 for fields 1 and 2, respectively) or ratio of real and ideal directional coupler length (for 50:50 operation)
r_{SMF}	1/e field radius of a SM fiber (default 5 μm)
R	Bending radius
s	Fraction of input power for a 2×2 MZI that is always divided equally to both outputs e.g. due to scattering
$\boldsymbol{S}$	Poynting vector
T_{BAR}	Relative output power (or transmission for lossless operation) from the bar port of a 2×2 MZI (i.e. $1-T_{CROSS}$)
T_{CROSS}	Relative output power (or transmission for lossless operation) from the cross port of a 2×2 MZI ($T_{CROSS,min}$ and $T_{CROSS,max}$ are the minimum and maximum when $\Delta\phi$ is varied, $T_{CROSS,ideal}$ corresponds to an ideal directional coupler with r = 1, s = 0)

W	Waveguide (rib) width
W_{10}	Proposed new width limit for eliminating higher order vertical modes in rib waveguides
W_{SM}	Proposed new width limit for SM rib waveguides
W_{Soref}	Soref's width limit for thick SM rib waveguides
$W_{\mathrm{Soref,Q}}$	Soref's more accurate width limit for SM rib waveguides
x	Horizontal coordinate (along chip surface)
y	Vertical coordinate (perpendicular to chip surface)
z	Longitudinal coordinate (along waveguide axis)

α	Rotational angle (e.g. in a rotational junction or for a rotatable polariser) or deflection angle in a waveguide mirror
$\Delta\phi$	Phase difference between two waveguides or polarisation modes
Δn	Refractive index difference between a waveguide core and its cladding
Δn_{eff}	Effective index difference in a waveguide grating (groove vs. no groove)
$\Delta\rho$	Radial misalignment in a fiber-waveguide junction
ΔT	Temperature difference between two waveguide branches
Δz	Longitudinal misalignment in a fiber-waveguide junction
ε	Permittivity
ε_0	Vacuum permittivity
η	Coupling coefficient between two electro-magnetic fields
κ	Coupling coefficient in a fiber-waveguide junction when $\theta_\rho = \Delta\rho = 0$
λ	Wavelength in vacuum (default 1550 nm)
μ	Permeability
μ_0	Vacuum permeability
θ_ρ	Angular misalignment in a fiber-waveguide junction (around $\Delta\rho$)
θ_x	Angular misalignment in a fiber-waveguide junction (around x)
θ_y	Angular misalignment in a fiber-waveguide junction (around y)
Ψ	Arbitrary component of an electro-magnetic field

1D	One-dimensional (2D and 3D for two- and three-dimensional)
ALD	Atomic layer deposition
AR	Anti-reflection
AWG	Arrayed waveguide grating
BESOI	Bond and etch-back SOI

BiCMOS	Bipolar complementary metal oxide semiconductor
BOX	Buried oxide (between silicon substrate and silicon core)
BPM	Beam propagation method
CVD	Chemical vapour deposition
CMOS	Complementary metal oxide semiconductor
DC	Directional coupler
Det.	Detector
DUT	Device under test (sample)
EDFA	Erbium doped fiber amplifier
EIM	Effective index method
ELTRAN	Epitaxial layer transfer (SOI wafer)
ER	Extinction ratio (ratio of the two output powers from a 2×2 MZI)
ER_{ideal}	Extinction ratio for an ideal 2×2 MZI (assuming r = 1, s = 0)
FDTD	Finite difference time domain
ICP	Inductively coupled plasma
IL	Insertion loss
JoFy	Department of Physics at the University of Joensuu
IC	Integrated circuit
IR	Infrared
LED	Light emitting diode
LTO	Low temperature oxide
LWC	Line width change with respect to a nominal width on a mask
MEMS	Micro-electro-mechanical-system
MM	Multi-moded
MMF	Multi-moded fiber
MMI	Multi-mode interference
MZI	Mach–Zehnder interferometer
PDL	Polarisation dependent loss
PhC	Photonic crystal
PIC	Photonic integrated circuit
PM	Polarisation maintaining
PMD	Polarisation mode dispersion
PMF	Polarisation maintaining fiber
PXR	Polarisation extinction ratio (PXR_{in} and PXR_{out} for input and output, respectively)

RIE	Reactive ion etching
SEM	Scanning electron microscope
SIMOX	Separation by implanted oxygen (SOI wafer)
SM	Single-moded
SMF	Single-mode fiber
SOI	Silicon-on-insulator
TEOS	Tetraethyl orthosilicate
TIR	Total internal reflection
TE	Transverse electric (**E** horizontally with respect to the Si chip)
TE_{XY}	TE polarised waveguide mode with X+1 and Y+1 intensity maxima in the x- and y-directions, respectively
TM	Transverse magnetic (**E** vertically with respect to the Si chip)
TM_{XY}	TM polarised waveguide mode with X+1 and Y+1 intensity maxima in the x- and y-directions, respectively
TO	Thermo-optical
TOX	Thermal oxide
UV	Ultraviolet

1. Introduction

1.1 Historical perspective

The entire technological history of mankind can be divided into four material eras. Each of them is associated with a certain material that people learned to find or fabricate, to process by different tools and methods, and to finally turn into useful products. The adoption of each material led to a significant technological progress. The first three eras were the *Stone Age* (2,000,000–3000 BC), the *Bronze Age* (3000–1200 BC), and the *Iron Age* (1200 BC – 1950 AD). The *Industrial Revolution* was the capstone of the *Iron Age*. The machines, tools, bridges, ships, trains, cars, airplanes etc. made from iron let us move easily from one place to another and provided us a multitude of new mechanical products for our everyday life. The huge leaps in fabrication technology that followed the introduction of iron, and its important derivative material, steel, have now mostly passed and we have entered a new era. The first impression might be that in our present information society the technology has become immaterial or that it is based on a variety of equally important materials. However, this is not the case.

The fourth and present era can be called the *Silicon Age* (1950–). It started from the first silicon transistor demonstrations at around 1950 and it probably continues for at least two decades more. Silicon provided us the ability to build intelligent machines, supplemented our own limited capacity for numerical calculations, and enabled us to communicate easily with anybody and anywhere. The present time is sometimes also called the Communication Age or the Information Age. However, based on the central role of silicon in the overwhelmingly fast technological development during the past fifty years, as well as in the foreseeable future, it is quite reasonable to call it the *Silicon Age*.

1.2 Silicon technology

What makes silicon so special? So far, it has been its semiconductor character. Single-crystal silicon is a semiconductor by nature, but by oxidation and doping with impurity atoms (typically boron or phosphorus) one can radically change its electrical properties, in particular its resistivity. The amount and type of impurity atoms (n- or p-type) determines the amount and type of free carriers (electrons or holes) that conduct electrical charges in silicon. Under the influence of an electric field, a deficiency of electrons, i.e. holes, can conduct charges just as well as a surplus of electrons. In a technology called *Silicon Microelectronics*, the ability to control the doping permits the formation of transistors, diodes and resistors. By combining these fundamental building blocks in various ways it is possible to realise integrated circuits (ICs), the functional parts of silicon microchips that exist inside almost every modern electronic product (see Fig. 1).

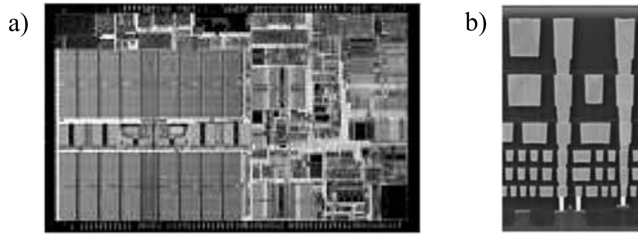

Figure 1. Microelectronic 0.13 µm CMOS technology: a) A Pentium III processor chip [1] and b) a magnified cross-section of a chip with six metal layers [2].

As predicted by Gordon Moore in 1965 [3] and seen from Fig. 2, the number of transistors on a single IC chip has grown exponentially, and is presently over 500 million. At the same time, the minimum process linewidth has reduced exponentially, and is now 0.13 µm. There are three main variations of IC technology, namely the bipolar technology, complementary metal oxide semiconductor (CMOS) technology and their combination (BiCMOS). Furthermore, a recent variation is the use of silicon-on-insulator (SOI) wafers instead of plain silicon substrates. The use of SOI can increase the speed and reduce the power consumption of IC chips. As a whole, it is predicted that the sales of the microelectronics industry will grow from $163 billion in 2003 to $219 billion in 2006 [4: Preface, 5]. At least so far, silicon microelectronics has been the main technology driver of the *Silicon Age*.

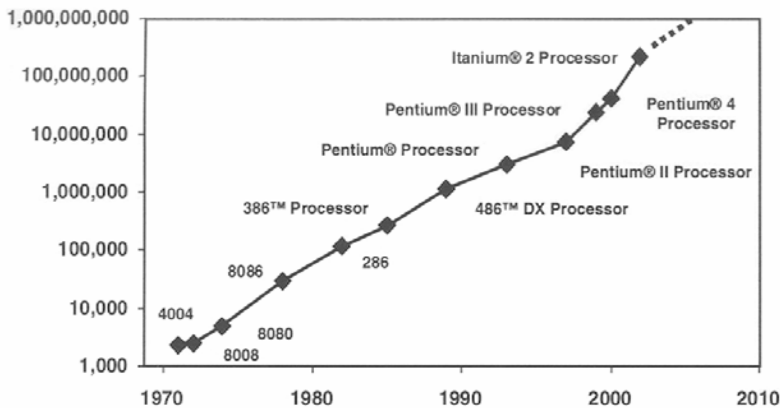

Figure 2. Number of transistors on a single silicon chip as a function of time since 1970. At 2004 the number is over 500 million. [6]

During the past few years, the mechanical characteristics of silicon have also been exploited in many applications. Silicon is at the same time resilient, hard and stiff material. Thus, it can be used to form static and moving structures in very small size and with excellent endurance. As a whole, the technology involving the realisation of miniaturised

beams, membranes, springs, resonators (see Fig. 3a), microfluidistic channels (see Fig. 3b), micromotors etc. in silicon, is called *Silicon Micromechanics* [7–12], also known as silicon micro-electro-mechanical-system (MEMS) technology. It has grown fast and it plays an important role in the miniaturisation and cost reduction of numerous products, such as oscillators, microphones, mobile phones, radios, scanners, ink jet printers, inertial sensors and diagnostic equipment for health care.

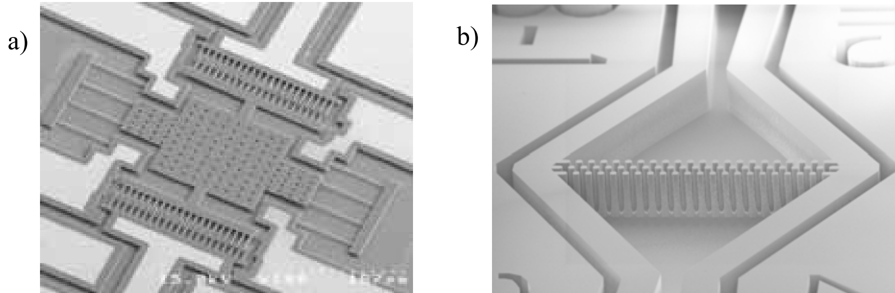

Figure 3. Micromechanical silicon chips. a) SiC microresonator on Si [9]. b) Microfluidic particle filter (etch depth ~0.5 mm) fabricated at VTT.

The third, and so far last, sector of silicon technology is called *Silicon Microphotonics*. It involves the realisation of optical functions on silicon chips (see Fig. 4) and it has been studied actively since the early 1990's. Much progress has been made, but the research efforts have been smaller than those in silicon micromechanics, and negligible compared to silicon microelectronics. Thus, silicon microphotonics is still in its infancy and has many technical challenges to tackle. Recent advancement has been very fast, which indicates a potential to solve the remaining problems and to commercialise the technology in larger scale. This makes silicon microphotonics a very attractive research subject.

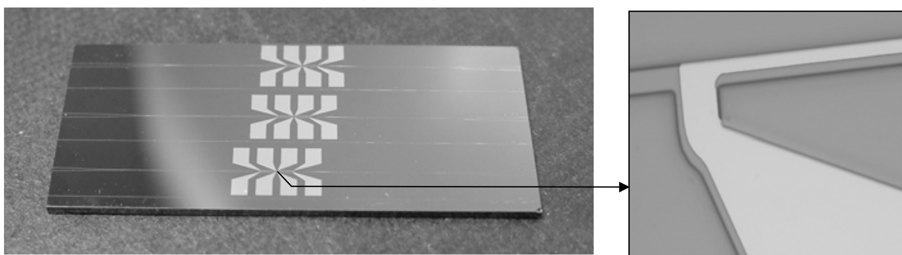

Figure 4. A simple silicon microphotonic chip (~30×12 mm^2) including three thermo-optic 2×2 switches, and a detail of a thin-film heater on top of a Si waveguide.

The success of silicon is not based only on its material characteristics, but on the combination of its availability, cost, processability and compatibility with other materials. Raw silicon can be easily extracted from silica sand, which is readily available throughout our planet. With the help of a single-crystal seed, a large single-crystal Si rod can be slowly

pulled out of melted silicon. Desired type and amount of doping can be accurately obtained by adding impurities, such as phosphorus or boron, into the melted silicon. The cooled Si rod can be sawn and polished into wafers, which form the substrates for further processing. Typical wafers are 0.5–0.8 mm thick and 100 to 400 mm in diameter (4–16"). The realisation of microelectronic, micromechanical and microphotonic components on Si wafers is usually carried out in a clean room, i.e. in an ultra-clean facility. Typical processing steps are the deposition of metallic and dielectric thin films, lithographic patterning of photo-sensitive resist layers, ion implantation, diffusion of impurity atoms into silicon, thermal oxidation of Si to produce silicon dioxide (SiO_2), wet etching with liquid chemicals and dry etching by ion bombardment. The strength of Si technology is that standard processes and tools are used to fabricate chips for numerous applications in very large quantities and with excellent yield. Huge research and development efforts carried out during the past fifty years have made silicon microelectronics a mature, reliable and cost-effective technology that has not been challenged by any other technology. Its continuing progress and recent roadmaps for IC technology indicate that this situation will remain at least for two decades more [5].

The development of silicon micromechanics and microphotonics has the clear advantage and justification in that it can use a mature microelectronics fabrication technology as a platform. Further on, it can extend the *Silicon Age* by offering new Si-based solutions for various non-electronic applications, and by enabling the unique opportunity of monolithic integration for microelectronics, micromechanics and microphotonics on a single chip. Some examples of attractive monolithic integration technologies are 1) optical clock distribution, signalling or computing carried out within a single Si chip [13], 2) integration of ICs to support microphotonic [14] and 3) micromechanical components [11], and 4) integration of optical waveguides or control electronics with microfluidic channels in optical diagnostics [15]. Further motivation for studying Si technologies can be found e.g. from recent review books written about silicon-based microfabrication [16], microelectronics [17], micromechanics [12] and microphotonics [4].

1.3 Silicon microphotonics

Silicon Microphotonics is a technology involving Si-based generation, conduction, manipulation and detection of light in microscopic scale. As electrons and photons are the basic elements of electricity and light, it is the optical equivalent of silicon microelectronics. Electrons propagate along regions of high electrical conductivity, while photons propagate along regions of high refractive index. In silicon microphotonics, optical waveguides correspond to electrical wires, as they propagate light from one place to another. Similarly, photonic integrated circuits (PICs) correspond to electrical ICs. Some of the passive building blocks for PICs are optical couplers, splitters, wavelength filters and wavelength multiplexers. Optoelectronic components, such as lasers, light emitting diodes (LEDs), detectors, switches and modulators act as a bridge between optical and

electronic signals. Optical amplifiers can boost attenuated optical signals and, thus, compensate for the losses associated with non-ideal components and power splitters. If optical transistors, wavelength converters and other all-optical components based on nonlinear phenomena will be successfully commercialised in the future, they may enable extremely fast optical computing and all-optical, packed-switched fiber-networks.

In order to use the term silicon microphotonics, one must realise some key components onto silicon substrates. The direct fabrication of different components onto a common Si substrate is called monolithic integration. Correspondingly, the attachment of separate components (fibers, chips etc.) to Si devices is called hybrid integration [18]. Today, fast modulators, light sources, amplifiers, detectors and most other optoelectronic components can be made more efficient and low-cost by using other materials, such as lithium niobate [18: pages 9–20] or III–V compound semiconductors [18: pp. 161–238]. Therefore, their integration with Si PICs is presently easier with hybrid methods.

In hybrid integration and when attaching (pigtailing) optical fibers to Si chips, the optical coupling between optical sub-components is of significant importance, especially when dealing with single-moded (SM) optical systems, as was done in this thesis. Single-mode optics is much more sensitive to misalignments than electronics. Transverse and angular misalignments between two SM sub-components should preferably be kept below 1 μm and 1°, respectively. In SM hybrid products, the tedious assembly work dominates the overall costs and limits the commercialisation. Therefore, mass-production should be based on passive or automated alignment, or monolithic integration. For some applications, such as short-range interconnections, multi-moded (MM) optics may also be used. Examples of hybrid integration are illustrated in Fig. 5.

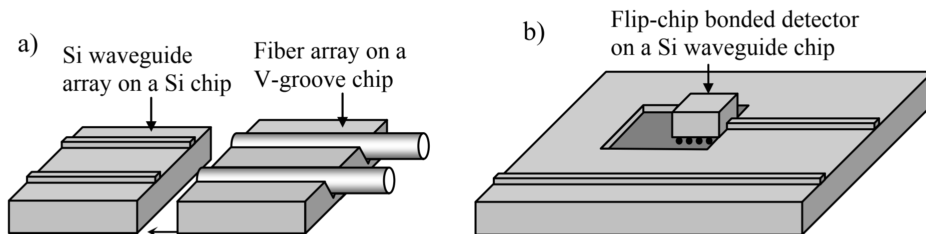

Figure 5. Examples of optical hybrid integration on silicon: a) fiber pigtailing of a Si waveguide array and b) flip-chip bonded detector on a Si chip.

Silicon microelectronics and micromechanics are not based on silicon alone, but they also involve many other materials, including various metals and dielectrics. Correspondingly, the fabrication and monolithic integration of photonic components on Si does not require that the components are made of silicon, but they may as well be made of silicon-compatible materials added on top of a Si wafer. The rest of this chapter briefly

describes the main techniques used for photonic device fabrication and monolithic integration on silicon substrates.

Waveguides can be made of silicon itself, e.g. by using the SOI waveguide technology (see Chapter 1.4) or differently doped silicon layers [19, 20]. Even in the case of SOI waveguides, the silicon core (refractive index $n = n_{Si} \approx 3.5$) is typically surrounded by other materials, such as thermal oxide (TOX, SiO_2, $n \approx 1.5$). Several types of so-called glass waveguides have also been fabricated on silicon (and glass) substrates by doping SiO_2 with impurity materials, such as As, B, Ge, N, P, Ti, or their combinations [15, 18, 21–25]. Examples of other Si-compatible waveguide materials are e.g. silicon nitride (Si_3N_4, $n \approx 2$) [26–28] and polymers [18]. Different waveguide materials are favoured for different applications and wavelengths, because each material has its own advantages and drawbacks.

The realisation of light sources and optical amplifiers on Si substrates has been investigated by using surface-textured bulk silicon (wavelength $\lambda < 1250$ nm) [29], Si nanocrystals ($\lambda < 1200$ nm) [30–32], erbium-doped Si [33] or SiO_x ($\lambda \approx 1550$ nm) [18, 34], the combination of Er and Si nanocrystals ($\lambda \approx 1550$ nm) [35, 36], Si/SiGe quantum cascade structures ($\lambda \approx 7$ µm) [37], Raman scattering ($\lambda \approx 1550$ nm) [38–40], and organic materials (λ up to 1550 nm) [41, 42]. Several breakthroughs have been made during the last four years and Si nanocrystals have even indicated stimulated emission [30, 31, 43, 44], the necessity for a silicon laser. Wavelength conversion has also been demonstrated in Si by using stimulated Raman scattering [40, 45]. Despite the promising results, the Si-based generation, amplification and wavelength conversion of light are still the greatest challenges in silicon microphotonics. Especially at wavelengths around 1550 nm, an efficient and reliable Si-based transmitter is still to be developed.

Silicon-based photodetectors have also been studied by using different approaches. Detectors for visible wavelengths can be fabricated from Si by using standard bipolar [14] and BiCMOS processes [46–48], or by using modified processes [49, 50]. Fast (>2 Gb/s) operation has been demonstrated with good responsivity (0.11 A/W) and low voltage (2 V) [51]. A potential mass market for Si detectors at visible wavelengths is in optical disc drives [46]. For near-infrared (IR) detectors operating e.g. at $\lambda = 1300$–1550 nm, the material of choice is epitaxial germanium on silicon. Unlike Si, Ge absorbs IR light. It is also compatible with Si technology, although the 4% lattice mismatch between Si and Ge somewhat hinders their monolithic integration. For the fabrication of photodetectors on Si, germanium has been introduced as thin Ge layers [52–54], Si/SiGe superlattices [55–58] and Ge islands [55, 59, 60]. Some modest results have also been reported from Er-doped SOI waveguide detectors ($\lambda \approx 1550$ nm) [61]. The latest results with Ge at $\lambda \approx 1550$ nm have shown fast operation (>2 Gb/s), good responsivity (0.75 A/W) and low voltage (<1 V) [52], thus making monolithic near-IR detectors on Si already competitive with hybrid solutions.

1.4 Silicon-on-insulator (SOI) waveguide technology

In silicon microphotonics, silicon can be used not only as a substrate, but also as a waveguide core material [I–VII, 4, 62–70]. The most straightforward way is to use silicon-on-insulator wafers, as was done in this work. They typically involve a thin SOI layer (i.e. a device layer) of single-crystal silicon on top of a Si substrate, with a thin buried oxide (BOX, SiO_2) layer between them. SOI wafers are also used in microelectronics and micromechanics, although the optimum resistivity and thickness of the SOI layer, as well as the optimum BOX thickness, often vary between different applications.

There are four main variations in the fabrication of commercial SOI wafers. So-called SIMOX (separation by implanted oxygen) wafers are based on oxygen implantation to plain Si wafers [71, 72]. They have SOI and BOX thicknesses <500 nm. This limits their applicability in microphotonics, although they are widely used in microelectronics [73]. In a so-called "Smart-Cut" process [71, 74], hydrogen ions are implanted to a plain Si wafer, which is then bonded to an oxidised Si wafer. The formed "zipper" layer helps to transfer a thin Si layer to another wafer. The resulting SOI and BOX layers have good thickness uniformities, and thicknesses up to 1.5 and 3 µm, respectively. The SOI thickness on Smart-cut and SIMOX wafers can be increased by using epitaxy. Epitaxial layer transfer (ELTRAN) wafers [75] are fabricated by using a high-pressure water jet to separate an epitaxial Si layer from its original substrate. This provides good thickness uniformity for various SOI and BOX thicknesses. Presently, ELTRAN wafers are available only for 300 mm wafers. Bond-and-etchback SOI (BESOI) wafers [63, 71] are fabricated by bonding a Si wafer to an oxidised Si wafer, and by chemical-mechanical thinning it to the desired SOI thickness, as illustrated in Fig. 6. They are relatively inexpensive and well suited for thick, low-loss waveguides. The SOI thickness inhomogeneity is typically 0.5–1 µm, which is the main limitation of BESOI. Below ~5 µm thickness the relative thickness variation becomes unacceptably high for many optical applications.

Figure 6. Fabrication of a BESOI wafer (dimensions not in scale).

Despite its apparently opaque character at the visible wavelengths from 200 to 700 nm, Si is highly transparent at near-IR wavelengths from 1.2 to approximately 7 µm [76]. This is particularly useful for fiber-optic communication, which is usually carried out between 1.3 and 1.7 µm, and especially at $\lambda \approx 1.55$ µm. The light sources, waveguides, modulators, detectors etc. must naturally all operate at the same wavelength. Therefore, the ongoing development of efficient, Si-based light sources and detectors to the $\lambda = 1.3$–1.7 µm range is particularly important for SOI waveguide technology (see Chapter 1.3).

Light propagation in a silicon waveguide is based on total internal reflection (TIR) at the outer boundaries of the Si core. The core ($n_{Si} \approx 3.5$) is usually surrounded by SiO_2 ($n_0 \approx 1.5$) or air ($n_0 \approx 1$). Therefore, the index difference $\Delta n = n_{Si} - n_0 = 2$–$2.5$ is exceptionally high compared to other waveguide technologies and optical fibers ($\Delta n < 0.01$). In the theory and simulations presented in this thesis, it is by default assumed that the Si core has $n_{Si} = 3.48$, and it is surrounded by an oxide cladding with $n_0 = 1.46$. Furthermore, claddings are assumed to be sufficiently thick to be considered semi-infinite.

The SOI layer itself acts as a slab waveguide (see Fig. 7a). However, the realisation of a PIC requires also horizontal confinement, i.e. a truly two-dimensional (2D) waveguide cross-section. If the core has a square cross-section, it should be 0.35×0.35 μm^2 or smaller to provide single-moded operation. A rectangular core (see Fig. 7b) can be somewhat thinner and wider, or vice versa. Such SM strip waveguides can be used to realise extremely miniaturised PICs and they have been demonstrated by several authors [77–80]. However, it is difficult to couple light into such small structures, and they also have high scattering losses due to their sensitivity to surface roughness. Alternatively, SM operation can be obtained by using a rib structure [82]. An SOI rib waveguide (also known as an SOI ridge waveguide) is illustrated in Fig. 7c. Large rib waveguides offer efficient coupling with SM fibers. Their main limitation is the required large bending radius that limits the miniaturisation of PICs [II, 81]. The fourth Si waveguide type is a photonic crystal (PhC) waveguide [83], illustrated in Fig. 7d. This work involved the development of fabrication technology for PhC waveguides [70, 84] as a by-product of waveguide grating development [VII]. Otherwise the details of PhC waveguides are outside the scope of this thesis and the focus is primarily in large SM rib waveguides. [I]

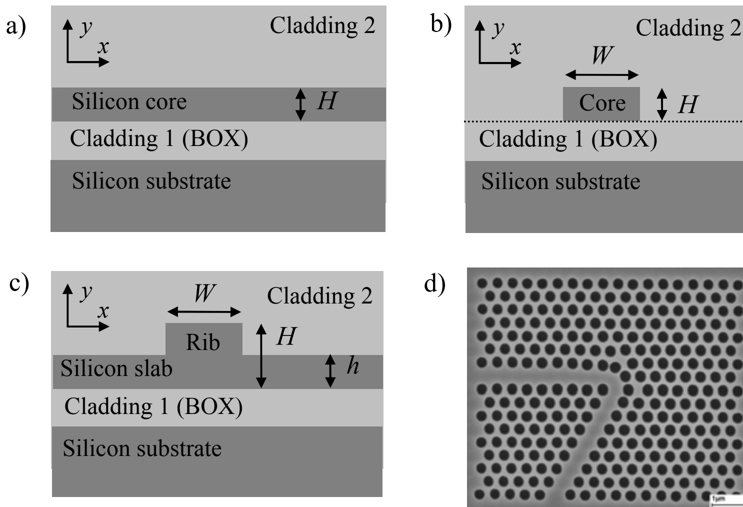

Figure 7. Schematic cross-sections (a–c) of three basic SOI waveguide structures and the used dimensional variables: a) a slab waveguide, b) a strip waveguide, and c) a rib waveguide. d) Top view of a photonic crystal waveguide forming a 120° bend [70].

In order to successfully apply Si waveguides in PICs, one should be able to provide at least low-loss waveguides and some passive waveguide components. In SOI technology, low propagation losses have been reported for MM slab waveguides (0.15±0.05 dB/cm for $\lambda = 1.3$ µm) [85], SM wet etched rib waveguides (<0.1 dB/cm) [86], and SM dry etched rib waveguides (<0.5 dB/cm) [72]. Even for SM strip waveguides with sub-micron dimensions, losses as low as 0.8 dB/cm have already been reported [79]. For realising functional PICs, SM dry etched waveguides are usually required [22]. With SOI waveguides, many passive building blocks for PICs have also been demonstrated. Some examples are optical couplers [87], splitters [78, 88, 89], wavelength filters [90–92] and wavelength multiplexers [69, 93–95]. Monolithic [39, 55, 59] and hybrid [69, 90, 92] integration of SOI waveguide components with light sources and detectors has also been successfully demonstrated.

Some of the simplest optoelectronic components in PICs are switches and modulators that alter their optical output power(s) according to electrical control signals. They are based either on absorption or interference. The optical absorption of Si can be increased by introducing a large quantity of free carriers into it. By free carrier injection (and depletion) one can tune the transparency of Si and to form e.g. an optical modulator [96, 97]. Optical intensity can also be controlled by using interferometry, i.e. by combining two or more coherent light beams, so that their mutual phase difference determines the intensity of output light. Interferometric modulation or switching in Si requires that the refractive index of silicon (n_{Si}) can be tuned. The simplest way to realise this is to heat silicon [I, III–V, 88, 98–100], because the thermo-optic (TO) constant of silicon is as high as $1.86 \cdot 10^{-4}$ K^{-1} [101]. Another way is to slightly tune the number of free carriers [96]. This method is faster, but more complicated to implement. It is also somewhat limited by the absorption loss that increases rapidly as a function of free carrier density. However, it was recently used by Intel to demonstrate a 1 GHz modulator based on Si waveguides [97].

Unlike the cylindrical symmetric SM fibers, asymmetric Si waveguides have usually fixed polarisation axes with respect to the Si chip, namely a vertical and a horizontal axis. When pigtailed with SM input and output fibers, a Si waveguide component should operate identically with both polarisations. However, the asymmetry of the geometry and stress can easily lead to different light propagation velocities for the two polarisation axes [95]. Polarisation dependent loss and wavelength filtering may also become a problem. Thus, the polarisation dependency of Si waveguide components should usually be minimised. However, in some applications the Si waveguides are pigtailed with polarisation maintaining (PM) fibers that also have fixed polarisation axes. Then the polarisation dependency is usually not a problem. Instead, the Si waveguide should then maintain light in the original polarisation state, i.e. to have a sufficiently high polarisation extinction ratio (PXR). The polarisation axes of the PM fibers and the Si waveguides should be rotationally aligned with high accuracy in order to minimise polarisation cross-talk at the fiber-waveguide junctions [VIII].

1.5 Aims of the thesis

The aim of the thesis has been to provide some basic building blocks that can promote the development of silicon microphotonics. The entire thesis is related to Si waveguides on an SOI substrate. The focus is on approximately 10 µm thick Si rib waveguides on 100 mm BESOI wafers. The wavelength is 1550 nm, unless otherwise stated. In particular, specific aims of the thesis were the following:

- Development of fabrication technology in order to provide single-moded Si waveguides and waveguide components with small scattering losses (smooth side-walls) and efficient coupling to SM fibers (smooth facets and anti-reflection coating).
- Study of modal properties, light propagation and polarisation effects in different silicon waveguides and waveguide components.
- Development of a fast thermo-optical switch based on Si waveguides.
- Development of novel solutions for vertical tapering and for the miniaturisation of waveguide components, such as couplers and bends.
- Design and process development for silicon waveguide gratings.
- Development of measurement technology for the characterisation and fiber-pigtailing of silicon waveguides and waveguide components.

1.6 Organisation of the thesis

This thesis includes eight original papers published in international scientific journals and reviewed proceedings of international conferences. In the compendium part preceeding these publications, the main goals, techniques and results of the work are summarised, and some unpublished results are also presented. The compendium part is organised as follows. Some background and motivation for the work, as well as the objectives, were presented Chapter 1. It also provides the aims and organisation of the thesis. Chapter 2 presents the theory, simulation and design for Si waveguides and waveguide components. Chapter 3 briefly describes the used fabrication methods and tools. It also presents process development for multi-step structures, waveguide gratings and photonic crystals. Chapter 4 summarises the experimental results. Conclusions are given in Chapter 5. Simulation and mask design softwares are described in Appendix A.

The eight original publications were selected so that they cover the majority of the results without significant overlapping. In addition to them, the author has published numerous proceedings papers in international and national conferences, and filed six international patent applications as a primary inventor. Some of those directly related to this thesis can be found from Refs. [23, 28, 62–68, 70, 84].

2. Theory, simulation and design

2.1 Electromagnetic theory of waveguides

Light propagation in waveguides can be theoretically approached by two alternative methods. A straightforward method is to calculate how a certain electro-magnetic input field propagates through a 3D waveguide structure. Light propagation is governed by the Maxwell's equations [102] and it can be simulated with beam propagation methods (BPM) and finite-difference-time-domain (FDTD) algorithms.

Another method is based on the analysis of waveguide modes in a 2D cross-section of a waveguide, which is invariant along its propagation axis, i.e. the z-axis (coordinate system shown in Fig. 7). Such a waveguide has a discrete number of propagating modes, which satisfy Maxwell's equations [102] and propagate losslessly with fixed transverse intensity distributions $I(x,y)$. Waveguides also have a continuum of radiating modes that radiate power away from the waveguide. Any physical intensity distribution $I(x,y,z)$ in the waveguide can be represented as a sum of propagating and radiating modes. When light propagates along the z-invariant waveguide, each propagating mode has a fixed power, while the power coupled to the continuum of radiating modes constantly radiates away from the waveguide. Each mode propagates with a (phase) velocity of c/n_{eff}, where c is the speed of light in vacuum and n_{eff} is the effective index of the mode [103]. If several modes are excited by an input field the resulting z-variation in the transverse intensity distribution can be explained by modal interference and radiation losses.

In points of waveguide discontinuity modes exchange power. The power coupling η of fields ψ_1 and ψ_2 across a discrete junction is calculated from the overlap integral [104]

$$\eta = \frac{\langle \Psi_1 | \Psi_2 \rangle^2}{\|\Psi_1\|^2 \|\Psi_2\|^2}, \qquad (1)$$

which can be calculated easily for real scalar fields, but also for complex and vectorial fields [105]. If the waveguide is not z-invariant, local modes can be calculated for each cross-section [105]. Gradual transformations couple power between dissimilar local modes, unless the transformations are adiabatic, i.e. sufficiently slow along the z-axis.

The electro-magnetic field of a waveguide mode, or light in general, consists of two fields; the electric field $\boldsymbol{E}$ and the magnetic field $\boldsymbol{H}$. The simulation softwares used in this work calculate either one (scalar algorithms) or both fields (vectorial algorithms). The Poynting vector $\boldsymbol{S} = \boldsymbol{E} \times \boldsymbol{H}$ describes the flow of electro-magnetic power. Thus, the intensity of light is obtained as the magnitude of the time-averaged Poynting vector. For a harmonic plane wave in silicon the amplitude ratio of $\boldsymbol{E}$ and $\boldsymbol{H}$ is [102]

$$\frac{|\boldsymbol{E}|}{|\boldsymbol{H}|} = \frac{\sqrt{\mu_0}}{n\sqrt{\varepsilon_0}} \approx 108\,\Omega\,, \tag{2}$$

where μ_0 and ε_0 are the vacuum permeability and permittivity, respectively. This applies quite well to waveguide modes as well.

Throughout this thesis, transverse electric (TE) and transverse magnetic (TM) polarisations refer to waveguide modes (or light in general) with $\boldsymbol{E}$ field mostly horizontal (x) and vertical (y), respectively, when the chip lies horizontally. By definition, a SM waveguide has only one propagating mode, i.e. the fundamental mode, for each polarisation. In homogeneous material, such as Si core or SiO_2 cladding, $\boldsymbol{E}$ and $\boldsymbol{H}$ are continuous functions of position. At the boundary between two dielectric media, such as the Si-SiO_2 interface, the tangential components of $\boldsymbol{E}$ and $\boldsymbol{H}$, and the normal components of $\varepsilon\boldsymbol{E}$ and $\mu\boldsymbol{H}$ are always continuous. In both Si and SiO_2, the permeability $\mu \approx \mu_0$ and the permittivity $\varepsilon \approx \varepsilon_0 n^2$. Thus, at a boundary between two dielectric materials all other components of $\boldsymbol{E}$ and $\boldsymbol{H}$ are continuous, except for the normal component of $\boldsymbol{E}$. In a Si-SiO_2 interface the normal component of $\boldsymbol{E}$ changes by a factor of $(n_{\mathrm{Si}} / n_0)^2 \approx 5.7$.

In a Si waveguide the $\boldsymbol{E}$ and $\boldsymbol{H}$ fields of a well-confined mode (far from cut-off) have negligible z-components. When light exits a waveguide through a perpendicular end-facet, the $\boldsymbol{E}$ and $\boldsymbol{H}$ fields are mostly tangential to the facet, and the intensity distribution is well maintained. If light enters free-space (air), the intensity distribution can be experimentally recorded with appropriate optics and an IR camera.

At the sidewalls of the waveguide, the continuity of the intensity distribution depends on the orientation of the electric field. For example, if $\boldsymbol{E}$ is perfectly horizontal (TE) the intensity distribution is continuous at all horizontal interfaces, but changes by a factor of 5.7 at a vertical Si-SiO_2 interface. This creates differences between the intensity distributions and effective indices of TE and TM modes, leading to geometrical birefringence. In silicon waveguides with large core dimensions the fundamental mode is well confined into the core. Then the intensity is very small at the core edges and the geometrical birefringence is weak. In smaller waveguides the intensity at the core edges increases and the geometrical birefringence becomes stronger.

As commercial simulation tools (see Appendix A and Refs. [18, 106]) were used in this work, the reader is encouraged to find detailed description of electromagnetic theory and waveguide modes from the variety of good text books [4, 102, 103, 105].

2.2 Straight waveguides

In this work, the number of propagating modes N, as well as the intensity distributions and effective indices of the modes, were calculated for various cross-sections of straight SOI waveguides. Semi-analytical solutions exist for slab waveguides, while the analysis of strip and rib waveguides can only be carried out with numerical methods. Publication I presents a partial summary of these results, including slab, strip and rib waveguides (refer to Fig. 7). Modal calculations were also carried out for publications II (junction losses), III–V (fiber coupling), and VI–VII (n_{eff} calculations).

Calculated effective indices of the first three TE and TM modes, N, and N^2 for a 1D slab waveguide are shown in Fig. 8 as a function of the slab thickness H_{slab}. It can be seen that for the fundamental mode $n_{eff} \approx n_{Si} \approx 3.48$ when $H_{slab} >> 1$ µm, and that n_{eff} decreases rapidly when $H_{slab} \leq 1$ µm. Each higher order mode is cut-off when $n_{eff} \approx n_0 = 1.46$ (cladding). The cut-off thicknesses for the two higher order modes are approx. 250 and 500 nm, respectively. As a function of H_{slab}, N increases quite linearly, so that 1 and 10 µm slabs support 5 and 41 modes, respectively.

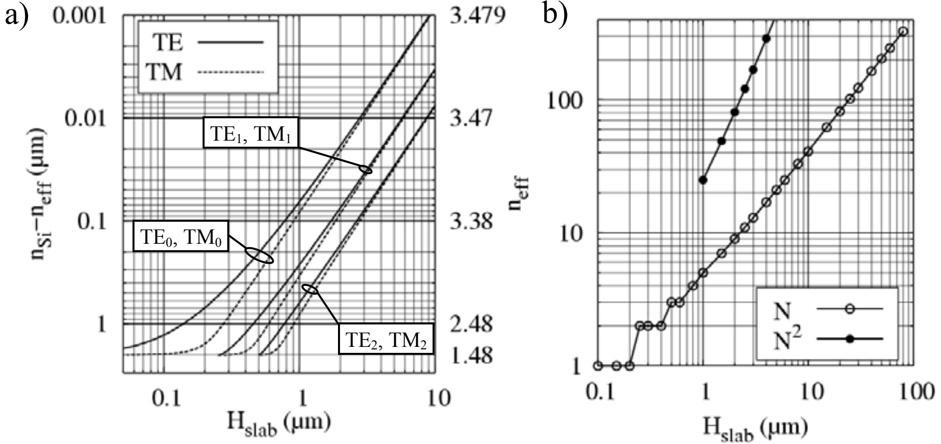

Figure 8. a) Calculated n_{eff} for the three lowest TE and TM modes as a function of slab thickness H_{slab}. b) Calculated number N of propagating modes and N^2 as a function of H_{slab}. The calculated discrete points are connected with straight lines for better visualisation, although N and N^2 are always integers ($n_{Si} = 3.48$, $n_0 = 1.46$ for both graphs).

The combination of extremely high Δn and $H_{slab} > 1$ µm enables a multitude of propagating modes and confines them very efficiently into the Si core, except for the modes close to cut-off. This can be seen from Fig. 9, which shows the intensity distributions of the first three modes in a 10 µm thick slab.

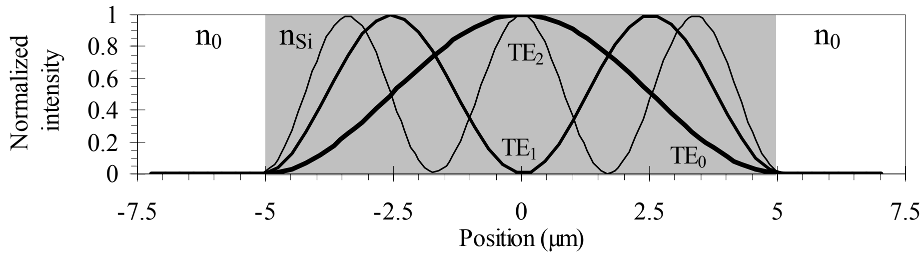

Figure 9. a) Calculated intensity distributions of the first three modes in a 10 µm thick slab waveguide. Grey area illustrates the Si slab (n_{Si} = 3.48, n_0 = 1.46).

If $H_{\text{slab}} \geq 1$ µm, then N^2 is a relatively good approximation for the number of modes in a $H_{\text{slab}} \times H_{\text{slab}}$ strip waveguide. More accurate analysis can be made by using the effective index method (EIM) [103] to simplify the cross-section from 2D to 1D, or by directly calculating the modes of the 2D cross-section. In this work, rigorous 2D calculations were used to study the modal properties of strip waveguides (n_{Si} = 3.48, n_0 = 1.46). Simulations verified that the effective index approximation is not valid close to the SM region. An approximate SM limit was found to be $W \times H \leq 0.13$ µm^2, as is illustrated in Fig. 10. Calculated intensity distributions of TE_{00} and TM_{00} modes in three strip waveguides are presented in Fig. 11. Strong polarisation dependency can be observed below the SM limit.

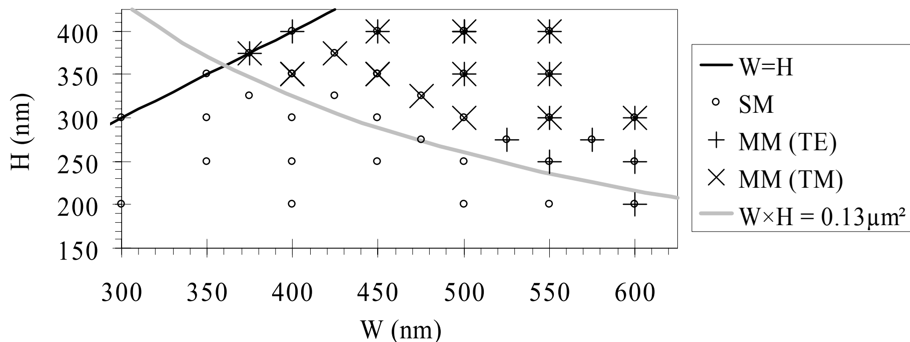

Figure 10. Calculated single-mode limits in strip waveguides. Lines illustrate the square case and the analytical SM condition.

Unlike slab and strip waveguides, rib waveguides can be SM even at dimensions over 10 µm. It was found already in the 1970s [107–109] that a slab surrounding a rib can act as a mode sink for the higher order modes. For a practical implementation in SOI waveguides this was proposed in 1991 by Soref et al. in a famous paper [82] that also involved a simple SM condition (Soref's width limit)

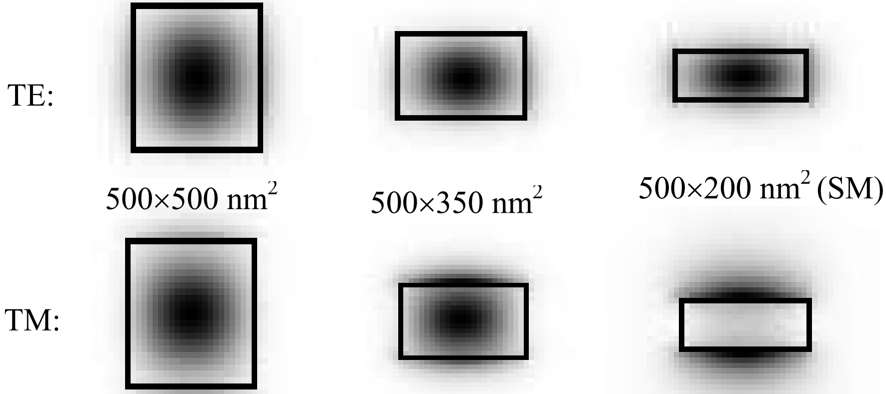

Figure 11. Calculated intensity distributions of fundamental TE and TM modes in three strip waveguides with indicated W×H.

$$W < W_{\text{Soref}} = 0.3H + \frac{h}{\sqrt{1-(h/H)^2}} = 0.3H + \frac{1}{\sqrt{h^{-2} - H^{-2}}} \tag{3}$$

that was proposed to be valid for both polarisations as long as the waveguide is sufficiently thick ($H > 2\lambda \approx 3.1$ µm) and the thickness ratio $h/H \geq 0.5$. With simple manipulation, Eq. (8) in [82] can be converted into a more accurate SM condition

$$W < W_{\text{Soref,Q}} = 0.3(Q+H) + \frac{1}{\sqrt{(Q+h)^{-2} - (Q+H)^{-2}}}\,, \tag{4}$$

where

$$Q = \begin{cases} Q_{\text{TE}} = \dfrac{\lambda}{\pi\sqrt{n_{Si}^2 - n_0^2}} & \text{for TE polarisation and} \\ Q_{\text{TM}} = Q_{TE}\,(n_0/n_{Si})^2 & \text{for TM polarisation.} \end{cases} \tag{5}$$

This formula is valid also for thinner rib waveguides if $h/H \geq 0.5$. For $\lambda = 1550$ nm, $n_{Si} = 3.48$ and $n_0 = 1.46$, one obtains $Q_{\text{TE}} = 156$ nm and $Q_{\text{TM}} = 27$ nm.

Obeying Soref's width limitation prevents the existence of higher order horizontal modes by assuring that their n_{eff} is lower than the effective index of the fundamental mode in the 1D slab waveguide surrounding the rib. Thus, all higher order horizontal modes leak into the slab. On the other hand, higher order vertical modes are eliminated by choosing $h \geq H/2$. Then their lowermost local intensity maxima also leak into the slab. When the

SM limit is approached, higher order modes spread into the slab and finally become radiative.

In order to verify Eq. (4) and to extend it to the range where $h/H < 0.5$, a detailed modal analysis was carried out for 10 and 3 µm thick rib waveguides with various slab thicknesses ($0.25 \leq h/H \leq 0.8$) and rib widths. With a given polarisation, each simulated cross-section was evaluated to be SM or to support the 10 or 01 mode, or both. Some limiting cases were left undefined. The true SM limit is expected to lie somewhere in a so-called transition zone, which is limited by the widest clearly SM and the narrowest clearly MM structure. The width of this region depends on the spacing of simulated rib widths and the simulation accuracy. Especially at $h/H \approx 0.4$, it is limited by the existence of undefined points, not the width variation. The results are summarised in Figs. 12–13.

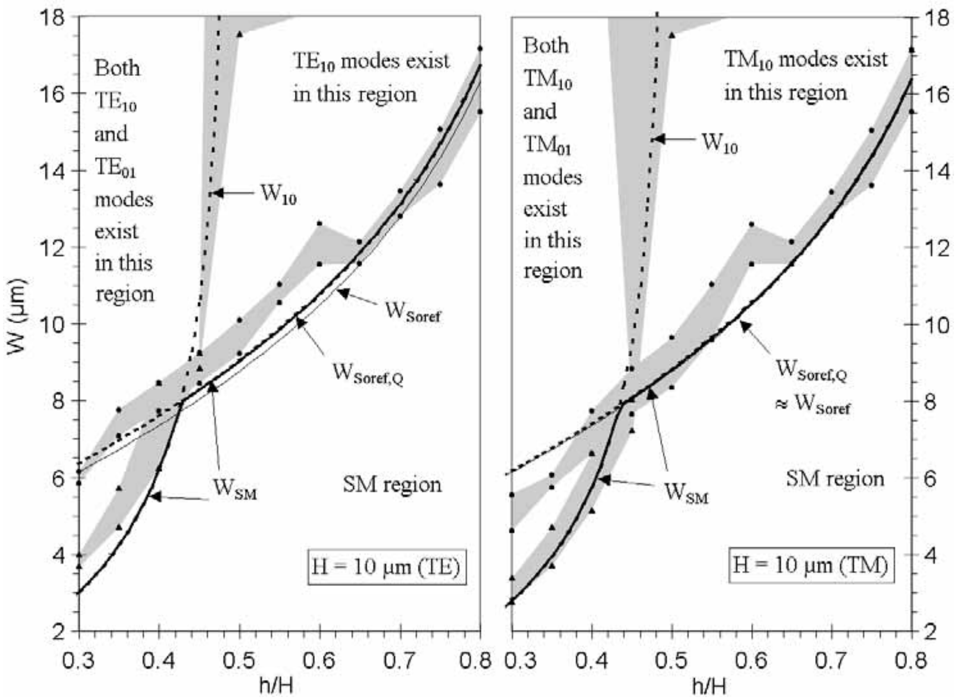

Figure 12. Theoretical and simulated SM conditions for 10 µm thick rib waveguides at TE (left) and TM (right) polarisations. The "transition zone", where the first higher order mode is expected to vanish according to simulations (black dots), is illustrated with grey colour separately for the horizontal 10 mode and the vertical 01 mode. Thin solid line describes the Soref's limit (Q = 0, extended to h/H < 0.5) according to Equation (3). Dashed lines represent the cut-off limits for 10 and 01 modes according to Equations (4) and (7), respectively. Thick solid line describes the proposed new SM limit according to Equation (6).

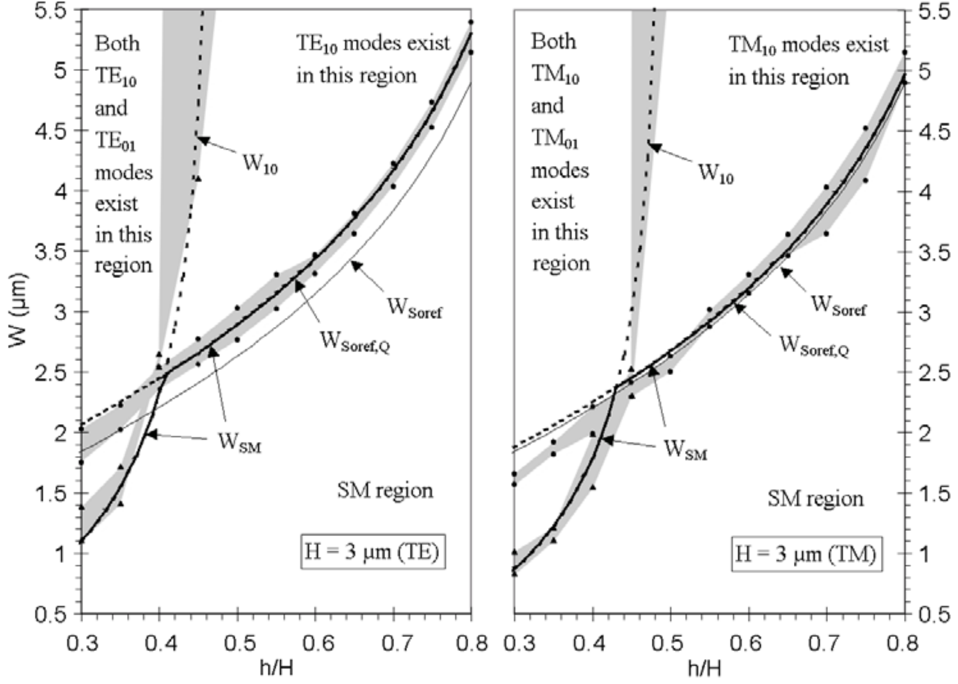

Figure 13. Theoretical and simulated SM conditions for 3 µm thick rib waveguides at TE (left) and TM (right) polarisations. For notations refer to Fig. 12.

When $h/H > 0.5$, there are no TE_{01} and TM_{01} modes and the cut-off widths for TE_{10} and TM_{10} modes are easily determined. At cut-off, these modes spread into the slab and their local intensity maxima clearly pass the outer edges of the rib. Beyond its cut-off, a propagating mode can usually not be found by the algorithms or the result is clearly a non-physical consequence of the finite calculation area. A calculated waveguide mode is not truly propagating if it is many times wider than the rib, as the power of such a mode will be radiated away by the slightest bend or any other variation along z. The cut-off widths for the TE_{01} and TM_{01} modes at $h/H < 0.5$ are much more difficult to determine unambiguously. Especially when $H << 10$ µm and $h/H << 0.5$, the local intensity maxima of these modes do not leave the rib at cut-off. The power ratios between their local intensity maxima change and the modes slowly become leaky, but localised solutions can be found even for modes that are clearly too lossy to be considered as propagating modes. Close to cut-off, these modes resemble substrate coupled waveguide modes or leaky fiber modes [105: p. 487]. Theoretically these modes settle between propagating and radiating modes. In this work, a mode was considered strictly cut-off if its loss was >10 dB/cm, all the local intensity maxima were not confined below the rib or the intensity distribution was many times wider than the rib. Calculated intensity distributions of TE_{10} and TE_{01} modes far from cut-off and close to their cut-off limits are shown in Fig. 14.

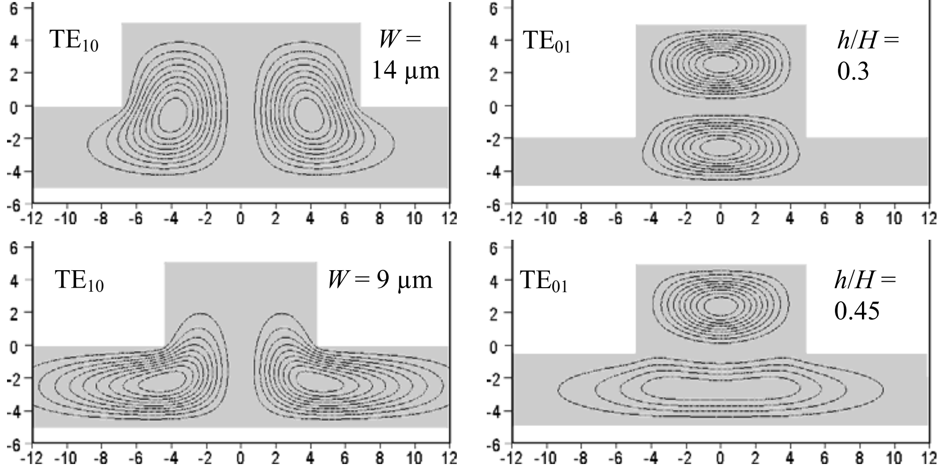

Figure 14. Calculated intensity distributions of TE$_{10}$ and TE$_{01}$ modes far from cut-off (upper row, modes well confined) and close to the cut-off limit (lower row, modes spread into the slab). For TE$_{10}$ mode rib width W is reduced from 14 to 9 µm (H = 10 µm, h/H = 0.5), while for TE$_{01}$ mode h/H is increased from 0.3 to 0.45 (H = W = 10 µm). Contour lines represent constant intensity levels with 10% increments.

Rib waveguides with H = 1 and 1.5 µm were also simulated, but the analysis of the results was much more difficult than for H = 10 and 3 µm. All modes were no longer linearly polarised (no clear TE and TM modes) and the SM limit was very difficult to determine unambiguously. The lack of reliable simulation results in literature also indicates that the modal behaviour of small Si rib waveguides is quite complicated.

Based on the simulations, a new analytical SM condition was proposed and numerically fitted to the results. This new formula is

$$W < W_{SM} = \begin{cases} W_{Soref,Q} & \text{if} \quad (Q+h)^{-2} - 4(\mathrm{Q}+\mathrm{H})^{-2} \le 0 \\ \min\left(W_{Soref,Q}, W_{10}\right) & \text{if} \quad (Q+h)^{-2} - 4(\mathrm{Q}+\mathrm{H})^{-2} > 0, \end{cases} \tag{6}$$

where

$$W_{10} = c_1(Q+H) + \frac{1}{\sqrt{(Q+h)^{-2} - 4(Q+H)^{-2}}}, \tag{7}$$

and c_1 is a numerical fitting parameter with an optimum value of -0.1. In addition to the Soref's accurate width limitation ($W_{\mathrm{Soref,Q}}$), another width limitation (W_{10}) is given for eliminating the higher order vertical modes. According to Figs. 12–13 the new SM condition appears to be at least roughly valid when $c_1 = -0.1$, H = 3–10 µm and h/H = 0.3–0.8. It was not yet presented in any of the original publications I–VIII. The mathematical

form of the proposed formula does not have any clear physical interpretation (yet), but its mathematical characteristics are similar to the analytical expressions presented in Refs. [82, 109]. To gain a deeper understanding of SM condition in rib waveguides, especially in thin and deeply etched rib waveguides, more theoretical considerations and simulation results are required.

In order to give Eq. (6) a more solid basis, a waveguide with H = 3 µm and h/H = 0.3 was analysed also with a 3D BPM algorithm. This method is slower and one needs special tricks to excite higher order modes near the SM limit. In this work, TE_{10}, TE_{01}, TM_{10}, and TM_{01} modes were excited one at a time in a clearly MM input waveguide with h/H = 0.15 and W = 1.6–2.2 µm. The waveguide was then slowly transformed closer to the SM limits by using a method described later in Chapter 2.6. Before final tapering the waveguide had h/H = 0.3 and W = 1.1, 0.8, 0.9, and 0.6 µm for TE_{10}, TE_{01}, TM_{10}, and TM_{01}, respectively. At this point it was checked that all modes were still propagating with negligible losses. Finally, W was slowly decreased until the higher order modes were clearly cut-off and the power originally coupled to them started to radiate into the slab. The estimated SM width limits for the four modes were 1.7–1.9 µm, 1.2–1.4 µm, 1.5–1.7 µm, and 0.8–1.0 µm, respectively. Corresponding limits according to Eq. (6) are 2.1, 1.1, 1.9, and 0.9 µm, respectively. Thus, the agreement of BPM simulations is rather good with respect Eq. (6). Furthermore, the agreement is excellent with respect to the modal simulation results (compare to Fig. 13).

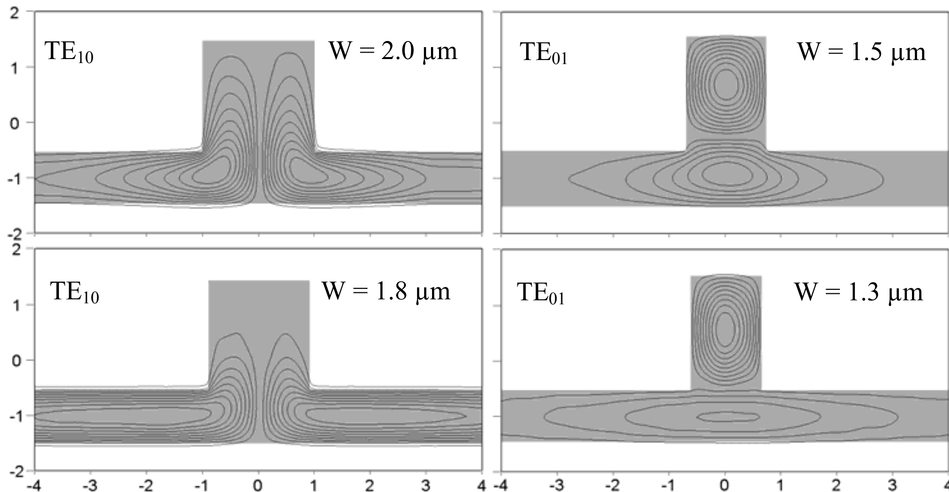

Figure 15. Cross-sections of 3D-BPM simulations used to check the validity of Eq. (6) for both TE_{10} (left) and TE_{01} (right) modes when H = 3 µm and h/H = 0.3. The modes are clearly cut-off between the two shown rib widths and the results agree very well with modal simulations (refer to Figs. 12–14).

2.3 Optical coupling of fibers and silicon waveguides

Coupling loss in a junction between a SM fiber and a Si rib waveguide is due to four main factors, namely scattering, reflection, modal mismatch and misalignment. Surface roughness in the junction, and especially at the end facet of the Si waveguide, causes scattering losses. Therefore, the waveguide facets must be carefully prepared by polishing, cleaving or etching. Reflections appear at all dielectric interfaces, and especially at the Si waveguide's end facet. An air gap between the waveguide and the fiber induces interference due to multiple reflections between the fiber and waveguide ends. However, the gap can be filled with index-matching oil or glue, which effectively leaves a single SiO_2-Si interface into the junction. The reflection can then be totally eliminated by adding an anti-reflection (AR) coating to the end facet of the waveguide. The optimum *n* and thickness for a single-layer AR coating between materials 1 and 2 are

$$n_{AR} = \sqrt{n_1 n_2} \text{ and} \tag{8}$$

$$d_{AR} = \lambda / (4n_{AR}), \tag{9}$$

respectively. For a SiO_2-Si interface $n_{AR} \approx 2.25$ and $d_{AR} \approx 172$ nm. The optical coupling between a fiber and a Si waveguide is presented schematically (1D) in Fig. 16.

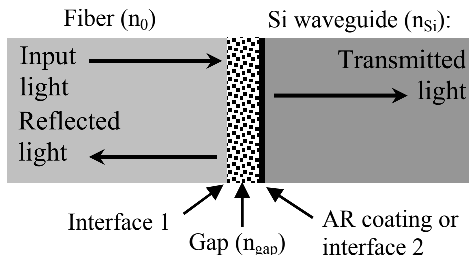

Figure 16. Schematic description of fiber-waveguide input coupling area as a 1D film stack. The gap ($n = n_{gap}$) is filled e.g. with air, index matching oil or glue. If $n_{gap} = n_0 = 1.46$ then the reflection at the first interface is eliminated. An optional AR coating can be used to eliminate the reflection at the second interface.

In the beginning of this work, waveguides were usually characterised without AR coating and air gap filling, which led to relatively high and unstable reflection losses. The total reflection loss for a single fiber-waveguide junction, as well as for a waveguide chip inserted between input and output fibers, can be estimated analytically by using a 1D film-stack method [VI–VII]. This is a valid approximation for large Si waveguides with high optical confinement into the Si core. The reflection coefficients for single SiO_2-air, SiO_2-Si, and air-Si interfaces are 3.5%, 17%, and 31%, respectively. For an airgap between SiO_2 and Si, the theoretical reflection loss is 31±14%. The large variation

is due to the interference of multiple reflections. For a long, tilted or absorbing airgap, the loss variation due to multiple reflections is reduced [102]. However, the best way to avoid loss variations is to fill the airgap with index-matching oil or glue, as was done at the later stages of this work. This leads to a constant 17% (0.8 dB) reflection at both ends of the Si waveguide. Taking into account multiple reflections inside the waveguide, the total reflection loss for the SiO_2-Si-SiO_2 structure is then 25±25% (0–2.93 dB), with an average of ~1.5 dB. Actual reflection loss in a measurement depends on the waveguide's propagation loss, scattering losses at the dielectric interfaces, and the interference effects. Interference depends on the optical length of the waveguide, as well as on the wavelength and the spectral width of the light source used.

The modal mismatch and the impact of misalignment can be calculated from Eq. (1). In the alignment of SM fibers to Si waveguides there are five degrees of freedom, namely x, y, z, θ_x, and θ_y (see Chapter 2.8 for the alignment of PM fibers). When using gaussian mode field approximations for both the fiber and the waveguide, the overall power-coupling efficiency η as a function of radial, longitudinal, and angular misalignments of $\Delta\rho$, Δz, and θ_ρ, respectively, can be expressed by a formula

$$\eta = \kappa \cdot \exp\left\{-\kappa\left[\frac{\Delta\rho^2}{2}\left(\frac{1}{r_1^2}+\frac{1}{r_2^2}\right)+\frac{\pi^2\theta_\rho^2}{2\lambda^2}\left(r_1^2+r_2^2\right)\right]\right\}, \tag{10}$$

where

$$\kappa = \frac{4r_1^2 r_2^2}{\left(r_1^2+r_2^2\right)^2+\lambda^2\Delta z^2/\pi^2 n_{gap}^2}, \tag{11}$$

r_1 and r_2 are the 1/e field radii of the gaussian fields, and n_{gap} is the refractive index of the material within the gap [110]. In this thesis, the mode fields of SM and PM fibers were assumed to be gaussian, and to have an 1/e field radius of $r_1 = r_{\mathrm{SMF}} = 5$ µm. In case of negligible modal mismatch ($r_1 = r_2 = \mathrm{r_{SMF}}$), the transverse, longitudinal and rotational alignment accuracies should be below 1 µm, 30 µm, and 1°, respectively, in order to keep the loss <0.2 dB for each axis. The cumulative effect of $\Delta\rho = 1$ µm, $\Delta z = 30$ µm, and $\theta_\rho = 1°$ is 0.65 dB. These tolerances are achievable with an appropriate alignment stage, transmitted power as a feedback signal, and a careful alignment procedure. However, fabrication of fixed fiber pigtails is much more difficult. Glues typically experience small deformations during and after curing, and for low-cost applications passive alignment is usually required.

Numerical overlap calculations were carried out to determine the modal mismatch between the gaussian field of a SM fiber and the modal fields of different Si waveguides more accurately. According to the results, the modal mismatch for Si rib (and strip)

waveguides with H = 10–14 µm, h/H = 0–0.6 and an optimised W (10–14 µm) varies between 0.1 and 0.5 dB. The optimum coupling is achieved with a 14×14 µm^2 strip waveguide (h/H = 0). The requirement for 1 µm transverse alignment accuracy was also numerically confirmed for Si waveguides with H = 10–14 µm, h/H = 0–0.5 and W = 11–15 µm. An example of the numerically calculated modal mismatch as a function of the vertical misalignment y is shown in Fig. 17. The optimum width changes very little as a function of misalignment, so the estimated misalignment does not necessarily need to be taken into account in the width optimisation.

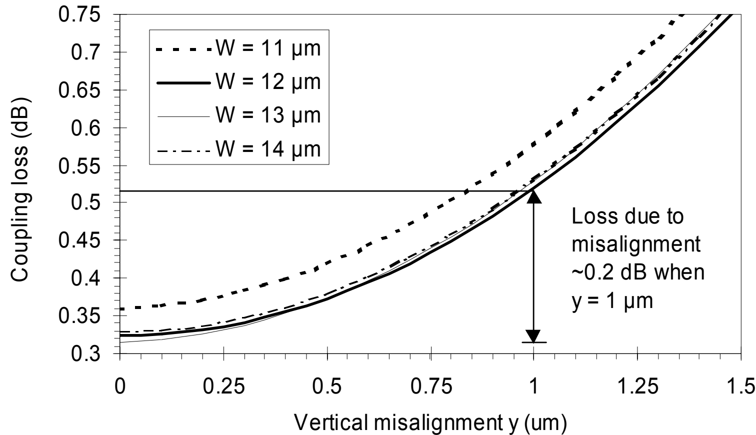

Figure 17. Calculated dependence of modal mismatch between a standard SM fiber and a Si rib waveguide as a function of waveguide width W and vertical misalignment y. Waveguide thickness H = 10 µm and h/H = 0.5.

2.4 Bends and mirrors in Si waveguides

As for the propagating modes of straight waveguides, discrete waveguide modes can also be calculated for waveguides with fixed bending radii. Such waveguides have an invariant cross-section in the cylindrical coordinate system, where the Maxwell's equations can also be applied [111]. In bends, the solutions for the decaying transverse field tails of the mode fields are based on Bessel functions, which are radiative by nature (see e.g. [105: p. 480]). However, the radiation loss for a bend mode may be negligible with a sufficiently large bending radius R, because the radiation losses decrease exponentially as a function of R [103]. For a low-loss and effectively SM bend, the radiation losses should be sufficiently small and high for the fundamental and higher order modes, respectively. Higher order bend modes with low losses may be tolerated if power is coupled only between the fundamental modes of bends and the SM straight waveguides connected to them. However, this can be quite difficult because of the distorted field profiles of the bend modes. With respect to a straight waveguide with a similar cross-

section, the modes of a bent waveguide are shifted away from the centre of curvature, as if they would be affected by a centrifugal force. This induces inter-modal coupling and junction losses at the interfaces between straight and bent waveguides. The overall loss of a fundamental mode due to a bend is, thus, a combination of radiation and junction losses. It can be minimised by optimising the shape of the bend, e.g. by changing R gradually [II].

A significant drawback of a large SM rib waveguide is its sensitivity to bending. Single-moded Si strip waveguides ($W \times H \approx 0.13\ \mu m^2$) may have bending radii around 1 μm [80], while a large Si rib waveguide (e.g. $W \times H \approx 100\ \mu m^2$) may require a 10 mm radius, or more. In this work, the overall bending losses of 1.5, 3 and 10 μm thick rib waveguides were calculated for different radii. The simulations were originally carried out for a Master's thesis [81], supervised by the author. The results are presented in publications I–II, and summarised below. Some older, and less accurate, bend simulations are also reported in publication III and Chapter 2.5.

Due to the slowness of rigorous bend calculations, the thickness ratio h/H was fixed to 0.5 and the rib widths were chosen according to the Soref's simple SM condition (3). Thus, for H = 1.5, 3 and 10 μm, W = 1.3, 2.6, and 8.8 μm, respectively. Results from the calculations are presented in Fig. 18 as the radiation loss for a 90° bend. The junction losses are excluded from Fig. 18 as they can be minimised by a proper bend design. Radiation loss has a strong polarisation dependency and thinner waveguides have significantly smaller bending radii with a given tolerable loss (e.g. 0.1 dB/90°). The required bending radius (R >> 10 mm) for a 10 μm thick waveguide with $h/H \approx 0.5$ and $W \approx H$ is not suitable for the dense integration of PICs.

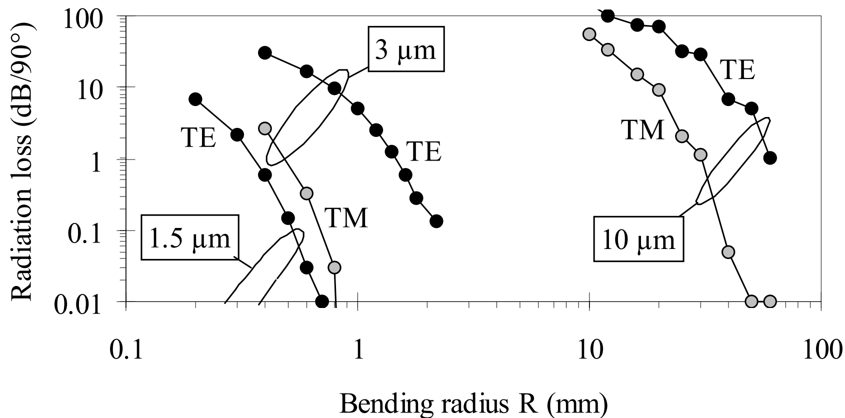

Figure 18. Calculated dependence of radiation losses on waveguide thickness (H = 10, 3, or 1.5 μm), polarisation (TE/TM) and bending radius R.

Bending losses can also be reduced by using wider ribs or smaller *h*/*H* ratios [93, 111]. This was not studied in the original publications, but some new results are given here. The dependence of bending losses on *W* and *h*/*H* in 10 µm thick waveguides with *R* = 20 mm was calculated at the end of this work. A new computer (2.8 GHz, 2GB RAM) was used for these simulations, which enabled the densification of the calculation grid by a factor of two in both directions. This improved the simulation accuracy and resulted in somewhat higher losses than those presented above for the same structure. The new results are summarised in Fig. 19. Smaller *h*/*H* clearly reduces the bending losses, but at sufficiently small *h*/*H* and sufficiently wide rib, higher order modes may also appear with low losses. Based on Fig. 19, a useful compromise for *H* = 10 µm and *R* = 20 mm could be e.g. *h*/*H* ≈ 0.4, which enables low-loss SM bends when *W* > 7 µm. Smaller *h*/*H* or wider *W* could enable even smaller *R*. Unfortunately, accurate calculation of radiation losses for various combinations of *H*, *h*/*H*, *W* and *R* values is not practical with available computers and software tools.

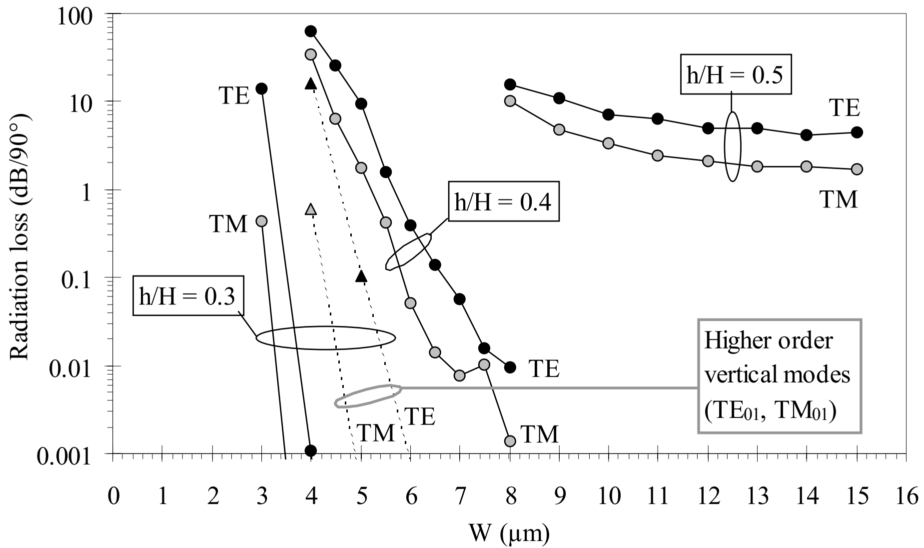

Figure 19. Calculated dependence of radiation losses on rib width W, thickness ratio h/H (= 0.5 / 0.4 / 0.3) and polarisation (TE/TM) when H = 10 µm and R = 20 mm. Higher order modes with low-loss can be found if h/H is sufficiently small and W sufficiently large.

An alternative for a waveguide bend is a waveguide mirror [112], which uses total internal reflection to deflect the light propagating along one waveguide into another waveguide. In SOI waveguides, the high Δn enables a deflection angle >90° if the reflection occurs at a Si-SiO_2 or Si-air interface (according to Snell's law). Successful reflection requires that the mirror facet be vertical and etched through the whole SOI layer,

and that light is well confined into the SOI layer. The mirror can be simply realised into a large multi-moded strip waveguide, as illustrated in Fig. 20. Then the coupling to SM rib waveguides must be separately solved, e.g. with the methods presented in Chapter 2.6. In thin SM strip waveguides significant amount of light bypasses the mirror leading to high losses. Direct integration of a through-etched mirror facet to a rib waveguide requires two masks and accurate alignment between them.

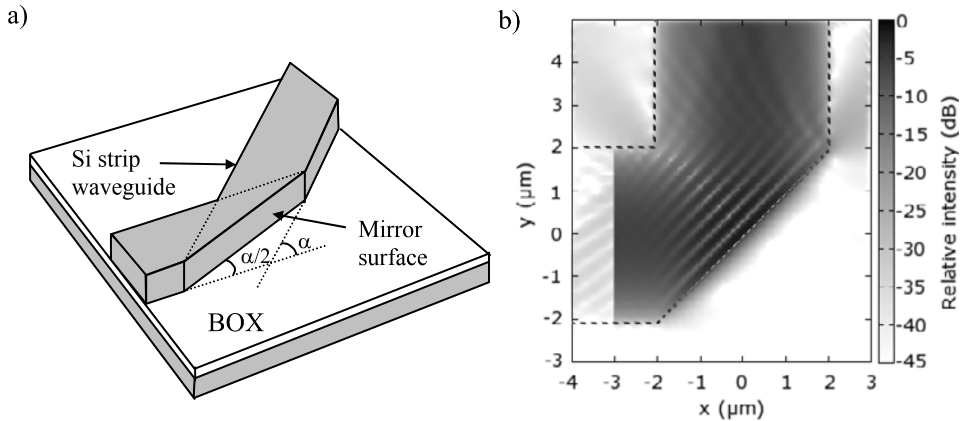

Figure 20. Waveguide mirror in a strip waveguide. a) Schematic illustration of a general structure. b) Reflection of light from a waveguide mirror, as simulated with a 2D FDTD software recently developed at VTT (top view, $W = H = 4$ μm, $\alpha = 90°$).

2.5 Directional couplers and interferometric switches

Fast and inexpensively mass produced optical switches (and modulators) are one of the needed key elements if optical communication technology is to be brought close to the end users. Present switches can be roughly divided into two speed categories. Those operating above 1 MHz are typically based on nonlinear effects, electro-optical modulation or, in SOI, current injection modulation [89]. Slower switches are typically based on thermal modulation (or moving parts [7]), and they usually operate around 1 kHz or, more generally, at 0.1–10 kHz. Switches operating above 1 MHz are typically much more expensive than those operating around 1 kHz. Furthermore, the fast switches may have harmful thermo-optical effects when operated below 1 MHz [89]. Presently, there is a lack of inexpensive switches and modulators to operate in the 10–1000 kHz range or to have sub-μs response times. Such switches and modulators could be used e.g. in the reconfiguration of optical networks, backup routing of optical signals, and optical data modulation e.g. in broadband connections to homes and small offices. [IV]

Si waveguides provide a possibility to realise particularly fast TO switches and modulators. Fast modulators have been demonstrated with both SOI waveguides [88, 100] and epitaxially grown Si waveguides [98]. The latter have operated with a 700 kHz bandwidth, while the SOI modulators have reached up to 40 kHz [88]. However, it should be noticed that these values correspond to a 3 dB modulation depth. For switches the maximum frequency is limited by the required minimum extinction ratio (ER), i.e. the cross-talk between the two (or more) outputs. This should usually be at least 10 dB, which makes fast switches more challenging to fabricate than modulators. A switch can always be used as a modulator, but not vice versa.

In this work, a fast TO switch based on large SOI rib waveguides was designed, fabricated, and characterised. Finally, it was accelerated by using a novel modulation technology. The design [III] of the switch started the research of SOI waveguides at VTT by the author in 1997. The SOI technology was chosen because it was rather new, it offered some unique advantages with respect to previous waveguide technologies and it was compatible with the Si processing technology available at VTT. The high thermo-optical constant ($1.86 \cdot 10^{-4}$ K^{-1}) and good thermal conductivity of Si suggested that there was some potential for realising particularly fast TO switches. Large rib waveguides with good fiber coupling efficiency, and a 2×2 Mach–Zehnder interferometer (MZI) layout with two successive 50:50 directional couplers (DCs) were taken as the design basis. The designed switch layout is schematically illustrated in Fig. 21. As such, the switch is in a cross-state (off), but it shifts into a bar state (on) if a phase difference $\Delta\phi = 180°$ is introduced between the two waveguide branches. This can be induced by operating at least one of the metallic thin film heaters patterned on top of the ribs.

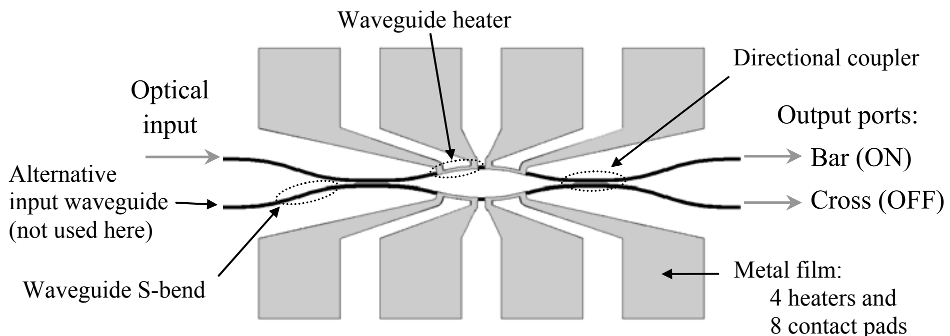

Figure 21. Schematic top view of the designed 2×2 MZI switch (not in scale).

The switch design involved the analysis, simulation and optimisation for fiber coupling efficiency, S-bends, DCs and thermal modulation. Simulations were carried out with the combination of commercial Optonex software (for 2D optics simulations) and a Matlab toolbox (for 2D thermal simulations). After the switch design, these tools were replaced

with more advanced 3D software from BBV Software. Publication III describes the calculation of fiber coupling coefficients and simulation of S-bends, although more accurate results are reported in publications I–II and Chapters 2.3–2.4. The optimum length for DCs was calculated by using a 2D BPM (top view) and a 2D mode solver (cross-section). The results from the two methods were clearly different, which indicated that 2D BPM and/or the assumption of low Δn in a mode solver were not applicable for accurate SOI rib waveguide simulation.

Thermal simulations indicated that the switch could indeed be somewhat faster than a typical TO switch made of e.g. glass or polymer waveguides. The key to fast heating was the thin oxide cladding that conducts heat rapidly from the heater into the Si rib. On the other hand, fast cooling is possible because the Si slab spreads the heat horizontally and the thin BOX conducts it rapidly into the Si substrate. The speed and power consumption were found to be strongly dependent on the boundary conditions used in the simulation. Airflow around the switch and thermal conductivity through the Si substrate into a sample holder are difficult to estimate accurately. With the used boundary conditions, the heating of one interferometer arm by 3°C required 120 mW of electrical power and changed the switch from cross- to bar-state. The rise (0–90%) and fall (100–10%) times were both 200 μs, corresponding to a maximum frequency of approximately 2.5 kHz. Better heat conductivity away from the rib leads to faster cooling, but it also increases the power consumption. Therefore, BOX thickness and deeply etched insulation grooves [88] can be used to choose a desired speed to power consumption ratio. Smaller waveguides and better heat conductivity into the core can provide a faster switch with lower power consumption, but these approaches are limited by the need for small propagation and coupling losses and the required optical insulation between the core and the metallic heater. [IV]

The work described above led to a mask layout (see Figs. 4 and 21) that was used to lithographically pattern all the switches reported in this thesis. It should be noted that the original layout is not thoroughly optimised and that e.g. multi-mode interference (MMI) couplers [23, 113] should be used instead of DCs in future designs. Two heaters were drawn on top of each waveguide branch in order to enable constant power consumption (successive vs. adjacent heaters operated). This also made it possible to modulate the switches with a novel modulation principle, which was invented soon after the mask design. It is briefly summarised below, while a detailed description can be found from publications I and IV–V, and from Ref. [66].

Traditional modulation is based on turning the heating power P simply on and off in a binary manner ($P = P_{on}$ or $P = 0$ W). In some cases bias voltages are used to stabilise the power consumption or to optimise the off-state of a non-ideal switching structure ($P = P_{ON}$ or $P = P_{bias}$). Traditional modulation can be applied by using simple control electronics, but the exponential stabilisation of the temperature difference ΔT between the waveguides seriously limits the attainable frequency. The purpose of the new modu-

lation principle is to remove this limit by optimising the time-dependent heating powers P_1 and P_2 of both waveguide branches during switching operations (rise/fall).

In the new modulation principle, high heating power peaks are used to rapidly heat one waveguide, while the other is cooling down, as illustrated in Fig. 22. Furthermore, at least the off-state is biased, so that both waveguides are equally heated ($P_1 = P_2 = P_{bias}$), and the time-dependence of P_1 and P_2 during a single switching operation (rise/fall) is optimised, so that $\Delta\phi$ is stabilised already before the waveguide temperatures T_1 and T_2 are stabilised. If $\Delta\phi$ is to be raised from 0 to 180°, P_1 forms a high power peak, while P_2 drops from P_{bias} to zero. This increases T_1, decreases T_2 and rapidly increases $\Delta\phi$. Similarly, $\Delta\phi$ can be rapidly decreased from 180 to 0°, by dropping P_1 from P_{on} to zero and by forming a high power peak into P_2. For both operations, the fine structures of P_1 and P_2 are optimised, so that $\Delta\phi$ reaches and maintains its target range as soon as possible.

The new method is different from the so-called overdriven operation [103: p. 330] because it enables switching with arbitrary input data. It is similar to the method described in [114], but it also enables the reduction of fall-times. Extremely high and sharp heating peaks, and perfectly optimised control signals between them, can provide at least one or two orders of magnitude reduction in response times, while maintaining the obtained phase difference between switching operations. Then heat diffusion into the waveguide core, potential heat accumulation, power consumption, and the availability of control electronics become the fundamental limits for switching speed. However, the new method can be implemented to any desired extent from a minor fine tuning to extreme acceleration by optimising the control signals with the given criteria.

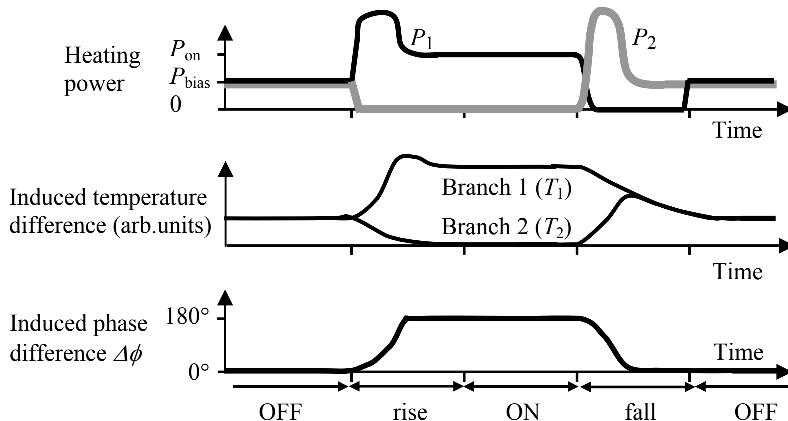

Figure 22. Schematic illustration of the novel modulation principle.

2.6 Multi-step patterning of silicon waveguides

Traditionally, optical waveguides are patterned by using a single mask layer, which is indeed sufficient for many applications. Additional mask layers are often used to define metallic heaters etc, but typically they do not define the waveguide structure. However, with a single mask layer it is difficult to simultaneously define waveguides with SM operation, efficient coupling with fibers, lasers, detectors etc., low-loss propagation, small bending radius, and applicability to miniaturised PICs. Using more than one mask layer in the patterning of a single SOI waveguide cross-section has significant advantages, as is explained in detail in publications [I–II] and Refs. [63–65]. Similar approach is already widely used in compound semiconductor devices [115], and it has been applied to SOI waveguides as well [90, 93, 116]. However, those implementations are somewhat different from the ideas described in this thesis, or insufficiently documented for real comparison. In particular, the proposed multi-step patterning principle avoids the complicated epitaxial growth in the middle of waveguide fabrication, and the light is always confined into a single unitary core made of homogeneous Si. The multi-step patterning principle and its potential is illustrated below with four example structures.

The first two waveguide structures transform a rib waveguide into a thin or thick rectangular waveguide (or vice versa), as shown in Figs. 23a–b. The third transformer waveguide connects two rib waveguides that have different thicknesses, as illustrated in Fig. 23c. The three structures can be combined in various ways, and there is no fundamental reason to limit the multi-step patterning principle to only two mask layers.

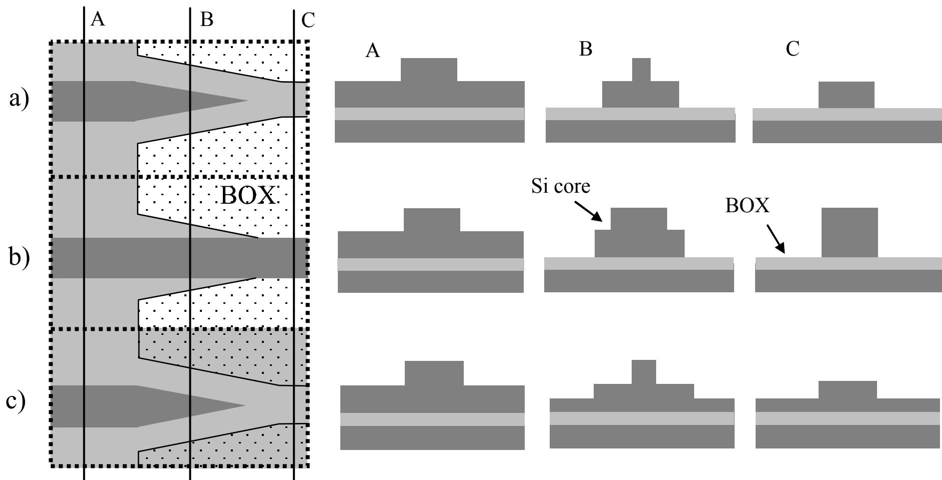

Figure 23. Three different 3D waveguide transformers based on multi-step patterning. The layouts on the left describe the structures a–c) as seen from the top and the cross-sections A, B, and C are shown on the right.

Waveguide transformers, such as those illustrated in Fig. 23, can enable vertical waveguide tapering, coupling between strip and rib waveguides (both with their unique advantages and disadvantages), radical tailoring of both Δn and the number of propagating modes, and e.g. coupling of light into SM strip waveguides and PhC waveguides. However, the waveguide cross-section must be changed adiabatically, i.e. in a sufficiently small angle with respect to the propagation axis. Depending on the type and size of the waveguide, this is expected to require 20–2000 μm long tapering areas [116]. The mask alignment must also be carried out accurately, although the alignment tolerances can be partially relaxed by using appropriate processing steps [64, 65]. According to simulations, the finite widths and the exact positions of the sharp tips in Figs. 23a and c are not critical, as long as the cross-sectional area is much smaller for the tip than for the underlying rib or strip structure. Thus, an easily attainable tip width of 500 nm is sufficient for large structures. The alignment accuracy is around 1 μm in contact lithography and <100 nm in stepper lithography, which are both sufficient for most multi-step structures. It should be noted that outside the transformation area only one mask layer defines the waveguide structure.

The fourth example is a bent rib waveguide with an additional groove etched to its outer side, as illustrated in Fig. 24. The groove locally increases Δn in the bent waveguide section, and it can almost completely suppress the radiation loss, as can be clearly seen from Fig. 24. In order to minimise the overall bending losses, i.e. both junction and radiation losses, the bending radius, as well as the distance and width of the groove, can be adiabatically tuned along the bend. Similar grooves have been proposed for glass waveguides [117, 4: pp. 97–99] and briefly referenced for Si waveguides as well [90].

Based on numerous simulations [I–II], there appears to be significant potential in realising extremely compact PICs based on multi-step SOI waveguides and the advantages should clearly overcome the associated extra efforts in fabrication.

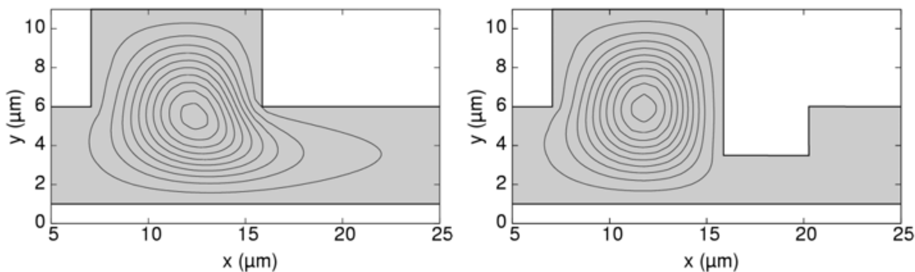

Figure 24. Cross-sections and calculated intensity distributions of bent rib waveguides with R = 20 mm, H = 10 μm, h/H = 0.5, and W = 8.8 μm. a) Without a bend groove (radiation loss 10 dB/90°). b) With a bend groove (radiation loss 0.0002 dB/90°). Contour lines with 10% spacing between 5 and 95%.

2.7 Waveguide gratings

Fiber optic gratings are widely used for reflecting desired wavelength(s) backwards along a fiber or, in general, for producing a desired reflection spectrum. Fiber gratings are usually fabricated by using ultraviolet (UV) light to produce small refractive index changes along a piece of fiber. Waveguide gratings on planar substrates [VI, VII, 62, 90, 91] represent a less mature technology, but they have some clear advantages, especially with respect to fabricating miniaturised gratings and in integrating several different gratings and other optical functions on a single chip.

In this work, waveguide gratings were designed for SOI waveguide technology in collaboration with the Department of Physics at the University of Joensuu (JoFy). The work is reported in publications VI–VII and in Ref. [62]. The target application was an add-drop filter which could be fabricated by adding identical corrugated gratings on top of the two waveguide branches of a 2×2 MZI, as illustrated in Fig. 25a. In order to have efficient fiber coupling and SM operation, the gratings were to be etched on top of ~10 µm thick rib waveguides with $h/H \approx 0.5$ and $W = 7–10$ µm. Therefore, light is expected to be well confined into the Si core with the n_{eff} of the fundamental mode being slightly below 3.5. This means that for a first order grating the period should be $\lambda/(2n_{eff}) \approx 220$ nm and the width of the corrugation groove ~110 nm. Such small structures are extremely difficult to fabricate with good surface quality, although they can result in compact devices.

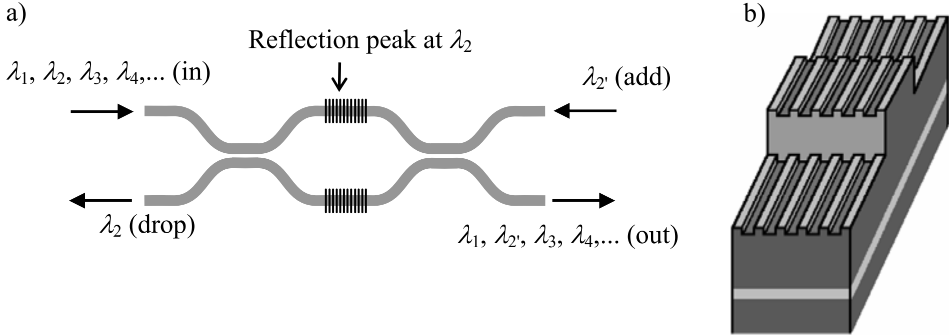

Figure 25. Schematic illustration of a) an add-drop filter and b) the designed waveguide grating.

First, the effective index change Δn_{eff} as a function of H, W and groove depth was calculated for grooves only on top of the rib and grooves extending to the surrounding slab (see Fig. 25b). The latter produced much higher Δn_{eff} values, although even they were <0.0002 if the grating depth was <500 nm, and $W \approx H = 7–10$ µm. The estimated maximum achievable etch depth for the grating was 500 nm. The required grating length as a function of Δn_{eff} was then calculated with a 1D film stack method. In order to have rela-

tively short gratings with >99% reflection, the grating should be as deep as possible and it should preferably extend to the slab region as well.

The results were confirmed with a rigorous 2D simulation tool that was specially developed for this task. The new simulation method is based on rigorous diffraction theory. It is much more accurate than the film stack method, computationally efficient and applicable to the analysis of other corrugated gratings as well. The 2D approximation was implemented by eliminating the horizontal coordinate, thus describing the surface corrugation accurately. However, the approximation presents a SM rib waveguide as a highly MM slab waveguide. This led to the identification of additional reflection peaks that correspond to non-physical higher order modes that in reality present loss. Based on the results, deeper etching enables shorter gratings, but at etch depths >>1 μm coupling to higher order vertical modes leads to harmful losses. The effect of stitching errors in e-beam lithography was also studied. [VI]

2.8 Polarisation cross-talk

Theoretically, propagating waveguide modes have no polarisation cross-talk. In practice, however, waveguides have a finite polarisation cross-talk due to junctions, process non-idealities, and non-adiabatic transformations. In most applications the input polarisation is unknown and it is sufficient to optimise the components with respect to polarisation dependent loss (PDL) and polarisation mode dispersion (PMD). However, in some polarisation maintaining applications the cross-talk between different polarisation modes should be minimised. This typically requires waveguides with sufficiently high birefringencies, low losses, and accurately aligned input junctions. It is possible to realise PM components with low PDL and PMD, but usually components are designed to be either highly polarisation independent (with SM fiber pigtails) or polarisation maintaining (with PM fiber pigtails). In the following, the theory of polarisation cross-talk in Si waveguide components is briefly discussed. More details and experimental results are given in Chapter 3.3, publications [I, VIII] and Ref. [63].

In literature, the term polarisation extinction ratio is commonly used to describe the characteristics of polarisers, PM fibers, waveguides, light propagating in free space and light originating from the end of a fiber or a waveguide [VIII]. In this thesis, the PXR of light that propagates along a SM fiber, or originates from the end of that fiber (PXR_{out}), is defined as the ratio of optical powers P_1 and P_2 coupled to the two differently polarised fundamental modes of the fiber, i.e. $PXR = 10 \cdot \log_{10}(P_1/P_2)$ dB. This and the following definitions apply for waveguides as well as for fibers. Usually, the two fundamental modes are linearly polarised along two mutually orthogonal polarisation axes. In PM fibers these axes are called the slow and the fast axis, while in Si waveguides the axes are horizontal (TE) and vertical (TM) with respect to the chip. Linear polarisation modes are assumed in this thesis, which is a good approximation for PM fibers and large Si rib

waveguides. Then PXR_{out} can be measured as the ratio of powers transmitted through a linear polariser aligned along the two polarisation axes. This PXR value depends on input coupling (PXR_{in}), polarisation cross-talk in the fiber and the order of the modes (P_1/P_2 or P_2/P_1). The PXR of the fiber itself is defined as its PXR_{out} (>1) when PXR_{in} = 0 or ∞. In practise, accurate characterisation of devices requires that PXR_{in} >> PXR_{out} and that the rotational misalignments at the input and output are kept well below arctan(1/PXR_{out}).

In general, PXR(α) is the ratio of powers P_1 and P_2 transmitted through a linear polariser in two orthogonal angles α (P_1) and α+90° (P_2). It describes the PXR_{in} that would couple to a fiber rotationally aligned to angle α. If α is the angle with respect to a fiber's polarisation axis,

$$\mathrm{PXR}(\alpha) = \frac{\mathrm{PXR_{out}} + 2\sqrt{\mathrm{PXR_{out}}}\,\tan(\alpha)\cos(\Delta\phi) + \tan^2(\alpha)}{\mathrm{PXR_{out}}\,\tan^2(\alpha) - 2\sqrt{\mathrm{PXR_{out}}}\,\tan(\alpha)\cos(\Delta\phi) + 1}, \qquad (12)$$

where PXR_{out} and $\Delta\phi$ are the PXR and the phase difference of the polarisation modes at the fiber's output. This formula was used to analyse the changing of PXR due to rotationally misaligned junctions, and to explain the measured PXR(α) curves. It is illustrated in Fig. 26 and it led to the invention of a novel method for measuring the polarisation axes of waveguides and polarisation maintaining fibers. According to the proposed method, two or more PXR(α) curves are measured and their crossing point determines the angle of a polarisation axis (α = 0°). In this method, $\Delta\phi$ does not need to be known or densely varied. It suffices to change it enough for the identification of the crossing point(s), e.g. by ±45°, or more. Changes can be induced by heating, bending or stretching the fiber (or waveguide), or by slightly changing the wavelength. If some interpolation or fitting to theoretical curves is used, the measurement accuracy can be much better than the angular step size. Also, the measurement accuracy of this method can be estimated based on curve fitting and/or deviation of crossing points between multiple PXR(α) curves.

It should be noted that if $\Delta\phi$ is properly averaged out, e.g. by using a sufficiently broadband light source, then PXR(α) corresponds to $\Delta\phi$ = 90°. For light propagating in free space, there are no modes or polarisation axes, and PXR is usually defined as the maximum of a measured PXR(α) curve. Sometimes this definition is also used to determine PXR_{out} of a fiber or a waveguide. However, based on Eq. (12) and Fig. 26 this should be used only if $\Delta\phi$ is averaged out. Otherwise the maximum PXR(α) indicates a false angle and a false PXR_{out}.

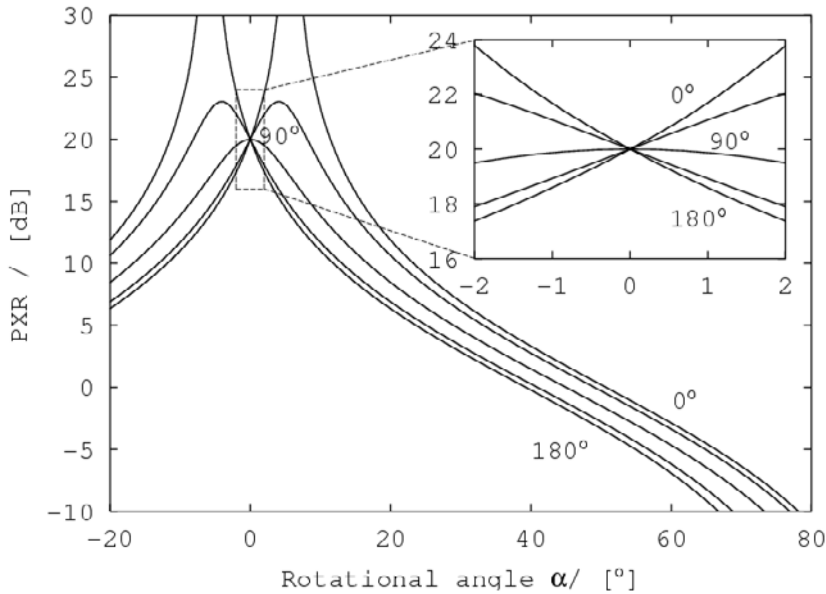

Figure 26. Theoretical PXR curves based on Eq. (12). PXR_{in} = 20 dB and $\Delta\phi$ = 0°, 45°, 90°, 135°, or 180°.

As can be concluded from Eq. (12) and Fig. 26, the rotational misalignment of a fiber with respect to the input of a Si waveguide rapidly increases the variation of the waveguide's input PXR with respect to $\Delta\phi$, which is usually unknown and unstable. Therefore, the rotational alignment should be carried out very accurately, especially in case of multiple successive junctions between different PM components.

Proper input alignment alone does not guarantee high PXR_{out} for a Si waveguide. The polarisation cross-talk within the waveguide or the waveguide component must also be minimised. Careful PIC design can minimise unwanted modal coupling in bends, tapers and other circuit elements. However, material inhomogeneities, surface roughness around the core and other process-related imperfections induce scattering losses, and some of the scattered power tends to couple to the other polarisation. This type of cross-talk can be minimised by decreasing the propagation losses and by increasing the waveguide birefringence.

3. Fabrication

3.1 Clean-room processing

The fabrication of waveguide components was mostly based on standard clean-room processes and tools that are commonly used in silicon microfabrication. An up-to-date introduction to microfabrication can be found from [105]. The basic principle of photolithographic patterning is illustrated in Fig. 27. A short summary of the used tools and methods is given in this chapter. Due to the numerous variations of processing, a default process for fabricating an SOI waveguide chip is first described and the main variations with respect to that are then briefly listed.

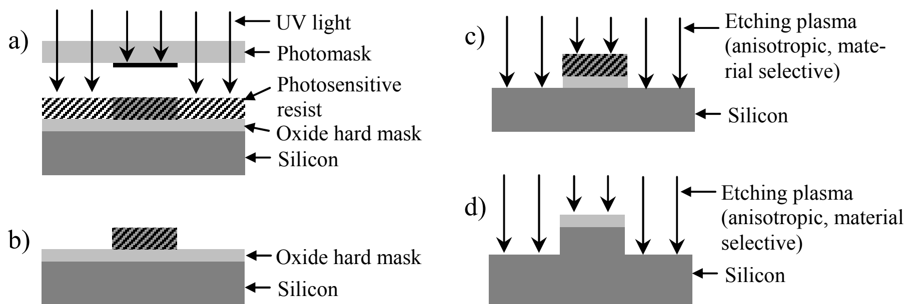

Figure 27. Schematic presentation of photolithographic surface patterning with an oxide hard mask (dimensions not in scale). a) UV exposure. b) Resist development. c) Oxide dry etching. d) Si dry etching.

The default waveguide process is based on photolithographic patterning and the use of an oxide hard mask (see Fig. 27). First, approx. 300 nm thick oxide hard mask is deposited with low temperature oxide (LTO) process in a chemical vapour deposition (CVD) furnace on top of a BESOI wafer with SOI thickness ~10 µm. Waveguide patterns are then transferred to the hard mask using standard photolithography and dry oxide etching in parallel plate plasma etcher. Silicon etching is done using an inductively coupled plasma (ICP) type reactive ion etcher (RIE). The etching process is modified from a pulsed (Bosch) type process for deep silicon etching, in which etching and passivation steps are alternated subsequently. The etching and passivation gases are SF_6 and C_4H_8, respectively. During the passivation step a thin polymer film is deposited on the etched silicon side-walls to prevent lateral etching under the mask and thus keeping the etched wall vertical. The passivation and etching step lengths are reduced to their minimum (5 s) to minimise the depth of the unavoidable side-wall undulation in this process. The process is started by etching the first 500 nm with continuous passivation to prevent the significant underetching in a first etch cycle when no passivation is yet present. The resulting etch wall roughness after Si etching is shown in Figs. 28a–b. After the removal of the resist and the passivation polymers in oxygen plasma, the oxide mask is removed

by wet etching in hydrofluoric acid. The final process step is the deposition of the top cladding oxide. By default, the cladding is formed by thermal oxidation, which also reduces surface roughness on waveguide walls. The default TOX thickness is 1 µm.

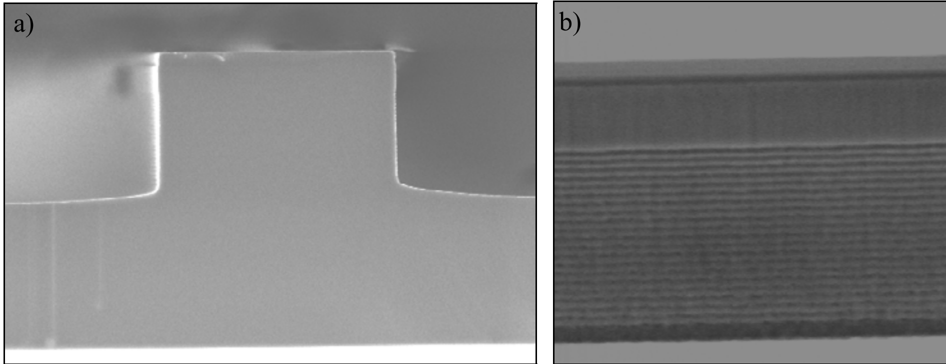

Figure 28. Scanning electron microscope (SEM) images of SOI rib waveguides fabricated with the default process, but before cladding oxide deposition. a) Cross-section (white area is the BOX layer). b) Side wall (undulation due to the pulsed process).

To eliminate the slight undulation in waveguide walls, a continuous passivation process may alternatively be used. In this case, the flow rate of the passivating gas (C_4F_8) is increased linearly as a function of time, instead of pulsed operation. In this process, the maximum achievable etch depth is presently limited to ~6 µm with acceptable side wall verticality. There are alternatives to the TOX top cladding as well. For example, low pressure CVD of oxides, such as tetraethyl orthosilicate (TEOS) and LTO, can be used, or the cladding deposition can be simply skipped. For fabricating TO switches, thin film metal heaters must be processed on top of the rib waveguides. By default, a 500 nm thick Al layer was sputter deposited and patterned using standard photolithography and dry etching.

In order to enable the future demonstration of functional multi-step waveguide structures, a three-step fabrication process was also developed. The process is schematically presented in Fig. 29. First the default waveguide process is applied for the first etch step (deepest areas in the final structure). Then a new mask oxide is deposited and patterned to define the layout for the third etch step. This structure is not immediately transferred to Si, but a new photoresist layer is applied and patterned on top of it. The second etch step is done using the photoresist mask. Then the photoresist is stripped off and the exposed oxide hard mask is used to carry out the third etch step. The different combinations of the three mask layouts (etch steps 1–3) can produce six final Si levels (no etch, etch 1, 3, 1+3, 2+3, or 1+2+3). Examples of fabricated test structures are shown in Fig. 30. When applied to functional waveguides on SOI wafers (see Chapter 2.6), these structures should provide adiabatic operation as long as the different mask lines have sufficiently small crossing angles with respect to each other.

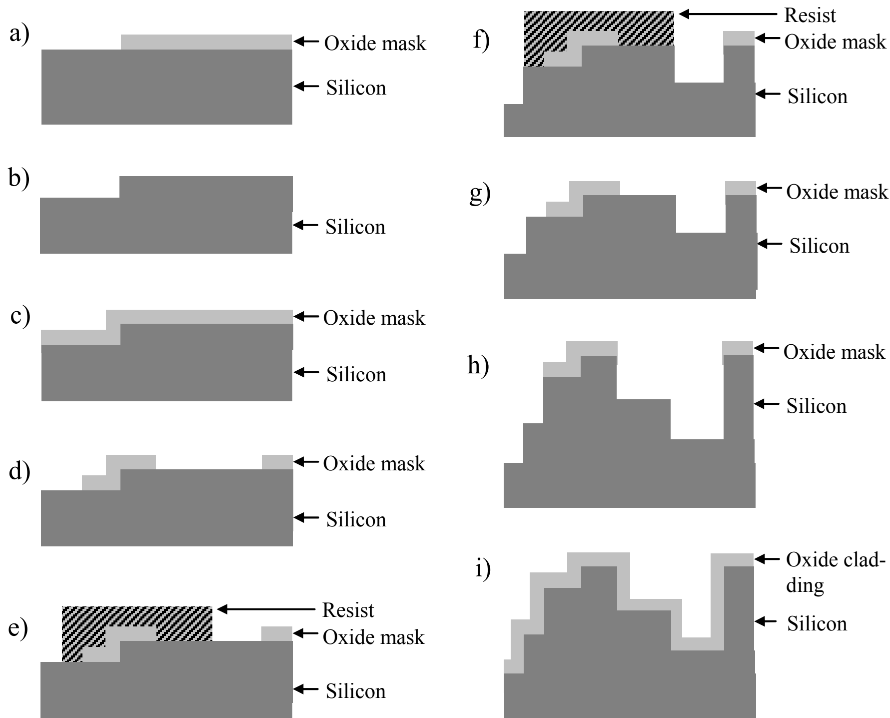

Figure 29. Schematic presentation of a multi-step process (3 etch steps, dimensions not in scale). a) Oxide patterning with photomask 1. b) Silicon etching with oxide mask and oxide removal. c) Oxide deposition. d) Oxide patterning with photomask 3. e) Resist patterning with photomask 2. f) Si etching with resist mask. g) Resist removal. h) Silicon etching with oxide mask. i) Final structure after oxide removal and thermal oxidation.

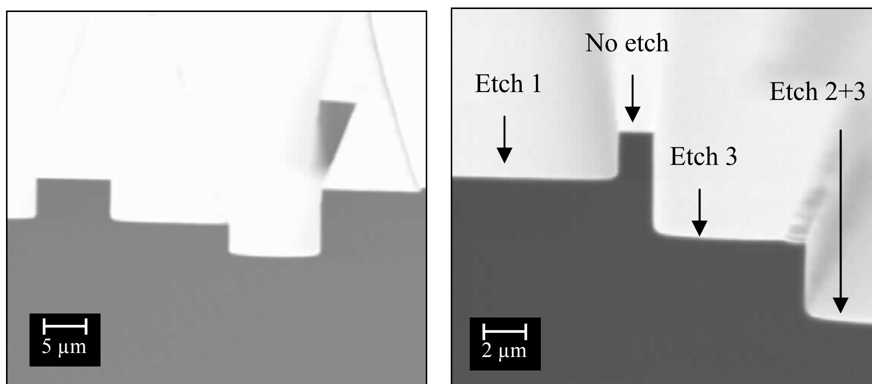

Figure 30. SEM images of fabricated multi-step test structures on Si wafers. The different combinations of etch steps are indicated on the right.

3.2 Post-processing and fiber pigtailing

Between the clean-room processing and sample characterisation, some post-processing is usually required. In this work, the main post-processing steps were wafer dicing (into chips), polishing of the chip facets to optical quality and wire bonding of electronic contacts to TO switches. Dicing was carried out with a Loadpoint MicroAce 3 machine. An improved dicing method was developed for optical samples in order to ease the polishing process.

In the beginning of this work, chip polishing was carried out by using diamond sprays and rapidly rotating polishing cloths. This process was slow and it only provided moderate surface quality. Therefore, better polishing equipment was purchased and a new polishing process was developed for SOI waveguide samples. With the latest process, fine tuned by another person at VTT, a chip facet with an array of SOI waveguides can be polished to excellent quality in less than half an hour. One key factor in a successful polishing process is that the chip surface is protected with a thick resist layer until the final chip cleaning. In order to characterise the TO switches the contact pads on the chips were wire-bonded to external electronics.

In this work, single-layer AR coating technology was developed to reduce reflections in fiber-waveguide junctions. Three coating materials were tested, namely Ta_2O_5 (n = 2.1), HfO_2 (n = 2.03), and ZrO_2 (n = 2.13). All three materials were grown by atomic layer deposition (ALD), but the first two were deposited at the University of Helsinki, while ZrO_2 was deposited at the Helsinki University of Technology. Lowest reflections were measured with an AR coating made of Ta_2O_5. However, the variation of measured reflection coefficients between different materials and samples was dominated by thickness variation, not the refractive index differences. The thicknesses were not thoroughly calibrated in this work. Nevertheless, it should be noted that in series production the ALD thickness uniformity is usually excellent and all the three materials are applicable for AR coatings. Another, and perhaps even more important, advantage of ALD is excellent conformality (step-coverage).

Some waveguide samples were equipped with fixed fiber pigtails, and even with fiber arrays. First, fibers were passively aligned onto Si V-groove chips and fixed with UV-curable glue and glass lids. Then these fiber sub-assemblies were polished and actively aligned to the waveguide chips. Finally, the aligned end facets were fixed together with UV-curable and index-matched glue.

3.3 Waveguide gratings and photonic crystal structures

The experimental part of the waveguide grating development was started in the very beginning of the whole research work, in parallel with the study of thermo-optical switching. Therefore, this work did not only concentrate on the waveguide gratings themselves, but it also involved a significant amount of fundamental development with respect to the processing of plain silicon waveguides and various types of silicon nanostructures with the help of both optical and electron (e)-beam lithography [VII, 62, 70].

As was explained in chapter 0, the target for process development was to realise up to 500 nm deep corrugated gratings on top of an SOI rib waveguide and the nearby slab regions (refer to Fig. 25b). The design for process integration involved the patterning of wide gratings onto an SOI wafer, the patterning of an oxide hard mask on top of the grating and, finally, the etching of silicon around the rib to the desired depth, so that the grating around the rib would be replicated on top of the slab. The fabrication processes for rib waveguides and gratings were first develop separately, while bearing in mind the requirement for process integration in the future. The developed waveguide process was similar to the above described default process and its detailed description can be found from publication VII. The grating process was first intended to be carried out mostly at JoFy in Joensuu, but it was found out that such a process formed a contamination risk to the CMOS fabrication line at VTT. Most of the fabrication steps were then moved to VTT's facilities in Espoo and only the critical e-beam lithography step was done at JoFy. Numerous processing tests were done with different mask layers and etch processes, but first order gratings with 225 nm period could not be fabricated with sufficient quality because of an artefact in e-beam writing. The varying e-beam dose resulted in linewidth and, consequently, etch depth variations (see Fig. 31a). However, second and third order gratings (450 and 675 nm periods) with over 1 μm etch depth were successfully realised on plain Si wafers (see Fig. 31b).

After developing the waveguide and grating processes separately, they were combined with the designed integration process. First and third order grating structures were fabricated on top of silicon ribs on both Si and SOI wafers (see Fig. 31c). Unfortunately, the gratings around the ribs had poor quality. Apparently, the replication of the surface corrugation from the original Si surface to the lower slab surface by using anisotropic silicon dry etching around the rib was not successful. Residual hard mask oxide in the grating grooves at the beginning of the deep Si etching was at least one of the reasons for this. The high quality of third order gratings was maintained on top of the ribs, but the gratings on the sides did not have sufficient quality for successful optical measurements. However, the obtained ability to realise over 1 μm deep gratings opened up the possibility to apply gratings only on top of the ribs in future experiments.

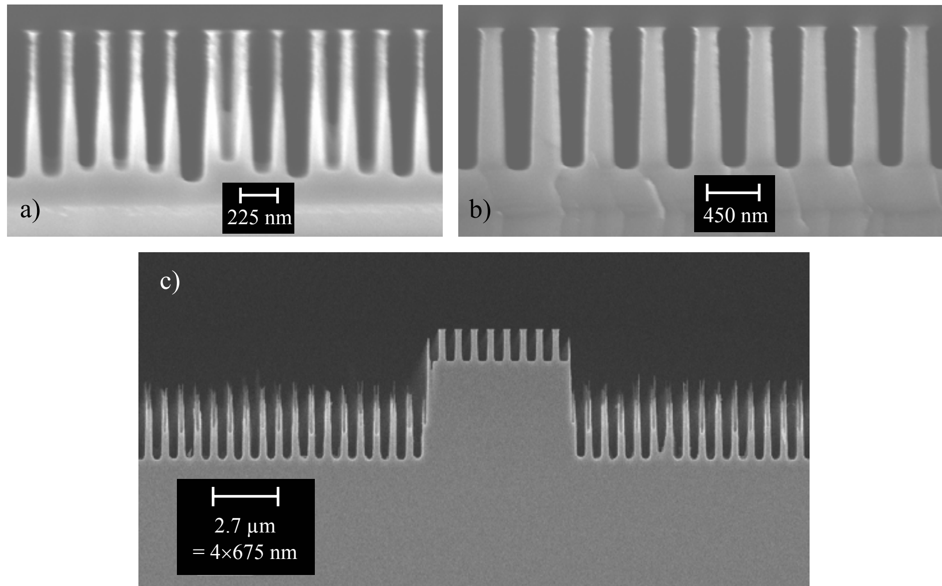

Figure 31. SEM images of fabricated grating test structures. a) Grating on a Si wafer with period 225 nm and depth ~1 µm. b) As above, but with 450 nm period and 1.2 µm depth. b) Parallel grating on top of a Si rib structure with period 675 nm and depth 1.2 µm (fabricated only for SEM analysis).

The success of fabricating nanostructures on flat surfaces enabled the fabrication of photonic crystal components on 1 µm thick SOI wafers. This was indeed carried out successfully [70, 84]. Some PhC waveguide structures fabricated in SOI are illustrated in Fig. 32. To enable the optical characterisation of these tiny PhC waveguides in the future, input and output coupling of light should still be developed. The structure illustrated in Fig. 23a may turn out to be useful for this purpose.

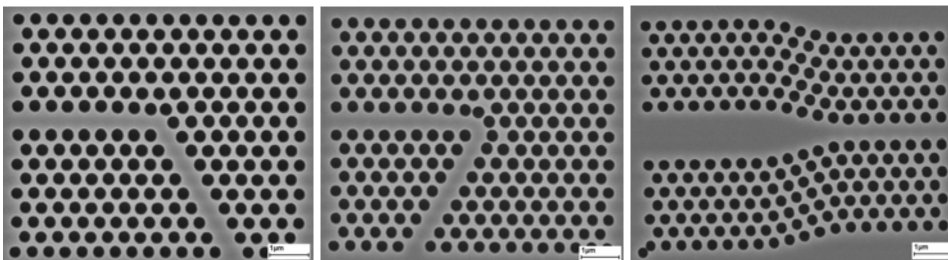

Figure 32. SEM images of PhC waveguide structures fabricated in SOI by using a single e-beam exposure window: a) 60° bend, b) 120° bend, and c) taper.

4. Experimental results

4.1 Construction of the measurement set-ups

In the beginning of this work, measurements were carried out with an unstable 6-axis alignment stage, standard SM and MM fibers (SMF, MMF), rotatable thin-film polarisers, standard objectives and an IR camera. This resulted in many problems, including difficult fiber alignment and unexplained polarisation effects. Therefore, a rigid 3-axis alignment stage with piezo drives (NanoBlock from Melles Griot), a computer controlled 6-axis stage (Model F-206 from PI), PM fibers (PMF, from Flextronics), a fiber pigtailed polariser (from General Photonics), two free-space polarisers (PXR 50 dB, from Thorlabs), a PM fiber coupler (from Newport), two PM 1×2 switches (from Newport), two polarisation splitters (from OZ optics), and a new IR camera with near-field optics were purchased. Furthermore, a motorised fiber rotator was fabricated by a student from The Finnish School of Watchmaking under author's supervision. With these tools, new setups for loss and polarisation measurements were constructed. The basic setups are illustrated in Figs. 33–34 (alignment tools not shown), although some modifications were made for particular measurement needs.

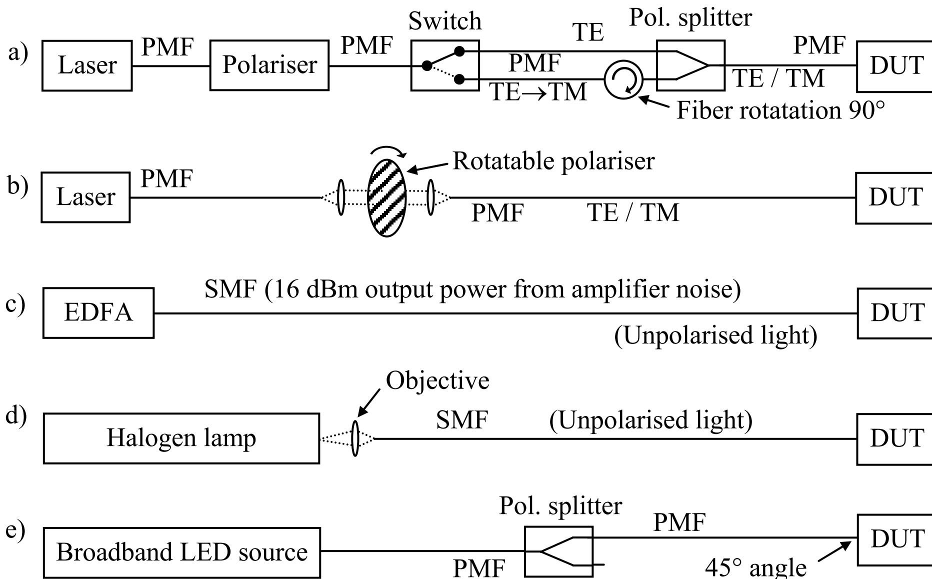

Figure 33. Typical measurement setups used for optical input coupling. a–b) TE/TM polarised input for insertion loss (IL), PDL, PXR, and polarisation axis measurements. c) High power input for IL measurements. d) Input for spectral measurements. e) Polarised broadband input for birefringence measurements. EDFA = erbium doped fiber amplifier, DUT = device under test.

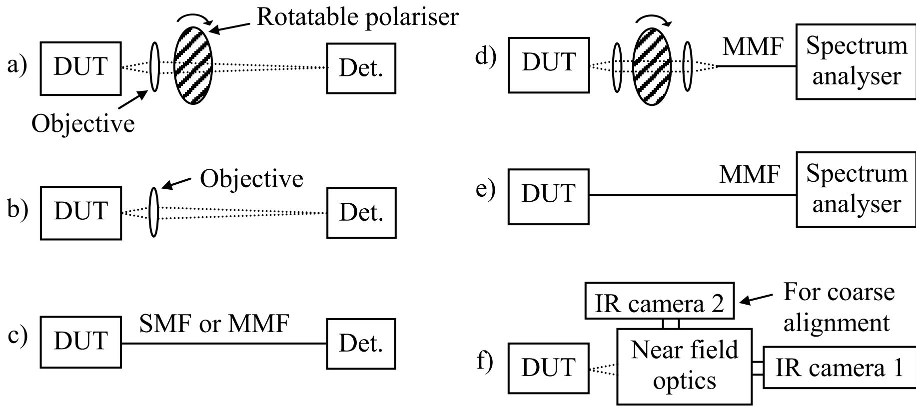

Figure 34. Typical measurement setups used for optical output coupling in measurement of a) polarised output power and PXR, b) output power in free-space, c) output power with SMF or MMF, d) PXR spectra for birefringence measurements, e) spectral characteristics and f) near-field intensity distributions. Det. = detector.

Compared to the old setups and methods, the new setups provided significantly better measurement accuracy. This also led to much better consistency with the theory and simulations. High quality polishing of the waveguide facets (see Chapter 3.2) and the use of index matching oil between fibers and waveguides were also found to be crucial for obtaining reliable results.

4.2 Optical coupling of fibers and silicon waveguides

Silicon rib waveguides were optically coupled with standard SM, MM and PM fibers. The coupling efficiency to MM fibers is practically 100%, excluding the reflection losses. Modal mismatch between a Si rib waveguide and a standard SM fiber was determined by measuring the insertion losses (IL) of 3 mm long waveguide chips between SM input and output fibers. Due to the short waveguide length the propagation losses are negligible (<0.1 dB) with respect to the coupling losses, and the worst-case coupling loss estimate for a single fiber-waveguide junction is IL/2, including the reflection losses. The reflection losses were suppressed to 0.8±0.05 dB/facet by using index matching oil (n = 1.5) between the fiber and the waveguide. To estimate the modal mismatch loss, 0.75 dB/facet reflection loss was subtracted from IL/2 (interference effects should be very small with the used light source). For 9 µm thick test waveguides with $h/H \approx 0.48$ the measured minimum modal mismatch loss was 0.6 dB with $W \approx 12$ µm (width variation in 1 µm steps). According to rigorous overlap calculations for the same H and h, minimum losses of 0.541 and 0.584 dB for TE and TM, respectively, should be obtained at $W \approx 13$ µm. Thus, the calculated and measured values agree very well.

The impact of AR coatings in reducing the reflection losses was measured with 4 cm long waveguide chips. In order to eliminate the somewhat uncertain propagation losses (0.2–0.8 dB), insertion losses for the waveguides were measured before and after AR coating deposition. Index matching oil was used for both measurements, and the IL reduction after AR coating was compared to the calculated loss reduction. The best results were obtained with Ta_2O_5 AR coatings and they are summarised in Table 1. The average loss reduction was 0.8 dB/facet with a 0.12 dB standard deviation (due to the finite measurement accuracy). The calculated loss reduction was 0.7 dB for a 180 nm thick Ta_2O_5 coating. This thickness was measured from a reference sample, and it may slightly deviate from the real thickness. Thus, the calculated and measured values again agreed very well. Based on the results and the calculated 0.8±0.05 dB reflection loss without the AR coating, the reflection loss with the AR coating is estimated to be <0.15 dB. Thus the total coupling loss for a 9 µm thick waveguide with AR coating and optimum alignment is estimated to be <0.75 dB/facet. Even lower coupling loss should be attainable with an optimised AR coating thickness and a thicker waveguide. With an optimal Ta_2O_5 coating and a 14×14 µm strip waveguide, the coupling loss could be as low as 0.1 dB/facet.

Table 1. Insertion losses (dB) of Si rib waveguides between standard SM fibers with and without Ta_2O_5 AR coatings, and the insertion loss reduction (dB) due to the AR coating. LWC = line width change with respect to the nominal W on the mask layout.

	H (µm)	*h*/*H*	LWC (µm)	Nominal *W*: 14 µm	13 µm	12 µm	11 µm	10 µm
Without Ta_2O_5	9.1	0.35	-2	3.0	3.2	3.2	3.3	3.8
With Ta_2O_5				1.8	1.4	1.9	1.8	2.0
IL reduction				1.2	1.8	1.3	1.5	1.8
Without Ta_2O_5	8.5	0.38	-2.3	3.2	3.1	3.4	3.7	3.8
With Ta_2O_5				1.9	1.7	1.6	1.8	2.3
IL reduction				1.3	1.4	1.8	1.9	1.5

Coupling with PM fibers was also tested. To obtain good input PXR the polarisation axes of the waveguides and fibers were accurately aligned parallel. The polarisation axes of a Si waveguide are usually parallel and transverse to the chip's surface and, thus, easy to align with respect to the setup. However, the polarisation axes at plain fiber ends need to be directly measured. After the measurement the fiber axes can be rotated parallel to the waveguide axes and the positional alignment can be started. In this work, two alternative methods were used to find the polarisation axes of PM fibers. In the first method, broadband light source was used to average out the phase differences between the polarisation modes. Thus, the maximum and minimum of PXR(α), as measured by a rotatable polariser, indicated the angles of the polarisation axes. Due to its simplicity and sufficient accuracy, this method was usually used. However, the practical applicability of the new measurement method, as introduced in Chapter 2.8, was also demonstrated [VIII].

The new measurement method was tested by using three alternative means to induce phase difference changes in a PM fiber. All three led to good results, but heating provided slightly better accuracy than wavelength tuning and mechanical fiber manipulation. The improved accuracy was mostly due to the motorised fiber rotator, which was used only in the heating experiments. It was not yet available when the other modulation methods were tested. Fitting to theoretical curves was good for temperature and wavelength tuning, but rather poor for the mechanical fiber manipulation. This was due to the uncontrolled and unexpectedly long stabilisation time of microscopic fiber movements, which induced phase fluctuations during the angular scan. With temperature modulation the measured PXR(α) curves fitted well to theory and provided a measurement accuracy of better than 0.2°, as can be confirmed from Fig. 35.

When compared to alternative methods [118–121], the new method has some unique advantages. Unlike the broadband method, the new method can be applied also to devices with a very narrow spectral range, such as arrayed waveguide gratings (AWGs) or wavelength filters. Compared to the use of polarisation analysers, or other complicated equipment, the new method is particularly simple and inexpensive to implement. Some alternative methods are based on measuring PXR(α) continuously with a fast rotating polariser. However, with these method one needs to vary both α and $\Delta\phi$ with very small steps. The accuracy of the new method appears to be at least as good as for any other method, and it can be easily confirmed from the results.

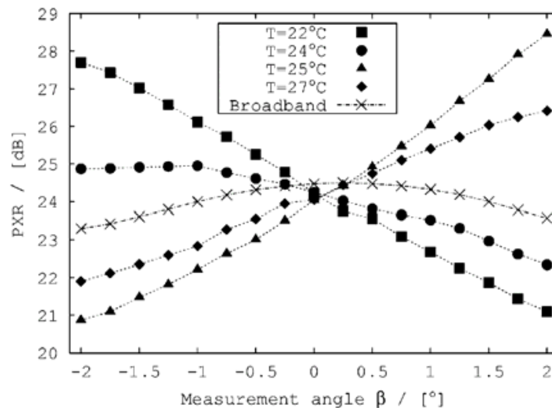

Figure 35. Measurement of a PM fiber's polarisation axis by heating the fiber (filled symbols) and by using a broadband light source (thin crosses).

Finally, fixed fiber pigtails were fabricated by using a combination of passive fiber alignment into Si V-groove chips and active alignment between the fiber array and waveguide array chips (see Fig. 5a). This was done for both SM and PM fibers. For PM fibers the output PXR of the fiber array was limited to ~17 dB, even if the fiber alignment was done with very high accuracy. This was probably due to the stress induced into

the PM fibers when they were permanently affixed to the V-grooves with UV-curing glue and a pyrex lid. For SM fiber arrays the fixed fiber pigtails increased the coupling losses by <0.5 dB/facet with respect to the optimum alignment of single fibers. Thus, the misalignments in a fiber array were <1.5 μm according to Fig. 17.

4.3 Propagation and bending losses of silicon waveguides

Accurate measurement of the propagation losses in low-loss Si rib waveguides is quite difficult. In this work, 4" SOI wafers were used, providing a maximum length of 9 cm for straight waveguides. For 9 cm long waveguides with 0.1–0.5 dB/cm attenuation the total propagation loss is comparable to the somewhat uncertain coupling losses. Also, low-loss light propagation in the surrounding slab makes it difficult to separate the powers associated with the fundamental, higher order and radiation modes at the output of short waveguide samples. Thus, the usual cut-back method [77, 79] does not provide very accurate results for low-loss waveguides. On the other hand, the very high effective index requires that short waveguides should be used in the alternative Fabry–Perot loss measurement [77, 79]. Then the scattering losses at the waveguide end facets induce uncertainties in the loss measurements.

In order to measure the propagation losses accurately, up to 114 cm long spiral waveguides were fabricated on 100 mm SOI wafers. A schematic layout of the spiral is shown in Fig. 36. Nominal waveguide width varied from 2 to 11 μm, and the bending radius varied between 25 and 42 mm along the spiral. The minimum radius of 25 mm is still quite short for weakly guided Si rib waveguides with $H \approx 9$ μm and $h/H \approx 0.5$, and the bending losses have some effect on the measured propagation losses. Also, each waveguide made 100 crossings with other waveguides. Thus, the measured losses are a worst-case estimate. However, the impact of fiber coupling and interference effects is almost completely eliminated in the very long waveguides, and the insertion loss of perpendicular crossings is very small (<0.05 dB/crossing based on the results). Reflection loss with index matching oil is only 0.8 dB/facet, while even the smallest measured IL was ~15 dB. To obtain the propagation loss, 0 and 1.6 dB losses were assumed for crossings and reflections, respectively. Also, the calculated modal mismatch loss was subtracted from the IL.

Most of the results were obtained with a high-power EDFA source (Fig. 33c) and SM or MM fibers at the output (Fig. 34c). Some polarisation measurements were carried out with a laser source and PM fibers (Figs. 33a and 34a). The waveguides were confirmed to be SM by monitoring the output with an IR camera while moving the input fiber. Straight waveguides with same dimensions were often seen to be multi-moded because the bends eliminate weakly guided higher order modes. In practise, wider waveguides can, and should, be used in bends.

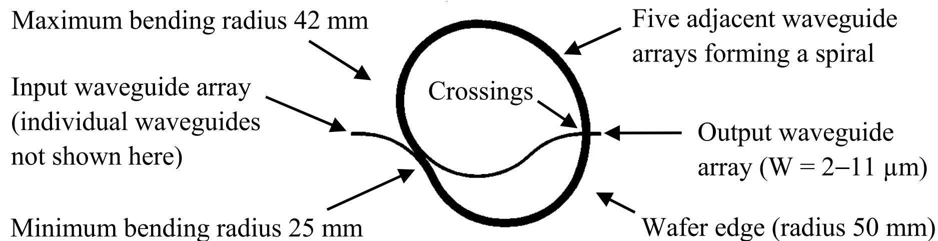

Figure 36. Schematic layout of the waveguide spiral test structure used to determine the propagation losses of Si rib waveguides.

The measured minimum propagation loss for 114 cm long and 9 μm thick SM rib waveguides between two SM fibers was 0.13±0.01 dB/cm. This waveguide was fabricated with the continuous passivation process. It had $h/H \approx 0.44$, $W \approx 7$ μm, and a calculated modal mismatch of 1.2 dB/facet. According to Eq. (6), the maximum SM width is 7.4 and 7.2 μm for TE and TM, respectively. Thus, the waveguide was SM also according to Eq. (6). The obtained propagation loss is the best reported so far in literature for a dry etched Si rib waveguide at $\lambda \approx 1550$ nm. Also, the measurement accuracy is much better than in previous results at $\lambda = 1300$–1550 nm. For example, in [72] the propagation loss at $\lambda = 1.52$ μm is reported to be 0±0.5 and 0.4±0.5 dB/cm for TE and TM, respectively.

Propagation losses were also measured as a function of wavelength for 9.0, 4.9, and 2.0 μm thick SM waveguides. For a 9.0 μm thick spiral waveguide the propagation loss was practically constant (0.13–0.16 dB/cm) from 1200 to 1650 nm. For $H \approx 4.9$ μm and $H \approx 2.0$ μm the minimum propagation loss measured from a 71 mm long straight waveguide was 0.3±0.2 dB/cm and 1.2±0.2 dB/cm, respectively. To obtain these values the calculated modal mismatch and reflection losses were subtracted from the measured insertion losses. This reduced the measurement accuracy of thin and straight waveguides compared to the thick spiral waveguides. However, it can be clearly seen that thinner waveguides have higher propagation losses due to their higher sensitivity to surface roughness. The measured transmission spectra are shown in Fig. 37.

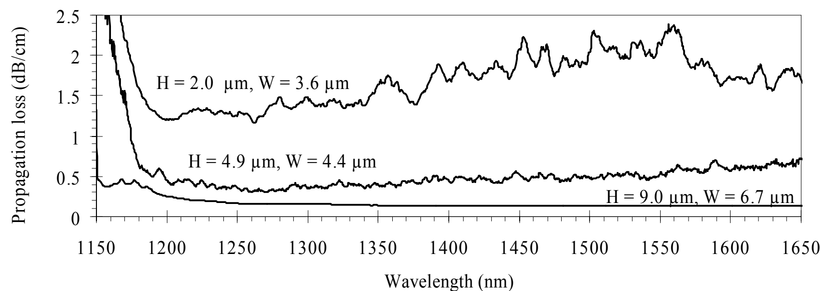

Figure 37. Measured propagation loss spectra for single-moded 9.0, 4.9, and 2.0 μm thick Si rib waveguides.

4.4 Polarisation characteristics of Si waveguides and directional couplers

The birefringencies of different Si rib waveguides were measured by using the fixed analyser method [122]. The used input and output setups are illustrated in Figs. 33e and 34d, respectively. The results are also described in publication [I] and Ref. [63]. In the measurements both polarisation modes of the waveguide were equally excited ($PXR_{in} \approx$ 0 dB) from an input PM fiber having high PXR and a rotational 45° angle with respect to the waveguide. At the output, a PXR spectrum was measured, again at 45° angle with respect to the waveguide. Waveguide birefringence induces a periodic variation of measured PXR as a function of λ, and the birefringence can, thus, be concluded from the measured λ-period and sample length. Examples of measured PXR spectra and birefringence values as a function of rib width W are shown in Fig. 38. Measurements were carried out for 9 µm thick rib waveguides with different widths and cladding materials ($h/H \approx 0.5$). The main conclusion was that typical cladding oxide materials (n ≈ 1.5), such as TOX and LTO, can increase the birefringence almost by an order of magnitude compared to an air cladding. This must be due to the stress induced by the cladding into the Si core [I, 63, 95]. A low-stress TEOS cladding indeed provided almost as low birefringence as the air cladding, although both values were at the limits of measurement accuracy. A summary of the results is given in Table 2. [I]

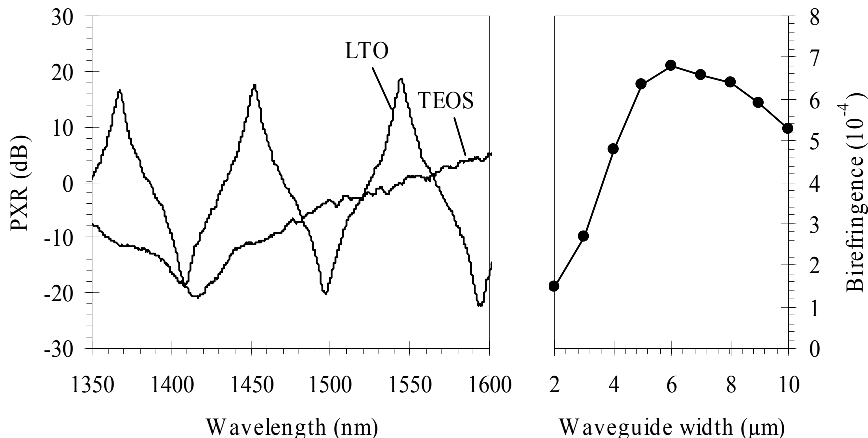

Figure 38. a) Measured PXR spectra from two 4 cm long waveguides with LTO and TEOS claddings ($H \approx 9$ µm, $h/H \approx 0.5$, $W \approx 8$ µm). b) Measured birefringence as a function of W in a 71 mm long sample chip with TOX cladding ($H \approx 9$ µm, $h/H \approx 0.5$).

Waveguide width can also be used to tune the birefringence, but this may produce conflicts with other design criteria, such as low-loss and SM operation. However, by choosing an appropriate cladding material and by fine tuning cladding thickness, waveguide width and etch depth, one should be able to tune the birefringence continuously from

very small values (polarisation independent operation) to very high values (PM operation). Some variations can also be done within a single chip to monolithically combine waveguides with different polarisation characteristics. Finally, it should be noted that in thin waveguides birefringence usually increases [93, 95] and becomes a more difficult problem.

Table 2. Calculated and measured birefringencies of rib waveguides with different cladding materials, all with H ≈ 9 µm, h/H ≈ 0.5 and W ≈ 8 µm. Calculated values do not include stress-induced birefringence, unlike the measured values.

	Calculated:		Measured:			
Cladding material:	Air	SiO_2	Air	TEOS	LTO	TOX
Birefringence (10^{-4}):	0.236	0.238	<1	1	6	6.3

For realising polarisation independent devices it is not always sufficient to minimise birefringence only. After all, birefringence-induced PMD is usually not very significant in the relatively short waveguide chips. Instead, the polarisation dependency of all optical circuit elements, such as directional couplers and modulators, must be minimised, although there is usually a strong correlation between birefringence and the polarisation dependency of components. In this work, the polarisation dependency of directional couplers was tested for different cladding materials, namely air, TEOS, LTO and TOX. According to the results, there was indeed a strong correlation with birefringence. Air and TEOS claddings provided polarisation independent DC operation, while LTO and TOX caused a strong polarisation dependency. Therefore, LTO and TOX should not be used for polarisation independent applications.

Birefringence measurements indicate that LTO and TOX claddings could be used for PM applications, particularly if only one polarisation is used. However, such applications require a sufficient PXR value for waveguides and waveguide components, such as DCs. Therefore, the PXR of straight Si waveguides and DCs was measured. The PXR of the input fiber was >30 dB and the polarisation angles were accurately aligned with the methods described in Chapter 2.3. Furthermore, the input angle was iteratively varied in order to confirm optimum alignment. Output PXR was measured with both the broadband method and the new crossing point method. However, the maximum output PXR of both straight waveguides and DCs was only slightly over 15 dB. This value is rather low, although sufficient for some applications. It is estimated that the relatively low PXR is due to scattering, which is also responsible for propagation losses. A certain fraction of the scattered light is coupled to the opposite polarisation state, and the PXR can only be improved by further reducing the propagation losses. This conclusion is supported by the fact that in a 4 cm long waveguide with 0.15 dB/cm loss 13% of the input power is scattered away from the waveguide, while PXR = 15 dB corresponds to 3.6% of the same input power having coupled to another polarisation state.

4.5 Fast thermo-optic 2x2 MZI switch

First thermo-optic 2×2 MZI switches were fabricated directly after the switch and mask design (see publication III and Chapter 2.5). However, the initial characterisation of the switches [28] was not easy, because the pre-existing measurement setup was somewhat unstable, the input polarisation was arbitrary, and the quality of the waveguide facets was rather poor. Also, the unprotected Mo thin film heaters experienced corrosion and the heating of the waveguide chip influenced the fiber coupling efficiency at the input due to the thermal expansion or warping of the chip. The measurement setup and the facet polishing process were then improved, as explained in Chapters 4.1 and 3.2, respectively, and heatsinks were attached to the waveguide chips. This stabilised the power and polarisation at the input. Furthermore, waveguide processing was developed further to reduce scattering losses, and ~200 nm thick Mo heaters were replaced with 500 nm thick Al heaters. The final dimensions of waveguides were $H \approx 9$ µm, $h \approx 5$ µm, and $W \approx 9$ µm. Waveguide spacing was 250 µm at the input, output and heating area, and 11 or 12 µm in the directional couplers. A bending radius of 12 cm was used for the S-bends to induce transverse offsets of ~120 nm, and the lengths of the DCs were varied between 0 and 4 mm. This led to a total chip length of 4 cm. For more details on switch processing, see publications I and IV–V, and Chapter 3.1. After the development described above, new switches were fabricated and characterised. As the DCs were polarisation dependent (see Chapter 4.4), only TE polarisation was used for the characterisation (setup as in Figs. 33a and 34c). Details of switch modulation can be found from publications I and IV–V.

First, the MZI switches were characterised without heating. The best switches had an output extinction ratio ER = $|10\log(T_{CROSS}/T_{BAR})| \approx 17$ dB (98:2), where T_{CROSS} and T_{BAR} are the relative powers from the two switch output ports (BAR and CROSS with respect to the input port). This was partly due to the very coarse variation of DC lengths on the mask. For example, only lengths 0, 1, 1.5, 2, and 3 mm were available for 11 µm waveguide separation. Therefore, the measured maximum ER does not indicate the maximum for SOI-based MZI switches in general.

Heating contacts were wire bonded to the best switches, which were then characterised with externally applied control signals. First, the voltage over a single heater was slowly increased in order to determine the minimum and maximum transmissions for both output ports. The minimum and maximum were obtained with heating powers $P = 0$ W and $P = P_{ON} = 300$ mW, respectively. Same 17 dB extinction ratio was found for the ON and OFF state ($\Delta\phi = 0$ or π). However, the ER of a lossless and symmetric MZI should be infinite for the ON state [III]. Therefore, the ER is not limited only by the DC lengths, but also by scattering, inter-modal coupling, limited PXR or some other imperfection. If we assume that a fixed fraction s of total output power is always divided equally to both outputs, e.g. due to scattering, then the relative CROSS port transmission (or portion of total output power if the switch has an excess loss) is

$$T_{\mathrm{CROSS}} = \frac{1}{2}\sin^2\left(\frac{r\pi}{2}\right)[1+\cos(\Delta\phi)](1-s)+\frac{1}{2}s\ , \tag{13}$$

where r is the ratio of real and ideal DC length. Relative transmission to the BAR port is $T_{\mathrm{BAR}} = 1-T_{\mathrm{CROSS}}$. The maximum and minimum transmissions $T_{\mathrm{CROSS,max}}$ and $T_{\mathrm{CROSS,min}}$ are obtained at $\Delta\phi = 0$ (OFF) and π (ON), respectively. By measuring them one can simply determine the remaining switch parameters

$$s = 2\,T_{\mathrm{CROSS,min}} \text{ and} \tag{14}$$

$$\sin^2\left(\frac{r\pi}{2}\right) = \frac{T_{\mathrm{CROSS,max}} - T_{\mathrm{CROSS,min}}}{1-2T_{\mathrm{CROSS,min}}}\ . \tag{15}$$

Equal ER exima (±17 dB) indicate that $T_{\mathrm{CROSS,max}} \approx 1-T_{\mathrm{CROSS,min}}$, DC length is close to optimum ($r \approx 1$) and $s \approx 0.04$ dominates the maximum ER. The relatively high s is probably due to scattering, and it could be lowered by reducing the excess loss of the switch, which was measured to be ~1 dB with respect to an equally long straight waveguide. It should be noted that the maximum output ER of ±17 dB describes perfect phase control, and that in the following results the emphasis is in the phase modulation depth. For any measured T_{CROSS} with an arbitrary $\Delta\phi$, one can calculate the ideal transmission $T_{\mathrm{CROSS,ideal}}$ corresponding to an ideal MZI structure ($r = 1$, $s = 0$) from

$$T_{\mathrm{CROSS,ideal}} = \frac{T_{\mathrm{CROSS}} - T_{\mathrm{CROSS,min}}}{T_{\mathrm{CROSS,max}} - T_{\mathrm{CROSS,min}}}\ . \tag{16}$$

This value, or the corresponding ideal extinction ratio

$$\mathrm{ER}_{\mathrm{ideal}} = \left| 10\log\left(\frac{T_{\mathrm{CROSS,ideal}}}{1-T_{\mathrm{CROSS,ideal}}}\right)\right| \mathrm{dB}\ , \tag{17}$$

should be used to evaluate the depth of the thermo-optic phase modulation.

After the preliminary characterisation the best switches were characterised with fast externally applied control signals. First, simple step-wise modulation (ON/OFF) was applied to one heater only. The maximum modulation frequency for 15 dB ER ($\mathrm{ER}_{\mathrm{ideal}}$ = 20 dB) was 10 kHz. The measured CROSS-port transmission at 10 kHz operation is shown in Fig. 39. The measured speed and power consumption of the switch were somewhat higher than in simulations. The heat conductivity from the Si substrate to the heat sink was probably higher than in simulations.

The feasibility of the novel modulation method (see Chapter 2.5) was tested by using it to accelerate the TO switch. At first, a simple, inexpensive, and somewhat slow control electronics was built with a minimum time-step of 1 μs. This defined a maximum frequency of 167 kHz for the new modulation method. The rise and fall operations were then shortened by optimising the heating powers P_1 and P_2 of the two waveguide branches in 1 μs time-steps. The switching state could then be changed in 3 μs with 15 dB ER. This could be done either once or with a continuous 167 kHz frequency. With better electronics, higher frequencies could have been obtained with lower ER.

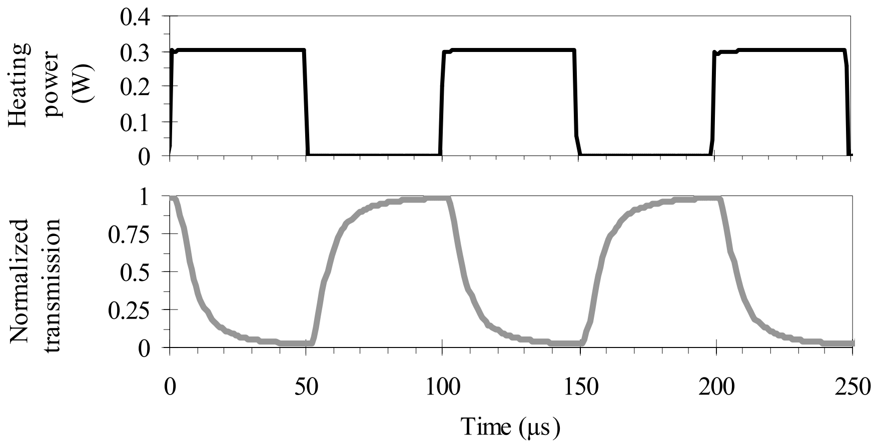

Figure 39. Measured CROSS-port transmission (lower graph) of the TO Si waveguide switch with traditional 10 kHz modulation (upper graph). Transmission is normalised to the attainable range of the slightly non-ideal switch (1–99%).

Sensitivity to random modulation was tested by sending semi-random bit sequences as inputs to the control electronics. This dropped the measured ER to 13 dB (ER_{ideal} = 15 dB). Optical response to a semi-random input signal at 167 kHz is shown in Fig. 40. With a random input signal the average power consumption was 150 mW for the traditional 10 kHz modulation and 590 mW for the novel 167 kHz modulation, i.e. the speed and the power consumption increased by factors 17 and 3.9, respectively. Thus, the acceleration was efficient with respect to the increase in heating power.

In order to reach even faster operation, new control electronics was constructed and used to optimise single switch transitions with 9 dB ER (10–90%) [V]. Single rise and fall times were successfully suppressed to 725 and 700 ns, respectively. For comparison, a traditional modulation method provided 29 and 35 μs transition times, i.e. 40–50 times slower operation. If the single transitions are carried out with an average frequency of 1 or 10 kHz, the power consumption increases 4 and 44%, respectively, when compared to traditional modulation with the same OFF-state bias power. Thus, the acceleration was again efficient with respect to the increase in heating power.

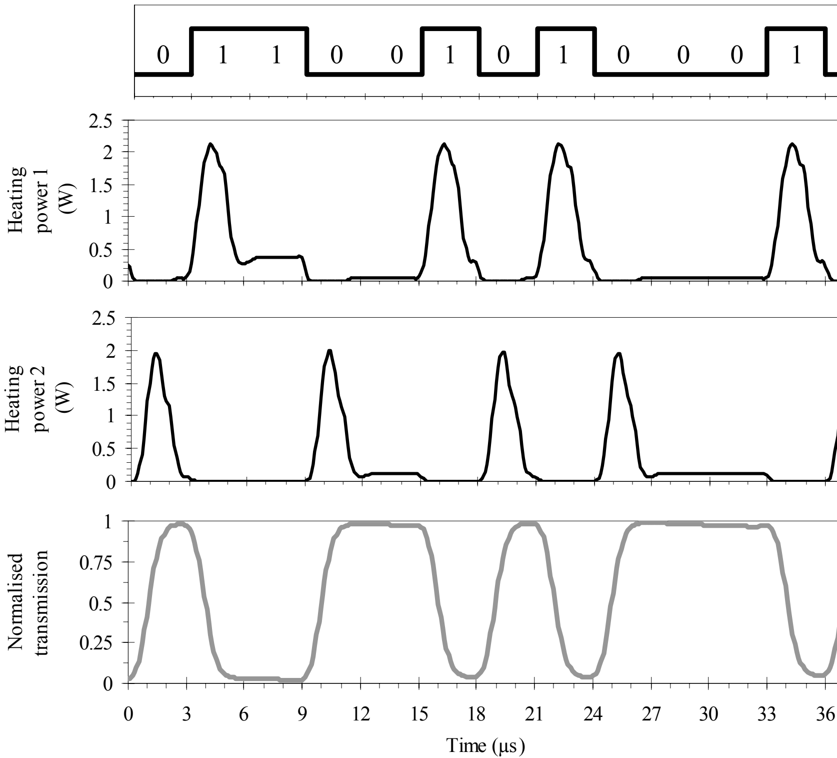

Figure 40. Semirandom input data at 167 kHz frequency (top), optimised heating powers P_1 and P_2 (middle), and the measured T_{CROSS} (bottom). Transmission is normalised to the attainable range (1–99%) of the slightly non-ideal TO Si waveguide switch.

Based on the results, TO switching appears to be approximately tenfold faster (~10 kHz for $H \approx 10$ μm) in Si waveguides than in equally large low index contrast waveguides, such as silica or polymer waveguides [18]. This is due to the good thermal conductivity of Si and the thin BOX and cladding layers. Thermal insulation grooves [88] and an appropriate BOX layer thickness can be used to obtain a desired compromise between speed and power consumption. Furthermore, smaller waveguides can provide both faster operation and lower consumption at the cost of more complicated fiber coupling. The feasibility of the new modulation method was successfully demonstrated with a speed improvement by a factor of 17–50 with respect to traditional modulation. For TO switches operating at $\lambda \approx 1550$ nm and having good mode matching with SM fibers, the obtained 167 kHz frequency and sub-μs switching times are clearly the fastest results reported so far in literature. In particular, one should keep in mind that these results are obtained with high ER values of 13–20 dB. For 3 dB modulation, the maximum frequencies would be much higher than those reported above. The promising results indicate that the new modulation principle should be tested also with other interferometric devices, such as slower silica and polymer switches, and 1×1 MZI modulators.

5. Conclusions

In this work, theoretical, numerical and experimental studies were carried out in order to promote Si waveguide technology. Based on the theoretical and numerical studies, a new SM condition and the use of multi-step patterning for Si waveguides were proposed. Novel methods were also invented for accelerating interferometric devices and for measuring the polarisation axes of waveguides and PM fibers. A small contribution was also given for the development of a new simulation method for corrugated waveguide gratings.

Numerous waveguides and waveguide components were fabricated by using standard and modified clean-room processes. Existing processes were improved, especially for realising low-loss Si rib waveguides. New processes were developed for multi-step patterning, as well as for patterning ~1 µm deep corrugated gratings and photonic crystal waveguides with a combination of e-beam lithography and two types of dry etching. Post-processing steps were also developed, especially waveguide facet polishing, anti-reflection coating, and fiber pigtailing.

For the characterisation of fabricated devices, new setups and methods were developed. Propagation losses as low as 0.13±0.01 dB/cm were accurately measured for 9 µm thick Si rib waveguides by using a 114 cm long spiral waveguide. This is the lowest propagation loss reported so far for SM dry etched Si waveguides at $\lambda \approx 1550$ nm. Modal mismatch between SM fibers and 9 µm thick Si rib waveguides was measured to be 0.6 dB, while thicker Si waveguides are expected to have mismatch losses as small as ~0.1 dB. The reflection losses at Si waveguide end facets were suppressed from 0.7–1.6 dB/facet to <0.15 dB/facet by using a Ta_2O_5 AR coating. Losses due to misalignments in fixed fiber pigtail arrays were kept below 0.5 dB/facet with 1.5 µm alignment accuracy. This included the impact of passive alignment into V-grooves and active alignment between fiber and waveguide arrays. Waveguides were pigtailed also with PM fibers. This involved the accurate rotational alignment between fibers and waveguides. For this purpose, also the invented new rotational alignment method was tested, and its accuracy was found to be better than 0.2°. At least for some applications, the new method appears to be more simple and accurate than the alternative methods. Waveguide birefringence was found to vary between 0.0001 and 0.00063 depending on the cladding material. This enables the fabrication of both polarisation independent and maintaining Si waveguides. However, the polarisation extinction ratio of waveguides and directional couplers was found to be only ~15 dB. This should be improved by further reducing the propagation losses.

Finally, the fabricated thermo-optical switches with non-optimised directional couplers were modulated with a traditional step-wise method and the invented novel modulation method. The former provided a maximum frequency of 10 kHz with 15 dB extinction

ratio and an average power consumption of 150 mW. The new method provided a maximum frequency of 167 kHz with the same ER and an average power consumption of 590 mW. Therefore, the frequency and the power consumption were increased by factors 17 and 3.9, respectively. It should be noted, that the measured 15 dB ER corresponds to a 20 dB ER in an ideal switch structure. With improved control electronics and a slightly lower ER of 9 dB, single rise and fall times were suppressed down to 725 and 700 ns, respectively. The continuous 167 kHz modulation frequency and the single transition times of ~0.7 μs represent the fastest values reported so far for thermo-optic waveguide switches operating at $\lambda \approx 1550$ nm and having efficient fiber coupling (thickness >5 μm).

Considering all the possibilities for extreme photonic circuit miniaturisation and monolithic integration with e.g. electrical and micromechanical functions, silicon microphotonics is a fascinating research area with a lot of potential for scientific and commercial success. However, silicon microphotonics, and Si waveguide technology in particular, are also a very challenging subject. Some of the main difficulties are the high capital cost of fabrication tools, sensitivity to surface roughness, polarisation dependence, difficulties in vertical tapering, and the requirement for 1 μm alignment accuracy in hybrid assembly. Also, the present lack of sufficient computer power for accurate 3D simulations in macroscopic scale complicates the design and theoretical analysis of Si waveguide devices. Furthermore, the indirect bandgap and negligible electro-optic constant of Si have so far prevented the realisation of optical light sources and fast modulators that would be competitive with other photonic technologies, such as compound semiconductors and lithium niobate. These drawbacks have prevented at least the silicon waveguides from making a true commercial success, although low index contrast waveguides on Si have already become widely used in optical communication.

The advantages of Si waveguides are estimated to appear especially in the mass production of photonic devices with high quality and sufficient complexity, as well as in the future integration between various optical, electronic and mechanical functions on a single chip. In the present optical communication market the demand for such devices is quite low. However, it is estimated that the further development of silicon microphotonics and the revival of the market can change the situation both radically and rapidly. During the past few years this technology has already evolved with huge steps. At the same time, numerous companies, universities and research organisations have started to study Si waveguide technology, which shows that there is a common belief in it.

Hopefully, this thesis will contribute to the future success of silicon microphotonics. In a wider perspective, the potential success of silicon microphotonics can provide a new technological development step for the whole *Silicon Age*.

References

1. http://www.intel.com/technology/itj/2002/volume06issue02/art02_processdev/vol6iss2_art02.pdf

2. http://www.intel.com/technology/itj/2004/volume08issue02/art05_on-chip/p02_intro.htm

3. G. E. Moore, "Cramming more components onto integrated circuits", *Electronics* **38**, pp. 114–117, 1965.

4. L. Pavesi, D.J. Lockwood (Eds.), *Silicon Photonics*, Topics in Applied Physics, **94**, Springer, 2004. 397 p. ISBN 3-540-21022-9.

5. International Technology Roadmap for Semiconductors: 2003 Edition (ITRS 2003), http://public.itrs.net

6. M. Paniccia, M. Morse, and M. Salib, "Integrated photonics", in [4], pp. 51–88, 2004.

7. M. Hoffmann and E. Voges, "Bulk silicon micromachining for MEMS in optical communication systems", *J. Micromech. Microeng.* **12**, pp. 349–360, 2002.

8. J. Kiihamäki, J. Dekker, P. Pekko, H. Kattelus, T. Sillanpää, and T. Mattila, "Plug-up – a new concept for fabricating SOI MEMS devices, *Microsystems Technologies* **10**, pp. 346–350, 2004.

9. S. Roy, R. G. DeAnna, C. A. Zorman, and M. M. Mehregany, "Fabrication and characterization of polycrystalline SiC resonators", *IEEE Electron Device Lett.* **49**, pp. 4323–4332, 2002.

10. A. Torkkeli, *Droplet microfluidics on a planar surface*, PhD Thesis, VTT Publications 504, Espoo, Finland, 194 p. + app. 19 p., 2003. ISBN 951-38-6237-2; 951-38-6238-0. http://www.vtt.fi/inf/pdf/publications/2003/P504.pdf

11. M. Ylimaula, M. Åberg, J. Kiihamäki, and H. Ronkainen, "Monolithic capacitive pressure sensor with CMOS readout circuit", *Proc. 29th European Solid-State Circuits Conf.* (ESSCIRC 2003), pp. 611–614, 2003.

12. N. Maluf, *An introduction to microelectromechanical systems engineering*, Artech House, 2000. 265 p. ISBN 0-89006-581-0.

13. Z. Gaburro, "Optical interconnect", in [4], pp. 121–176, 2004.

14. J. Wieland, H. Duran, and A. Felder, "Two-channel 5 Gbit/s silicon bipolar monolithic receiver for parallel optical interconnects", *Electron. Lett.* **30**, pp. 359–359, 1994.

15. P. Friis, K. Hoppe, O. Leistiko, K. B. Mogensen, J. Hübner, and J. P. Kutter, "Monolithic integration of microfluidic channels and optical waveguides in silica on silicon", *Appl. Opt.* **40**, pp. 6246–6251, 2001.

16. S. Franssila, *Introduction to microfabrication*, John Wiley & Sons, 2004. 401 p. ISBN 0-470-85105-8.

17. J. D. Plummer, M. D. Deal, and P. B. Griffin, *Silicon VLSI Technology: Fundamentals, Practice, and Modeling*, Prentice Hall, 2000, 817 p. ISBN: 0130850373.

18. E. J. Murphy (Ed.), *Integrated optical circuits and components*, Marcel Dekker, Inc, 1999, 449 p. ISBN: 0-8247-7577-5.

19. A. Splett, J. Schmidtchen, B. Schüppert, and K. Petermann, "Low loss optical ridge waveguides in a strained GeSi epitaxial layer grown on silicon", *Electron. Lett.* **26**, pp. 1035–1037, 1990.

20. G. Cocorullo, F. G. Della Corte, M. Iodice, I. Rendina, and P. M. Sarro, "Silicon-on-insulator rib waveguides with a high-confining ion-implanted lower cladding", *IEEE J. Sel. Top. Quantum Electron.* **4**, pp. 983–989 1998.

21. G. Bonfrate, M. Harlow, C. Ford, G. Maxwell, and P. D. Townsend, "Asymmetric Mach–Zehnder germanosilicate channel waveguide interferometers for quantum cryptography systems", *Electron. Lett.* **37**, pp. 846–867, 2001.

22. S. Janz, "Silicon-based waveguide technology for wavelength dicision multiplexing ", in [4], pp. 323–360, 2004.

23. P. Katila, T. Aalto, P. Heimala, and M. Leppihalme, "Optical waveguides for 1064 nm and chip pigtailing with PM fibers", *Proc. 4th Int. Conf. on Space Optics* (ICSO 2000), Toulouse, France, 5–7 December 2000, pp. 635–640, 2000.

24. G. D. Maxwell and B. J. Ainslie, "Demonstration of a directly written directional coupler using UV-induced photosensitivity in a planar silica waveguide", *Electron. Lett.* **31**, pp. 95–96, 1995.

25. K. Wörhoff, P. V. Lambeck, and A. Driessen, "Design, tolerance analysis, and fabrication of silicon oxynitride based planar optical waveguides for communication devices", *J. Lightwave Technol.* **17**, pp. 1401–1407, 1999.

26. P. Heimala, P. Katila, J. Aarnio, and A. Heinämäki, "Thermally tunable integrated optical ring resonator with poly-si thermistor", *J. Lightwave Technol.* **14**, pp. 2260–2267, 1996.

27. K. K. Lee, D. R. Lim, A. Agarwal, K. Wada, and L. C. Kimerling, "Scattering losses in a high Δn waveguide system for silicon microphotonics", *Mat. Res. Soc. Symp. Proc.* **637**, paper E3.4, 2001.

28. M. Leppihalme, T. Aalto, P. Katila, P. Heimala, M. Blomberg, and S. Tammela, "Si-based integrated optical and photonic microstructures", *Proc. SPIE* **3936**, pp. 2–15, 2000.

29. M. A. Green, J. Zhao, A. Wang, P. J. Reece, and M. Gal, "Efficient silicon light-emitting diodes", *Nature* **412**, pp. 805–808, 2001.

30. L. Pavesi, L. Dal Negro, C. Mazzoleni, G. Franzò, and F. Priolo, "Optical gain in silicon nanocrystals", *Nature* **408**, pp. 440–444, 2000.

31. L. Khriachtchev and M. Räsänen, "Optical gain in Si/SiO_2 lattice: Experimental evidence with nanosecond pulses", *Appl. Phys. Lett.* **79**, pp. 1249–1251, 2001.

32. ST Microelectronics (http://www.stmicroelectronics.com), Press release 29 October 2002.

33. S. Coffa, G. Franzò, and F. Priolo, "High efficiency and fast modulation of Er-doped light emitting Si diodes", *Appl. Phys. Lett.* **69**, pp. 2077–2072, 1996.

34. Y. C. Yan, A. J. Faber, and H. de Waal, "Erbium-doped phosphate glass waveguide on silicon with 4.1 dB/cm gain at 1.535 μm", *Appl. Phys. Lett.* **71**, pp. 2922–2924, 1997.

35. H.-S. Han, S.-Y. Seo, and J. H. Shin, "Coefficient determination related to optical gain in erbium-doped silicon-rich oxide waveguide amplifier", *Appl. Phys. Lett.* **81**, pp. 3720–3722, 2002.

36. F. Iacona, D. Pacifici, A. Irrera, M. Miritello, G. Franzò, F. Priolo, D. Sanfilippo, G. D. Stefano, and P. G. Fallica, "Electroluminescence at 1.54 μm in Er-doped Si nanocluster-based devices", *Appl. Phys. Lett.* **81**, pp. 3242–3244, 2002.

37. L. Diehl, S. Menteşe, E. Müller, D. Grützmacher, H. Sigg, U. Gennser, I. Sagnes, Y. Campidelli, O. Kermarrec, and D. Bensahel, "Electroluminescence from strain-compensated $Si_{0.2}Ge_{0.8}$/Si quantum-cascade structures based on bound-to-continuum transition", *Appl. Phys. Lett.* **81**, pp. 4700–4702, 2002.

38. R. Claps, D. Dimitropoulos, and B. Jalali, "Stimulated Raman scattering in silicon waveguides", *Electron. Lett.* **38**, pp. 1352–1354, 2002.

39. R. Claps, D. Dimitropoulos, Y. Han, and B. Jalali, "Observation of Raman emission in silicon waveguides at 1.54 μm", *Optics Exp.* **10**, pp. 1305–1313, 2002.

40. B. Jalali, R. Claps, D. Dimitropoulos, and V. Raghunathan, "Light generation, amplification and wavelength conversion via stimulated Raman scattering in silicon microstructures", in [4], pp. 199–238, 2004.

41. R. J. Curry, W. P. Gillin, A. P. Knighs, and R. Gwillam, "Silicon-based organic light-emitting diode operating at a wavelength of 1.5 µm" *Appl. Phys. Lett.* **77**, pp. 2271–2273, 2000.

42. D. L. Mathine, H. S. Woo, W. He, T. W. Kim, B. Kippelen, and N. Peyghambarian, "Heterogeneously integrated organic light-emitting diodes with complementary metal-oxide-silicon circuitry", *Appl. Phys. Lett.* **76**, pp. 3849–3851, 2000.

43. L. Dal Negro, M. Cazzanelli, N. Daldosso, Z. Gaburro, L. Pavesi, F. Priolo, D. Pacifici, G. Franzo, and F. Iacona, "Stimulated emission in plasma-enhanced chemical vapour deposited silicon nanocrystals", *Physica E* **16**, pp. 297–308, 2003.

44. L. Pavesi, "Will silicon be the photonic material of the third millenium?", *J. Phys. Condens. Matter* **15**, pp. 1169–1196, 2003.

45. R. Claps, V. Raghunathan, D. Dimitropoulos, and B. Jalali, "Anti-stokes Raman conversion in silicon waveguides", *Optics Exp.* **11**, pp. 2862–2872, 2003.

46. S. Kimura, K. Maio, T. Doi, T. Shimano, and T. Maeda, "Photodetectors monolithically integrated on SOI substrate for optical pickup using blue or near-infrared semiconductor laser", *IEEE Trans. Electron Dev.* **49**, pp. 997–1004, 2002.

47. D. M. Kuchta and H. A. Ainspan, "Performance of fiber optic data links using 670 nm CW VCSEL's and a monolithic Si photodetector and CMOS preamplifier", *IBM J. Res. & Development.* **39**, pp. 63–72, 1995.

48. H. Zimmermann, K. Kieschnick, M. Heise, and H. Pless, "BiCMOS OEIC for optical storage systems", *Electron. Lett.* **34**, pp. 1875–1876, 1998.

49. Schaub, J. D., Li, R., Csutak, S. M. and Campbell, J. C., "High-speed monolithic photoreceivers on high resistivity and SOI substrates", *IEEE J. Lightwave Technol.* **19**, pp. 272–278, 2001.

50. H. Zimmermann, "Silicon photo-receivers", in [4], pp. 239–268, 2004.

51. J. Ho and K. S. Wong, "High-speed and high-sensitivity silicon-on-insulator metal-semiconductor-metal photodetector with trench structure", *Appl. Phys. Lett.* **69**, pp. 16–18, 1996.

52. S. Fama, L. Colace, G. Masini, G. Assanto, and H.-C. Luan, "High performance germanium-on-silicon detectors for optical communications", *Appl. Phys. Lett.* **81**, pp. 586–588, 2002.

53. G. Masini, L. Colace, G. Assanto, H.-C. Luan, and L. C. Kimerling, "High-performance p-i-n Ge on Si photodetectors for the near-infrared: From model to demonstration", *IEEE Trans. Electron Dev.* **48**, pp. 1092–1096, 2001.

54. L. Colace, G. Masini, G. Assanto, H.-C. Luan, K. Wada, and L. C. Kimerling, "Efficient high-speed near-infrared Ge photodetectors integrated on Si substrates", *Appl. Phys. Lett.* **76**, pp. 1231–1233, 2000.

55. H. Lafontaine, N. L. Rowell, S. Janz, and D.-X. Xu, "Growth of undulating $Si_{0.5}Ge_{0.5}$ layers for photodetectors at λ=1.55 µm", *J. Appl. Phys.* **86**, pp. 1287–1291, 1999.

56. F. Y. Huang, X. Zhu, M. O. Tanner, and K. L. Wang, "Normal-incidence strained-layer superlattice $Ge_{0.5}Si_{0.5}$/Si photodiodes near 1.3 µm", *Appl. Phys. Lett.* **67**, pp. 566–568, 1995.

57. A. Splett, T. Zinke, K. Petermann, E. Kasper, H. Kibbel, H.-J. Herzog, and H. Presting, "Integration of waveguides and photodetectors in SiGe for 1.3 µm operation", *IEEE Photon. Technol. Lett.* **6**, pp. 59–61, 1994.

58. S. Winnerl, D. Buca, S. Lenk, Ch. Buchal, S. Mantl, and D.-X. Xu, "MBE grown Si/SiGe undulating layer superlattices for infrared light detection", *Mat. Sci. Eng. B* **89**, pp. 73–76, 2002.

59. M. El kurdi, P. Boucaud, S. Sauvage, G. Fishman, O. Kermarrec, Y. Campidelli, D. Bensahel, G. Saint-Girons, I. Sagnes, and G. Patriarche, "Silicon-on-insulator waveguide detector with Ge/Si self-assembled islands", *J. Appl. Phys.* **92**, pp. 1858–1861, 2002.

60. M. El kurdi, P. Boucaud, S. Sauvage, O. Kermarrec, Y. Campidelli, D. Bensahel, G. Saint-Girons, and I. Sagnes, "Near-infrared photodetector with Ge/Si self-assembled quantum dots" , *Appl. Phys. Lett.* **80**, pp. 509–511, 2002.

61. P. G. Kik, A. Polman, S. Libertino, and S. Coffa, "Design and performance of an erbium-doped silicon waveguide detector operating at 1.5 µm", *J. Lightwave Technol.* **20**, pp. 862–867, 2002.

62. T. Aalto, S. Yliniemi, P. Heimala, P. Pekko, J. Simonen, and M. Kuittinen, "Integrated Bragg gratings in silicon-on-insulator waveguides ", *Proc. SPIE* **4640**, pp. 117–124, 2002.

63. T. Aalto, P. Heimala, S. Yliniemi, M. Kapulainen, and M. Leppihalme, "Fabrication and characterization of waveguide structures on SOI", *Proc. SPIE* **4944**, pp. 183–194, 2003.

64. T. Aalto / Valtion Teknillinen Tutkimuskeskus, "Optical waveguide for integrated optical circuit and method for producing the optical waveguide", PCT Patent Application WO 03/085429 A1, Priority date 11 April 2002, Publication date 16 October 2003.

65. T. Aalto / Valtion Teknillinen Tutkimuskeskus, "Optical waveguide ", PCT Patent Application WO 03/085430 A1, Priority date 11 April 2002, Publication date 16 October 2003.

66. T. Aalto, M. Kapulainen, M. Harjanne, and M. Rönö / Valtion Teknillinen Tutkimuskeskus, "Method for controlling an optoelectronic component", PCT Patent Application WO 2004/023196 A1, Priority date 4 September 2002, Publication date 18 March 2004.

67. T. Aalto / Valtion Teknillinen Tutkimuskeskus, "Method and device for determining the rotational angle of the polarisation axis of an optical waveguide or fiber", PCT Patent Application WO 2004/065921 A1, Priority date 24 January 2003, Publication date 5 August 2004.

68. T. Aalto / Valtion Teknillinen Tutkimuskeskus, PCT Application PCT/FI2004/000299, Priority date 18 May 2004, to be published 18 November 2005.

69. B. Jalali, S. Yegnanarayana, T. Yoon, T. Yoshimoto, I. Rendina, and F. Coppinger, "Advances in silicon-on-insulator optoelectronics", *IEEE J. Sel. Top. Quantum Electron.* **4**, pp. 938–947, 1998.

70. S. Yliniemi, T. Aalto, P. Heimala, P. Pekko, K. Jefimovs, J. Simonen, and T. Uusitupa, "Fabrication of photonic crystal waveguide elements on SOI", *Proc. SPIE* **4944**, pp. 23–31, 2003.

71. B. Jalali, "Silicon-on-insulator photonic integrated circuit (SOI-PIC) technology", *Proc. SPIE* **2997**, pp. 60–71, 1997.

72. A. G. Rickman, G. T. Reed, "Silicon-on-insulator optical rib waveguides: loss, mode characteristics, bends and Y-junctions", *IEE Proc.-Optoelectron.* **141**, pp. 391–393, 1994.

73. W. P. Maszara, R. Dockerty, C. F. H. Gondran, P. K. Vasudev, "SOI materials for mainstream CMOS technology", *Electrochem. Soc. Proc.*, Ed. S. Christoloveanu, **97**, pp. 15–26, 1997.

74. SOITEC, manufacturer of Smart-Cut SOI wafers, http://www.soitec.com

75. Canon, commercial manufacturer of ELTRAN SOI wafers, http://www.canon.com/technology/detail/device/soi/index.html

76. E. D. Palik, *Handbook of optical Constants of Solids*, Academic Press Inc., 1985.

77. W. Bogaerts, *Nanophotonic waveguides and photonic crystals in silicon-on-insulator*, PhD Thesis, Universiteit Gent, 2004. 271 p.

78. A. Sakai, T. Fukazawa, T. Baba, "Low loss ultra-small branches in a silicon photonic wire waveguide", *IEICE Trans. Electron.* **E85-C**, pp.1033–1038, 2002.

79. K. K. Lee, D. R. Lim, and L. C. Kimerling, "Fabrication of ultralow-loss Si/SiO_2 waveguides by roughness reduction", *Opt. Lett.* **26**, pp. 1888–1890, 2001.

80. Y. A. Vlasov and S. J. McNab, "Losses in single-mode silicon-on-insulator strip waveguides and bends", *Optics Exp.* **12**, pp. 1622–1631, 2004.

81. M. Harjanne, *Design of tight bends in optical waveguides*, Master's Thesis, Helsinki University of Technology, 2003. 58 p. In Finnish.

82. R. A. Soref, J. Schmidtchen, K. Petermann, "Large single-mode rib waveguides in GeSi-Si and Si-on-SiO_2", *IEEE J. Quantum Electron.* **27**, pp. 1971–1974, 1991.

83. K. Hosomi, T. Katsuyama, "A dispersion compensator using coupled defects in a photonic crystal", *IEEE J. Quantum Electron.* **38**, pp. 825–829, 2002.

84. S. Yliniemi, J. Simonen, T. Aalto, P. Heimala, "Fabrication of silicon nanostructures for photonic crystal applications", *Proc. 4th Int. Conf. on Materials for Mikroelectronics and Nanoengineering*, Espoo, Finland, 10–12 June 2002. IOM Communications Ltd, 2002. ISBN 1-86125-155-6.

85. T. W. Ang, G. T. Reed, A. Vonsovici, A. G. R. Evans, P. R. Routley, M. R. Josey, "0.15 dB/cm loss in Unibond SOI waveguides", *Electron. Lett.* **35**, pp. 977–978, 1999.

86. Fischer U., Zinke T., Kropp J.-R., Arndt F., Petermann K., "0.1 dB/cm waveguide losses in single-mode SOI rib waveguides", *IEEE Photonics Technol. Lett.* **8**, pp. 647–648, 1996.

87. T. Zinke, U. Fischer, B. Schüppert, K. Peterman, "Theoretical and experimental investigation of optical couplers in SOI", *Proc. SPIE* **3007**, pp. 30–39, 1997.

88. S. A. Clark, B. Culshaw, E. J. C. Dawnay, and I. E. Day, "Thermo-optic phase modulators in SIMOX material", *Proc. SPIE* **3936**, pp. 16–24, 2000.

89. P. Dainesi, A. Küng, M. Chabloz, A. Lagos, Ph. Flückiger, A. Ionescu, P. Fazan, M. Declerq, Ph. Renaud, Ph. Robert, "CMOS compatible fully integrated Mach–Zehnder interferometer in SOI technology", *IEEE Photon. Technol. Lett.* **12**, pp. 660–662, 2000.

90. T. Bestwick, "ASOC™ – A silicon-based integrated optical manufacturing technology", *Proc.48th IEEE Electronic Components and Technology Conf.*, 25–28 May 1998, pp. 566–571, 1998.

91. A. Cutolo, M. Iodice, A. Irace, P. Spirito, L. Zeni, "An electrically controlled Bragg reflector integrated in a rib silicon on insulator waveguide", *Appl. Phys. Lett.* **71**, pp. 199–201, 1997.

92. J. Tidmarsh, S. Fasham, P. Stopford, A. Tomlinson, and T. Bestwick," A narrow linewidth laser for WDM applications using silicon waveguide technology", *Proc. Lasers and Electro-Optics Society 12th Annual Meeting (LEOS '99)*, 8–11 Nov. 1999, IEEE, Vol. 2, pp. 497–498, 1999.

93. R. J. Bozeat, S. Day, F. Hopper, F. P. Payne, S. W. Roberts, and M. Asghari, "Silicon based waveguides ", in [4], pp. 267–294, 2004.

94. P. D. Trinh, S. Yegnanarayanan, F. Coppinger, B. Jalali, "Silicon-on-insulator (SOI) phased-array wavelength multi/demultipelexer with extremely low-polarization sensitivity", *IEEE Photon. Technol. Lett.* **9**, pp. 940–942, 1997.

95. W. N. Ye, D.-X. Xu, S. Janz, P. Cheben, A. Delâge, M.-J. Picard, B. Lamontagne, and N. G. Tarr, "Stress-induced birefringence in silicon-on-insulator (SOI) waveguides", *Proc. SPIE* **5357**, pp. 57–66, 2004.

96. R. A. Soref, B. R. Bennett, "Electrooptical effects in silicon", *IEEE J. Quantum Electron.* **23**, pp. 123–129, 1987

97. A. Liu, R. Jones, L. Liao, D. Samara-Rubio, D. Rubin, O. Cohen, R. Nicolaescu, and M. Panicia, "A high-speed silicon optical modulator based on a metal-oxide-semiconductor capacitor", *Nature* **427**, pp. 615–618, 2004.

98. G. Cocorullo, M. Iodice, I. Rendina, and M. Sarro, "Silicon thermooptical micromodulator with 700-kHz, 3-dB bandwidth", *IEEE Photon. Technol. Lett.* **7**, pp. 363–365, 1995.

99. U. Fischer, T. Zinke, B. Schüppert, and K. Petermann, "Singlemode optical switches based on SOI with large cross-section" *Electron. Lett.* **30** , pp. 406–408, 1994.

100. G. V. Treyz, "Silicon Mach–Zehnder waveguide interferometers operating at 1.3 μm", *Electron. Lett.* **27**, pp. 118–120, 1991.

101. N. A. Nazarova, G. I. Romanova, A. D. Yas'kov, "Refractometric characteristics of silicon", *Sov. J. Opt. Technol.* **55**, pp. 220–224, 1988.

102. B. E. A. Saleh and M. C. Teich, *Fundamentals of photonics*, John Wiley & Sons, Inc, 1991. 966 p. ISBN 0-471-83965-5.

103. H. Nishihara, M. Haruna, and T. Suhara, *Optical Integrated Circuits*, McGraw–Hill, New York, 1989, 374 p. ISBN: 0-07-046092-2.

104. P. Tien, "Light waves in thin films and integrated optics", *Appl. Opt.* **10**, pp. 2395–2413, 1971.

105. A. W. Snyder and J. D. Love, *Optical waveguide theory*, Chapman and Hall Ltd., 1983. 734 p. ISBN 0-412-24250 8.

106. C2V, present representative of the Slab, TempSelene, and Prometheus software used for optical simulation, http://www.c2v.nl/

107. P. Kaiser, E. A. J. Marcatili, and S. E. Miller, "A new optical fiber", *The Bell System Technical Journal* **52**, pp. 265–269, 1973.

108. J. A. Arnaud, "Transverse coupling in fiber optics Part II: Coupling to mode sinks", *The Bell System Technical Journal* **53**, pp. 675–696, 1974.

109. E. A. J. Marcatili, "Slab-coupled waveguides", *The Bell System Technical Journal* **53**, pp. 645–674, 1974

110. M. Saruwatari, K. Nawate, "Semiconductor laser to single mode fiber coupler", *Appl. Optics* **18**, pp 1847–1856, 1979.

111. M. K. Smitt, E. C. M. Pennings, and H. Block, "A normalized approach to the design of low-loss optical waveguide bends", *IEEE J. Lightwave Technol.* **11**, pp. 1737–1742, 1993.

112. Y. Z. Tang, W. H. Wang, T. Li, and Y. L. Wang, "Integrated waveguide turning mirror in silicon-on-insulator", *IEEE Photon. Technol. Lett.* **14**, pp. 68–70, 2002.

113. L. B. Soldano, E. C. M. Pennings, "Optical multi-mode interference devices based on self imaging: Principles and applications", *J. Lightwave Technol.* **13**, pp. 615–626, 1995.

114. M. J. Brinkman, W. K. Bischel, T. Kowalczyk, D. R. Main, and L. L. Huang / Gemfire Corporation, "Thermo-optical switch having fast rise-time", Patent US 6,351,578 B1, Priority date 6 August 1999.

115. B. Mersali, A. Ramdane, A. Carenco, "Optical-mode transformer: A III–V circuit integration enabler", *IEEE J. Sel. Top. Quantum Electron.* **3**, pp. 1321–1330, 1997.

116. A. G. Rickman, A. P. R. Harpin, and R. J. R. Morris / Bookham Technology Ltd., "A tapered rib waveguide", PCT Patent Application WO 98/35250, Priority date 7 February 1997, Publication date 13 August 1998.

117. M. Popovic, K. Wada, S. Akiyama, H. Haus, and J. Michel, "Air trenches for sharp silica waveguide bends", *IEEE J. Lightwave Technol.* **20**, pp. 1762–1772, 2002.

118. N. Caponio and C. Svelto, "A simple angular alignment technique for a polarization-maintaining-fibre", *IEEE Photonics Technol. Lett.* **6**, pp. 728–729, 1994.

119. A. Ebberg and R. Noe, "Novel high precision alignment technique for polarization maintaining fibres using a frequency modulated tunable laser", *Electron. Lett.* **26**, pp. 2009–2010, 1990.

120. Y. Ida, K. Hayashi, M. Jinno, T. Horii, and K. Arai, "New method for polarization alignment of birefringent fibre with laser diode", *Electron. Lett.* **21**, pp. 18–21, 1985.

121. G. R. Walker and N. G. Walker, "Alignment of polarization maintaining fibres by temperature modulation", *Electron. Lett.* **23**, pp. 689–691, 1987.

122. Y. Namihira, J. Maeda, “Comparison of various polarisation mode dispersion measurement methods in optical fibres”, *Electron. Lett.* **28**, pp. 2265–2266, 1992.

Appendix A: Simulation tools

In this work, the following simulation tools were mostly used:

- *PDE Toolbox for Matlab 5* (from Comsol)
  - Calculation of static and dynamic temperature distributions in waveguide cross-sections by solving partial differential equations with a finite element method.
  - Results used in publications III–IV and Chapter 2.5.
  - Software used as a platform for developing FEMLAB (no longer available)
- *Optonex Integrated optics design software* (from Optonex)
  - Sub-components *LightGuide*, *FieldEx* and *BPM* were used for 2D BPM simulations of bends and directional couplers
  - Sub-components *Channel* and *Contours* were used for calculating 2D modes in waveguides and DCs, mode mismatch with SM fibers, and coupling coefficients of DCs.
  - Results used in publication III and Chapter 2.5.
- *Slab* (from Kymata Software), version 4.3.04 for Windows NT 4.0[1]
  - Calculation of 1D waveguide modes. Fast and accurate.
  - Results used in publication I and Chapter 2.5.
- *TempSelene* (from Kymata Software), version 4.3.04 for Windows NT 4.0[1]
  - Calculation of 2D waveguide modes and coupling efficiencies between calculated fields (including modal mismatch between fibers and waveguides).
  - Finite-difference (*FD*) algorithms used for simple problems and first estimations.
  - *Bend* algorithm used for rigorous calculations (for SM condition and bend loss): Full-vectorial and complex solver can solve bend modes and leaky modes with losses.
  - Typical calculation grid spacing 50–200 nm in both horizontal and vertical direction
  - For example, 10 µm thick rib waveguides were typically analysed with a calculation area of approximately 60×12 μm^2 and 20–40 thousand grid points.
  - Transparent boundary conditions (perfectly matched layers in the *Bend* algorithm)
  - Results used in publications I–II and IV, and Chapters 2.2–2.4, 2.6, and 4.2–4.3.
- *SelenePro* (from Kymata Software), version 3.1.11 for Windows NT 4.0[1]
  - As *TempSelene*, but an older version without thermal analysis.
  - Results used in publications VI–VII and Chapter 2.7.
- *Prometheus* (from Kymata Software), version 4.3.13 for Windows NT 4.0[1]
  - Finite-difference BPM algorithm for simulating light propagation along waveguides with one polarisation at a time (FFT-BPM algorithm not used). 2D and 3D options available.
  - Hierarchial mask editor used for mask design.
  - Results used in publication I and Chapter 2.2.

[1]Presently represented by C2V, http://www.c2v.nl/, originally from BBV Software

PUBLICATION I

Development of silicon-on-insulator waveguide technology

In: Photonics West 2004, San Jose, USA, 26–29 January 2004.
Integrated Optics: Devices, Materials, and Technologies VIII,
Proceedings of SPIE, Vol. 5355, pp. 81–95, 2004.
Reprinted with permission from the publisher.

Invited Paper

Development of silicon-on-insulator waveguide technology

Timo Aalto*[a], Mikko Harjanne[b], Markku Kapulainen[a], Päivi Heimala[a], and Matti Leppihalme[a,b]

[a] VTT Information Technology, Microelectronics,
P.O. Box 1208 (Tietotie 3, Espoo), FIN-02044 VTT, Finland;

[b] Helsinki University of Technology, Optoelectronics laboratory,
P.O. Box 3000 (Tietotie 3, Espoo), FIN-02015 HUT, Finland;

ABSTRACT

An overview of the present silicon-on-insulator (SOI) waveguide technology is given and supplemented with an extensive set of theory and simulation results. Characteristics of slab-, rectangular- and ridge waveguides in SOI are explained. In particular, the number of modes and the single-mode conditions are carefully analyzed. Experimental work with straight and bent 8 to 10 μm thick SOI ridge waveguides and a very fast thermo-optical switch are reported. Propagation loss in a very long spiral waveguide down to 0.3 dB/cm, waveguide birefringence below 10^{-4}, and a switching frequency up to 167 kHz were obtained. A very promising multi-step patterning principle for SOI waveguides is described together with many practical application examples.

Keywords: Silicon-on-insulator, SOI, waveguide, ridge waveguide, thermo-optical switch, polarization, polarization extinction ratio, birefringence

1. INTRODUCTION

Silicon-on-insulator (SOI) waveguides, and high refractive index difference waveguides in general, are very promising for realizing dense photonic integrated circuits (PICs)[1]. They allow extreme miniaturization of PICs due to their ability to realize e.g. ultra small bends, high optical insulation between adjacent waveguides and photonic crystal (PhC) structures[2,3]. SOI waveguides particularly have the advantage of using mature silicon processing technology, and the potential for monolithic integration with electrical and micromechanical structures. SOI waveguide technology is competitive also in less miniaturized and directly fiber coupled telecommunication circuits, where the single mode behavior of large SOI ridge waveguides[4] can be exploited. Such large SOI waveguides have been used to demonstrate e.g. directional and MMI couplers[5], wavelength multiplexers[6], and waveguide gratings[7,8]. High thermal conductivity of silicon can be exploited to make thermo-optic (TO) switches for frequencies well above the typical 1 kHz limit of todays commercial TO switches. A new interferometric modulation technique has been proposed to accelerate TO switches in SOI up to 167 kHz[9]. Fast TO switches based on SOI waveguides can provide a low-cost solution for the optical access networks and the fiber-to-the-home applications. A multi-step patterning principle has been proposed[10] to solve many of the remaining problems in SOI waveguide technology. It can be used to couple light efficiently between various types of waveguides and fibers with different sizes and refractive index distributions. It also enables the realization of highly miniaturized, single moded, and low-loss PICs with reduced processing and packaging costs.

An SOI waveguide has a silicon core ($n \approx 3.5$) surrounded by some cladding material(s), such as air, thermal oxide or deposited oxide, that have n typically between 1 and 2. Therefore, the silicon core always has a very high index difference with respect to the cladding and only a thin cladding layer is needed to insulate the waveguide core from its

* timo.aalto@vtt.fi; phone +358-9-456 6694; fax +358-9-456 7012; http://www.vtt.fi/tte/research/tte6/

Integrated Optics: Devices, Materials, and Technologies VIII,
edited by Yakov Sidorin, Ari Tervonen, Proceedings of SPIE Vol. 5355
(SPIE, Bellingham, WA, 2004) · 0277-786X/04/$15.00 · doi: 10.1117/12.537540

surrounding structures, such as the silicon substrate or any metallic electrodes. In case of standard SOI wafers, there is a buried oxide (BOX) layer between the silicon core and an underlying silicon substrate. Three basic SOI waveguide structures are presented schematically in Fig. 1: a one-dimensional (1D) slab waveguide, a two-dimensional (2D) rectangular waveguide and a 2D ridge waveguide. The very high refractive index difference sets strict requirements for the fabrication technology, especially when the dimensions are small. Single-moded (SM) rectangular SOI waveguides require sub-micron dimensions, which easily leads to intolerable propagation loss due to surface scattering. The smoothness of all etched and polished surfaces becomes an extremely critical factor as the SOI waveguide dimensions approach the sub-micron limit and it is also essential in fabricating thicker ridge waveguides with low propagation and fiber coupling losses.

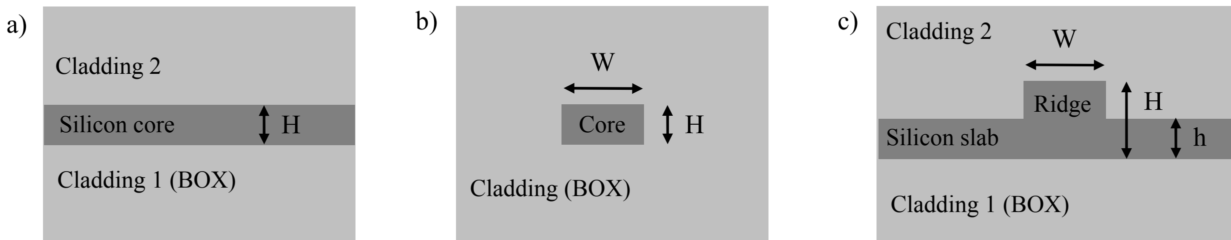

Fig. 1. Schematic cross-sections of three basic SOI waveguide structures: a) slab waveguide (1D), b) rectangular waveguide (2D), and c) ridge waveguide (2D). Dark gray represents the silicon core and light gray represents the cladding materials, which are semi-infinite by default. Silicon core has a height H and a width W. The thickness of the slab surrounding the ridge waveguide is h.

In this paper, theory, simulation results and some experimental results will be represented separately in Chapters 2, 3, and 4 for the above mentioned three basic waveguide structures. Demonstration of very fast (>150 kHz) TO switching in 10 μm thick SOI ridge waveguides is reported in Chapter 5. Finally, the basic principles of the multi-step patterning technology for SOI waveguides are presented in Chapter 6. Throughout the paper, a semi-infinite oxide layer is assumed to surround the silicon core, unless otherwise stated. The material choice for the top cladding has a clear effect on a ridge waveguide's birefringence, as is concluded in Chapter 4. As usual, waveguide modes with the major electric field component aligned horizontally or vertically are labelled TE and TM modes, respectively. The default wavelength is 1550 nm. Most of the experiments are related to approximately 10 μm thick ridge waveguides.

2. SOI SLAB WAVEGUIDES (1D)

To ease the understanding of waveguide modes and the single-mode conditions in SOI waveguides, a brief introduction to the modes in one-dimensional SOI slab waveguides is first presented. A schematic cross-section of the slab waveguide is shown in Fig. 2a. Propagating modes and their effective indices can be easily calculated in this 1D case, for both TE and TM polarization. Two-dimensional SOI waveguide structures (see Chapters 3 and 4) can be approximately analyzed with a so-called effective index method (EIM) by applying the 1D field calculations first in vertical slices of the 2D structure and finally in the horizontal direction (see Fig. 2b).

For simplicity, the following modal analysis is presented only for TE polarization, but the results for TM polarization can be obtained similarly. Calculated effective indices of the first three propagating modes are shown in Fig. 3a as a function of the slab thickness H_{slab}. It can be seen that in several micrometers thick slabs the effective indices have only a slight difference with respect to silicon's refractive index (3.48). When the slab thickness decreases well below 1 μm the effective indices start to decrease rapidly and the modes are cut-off just before their effective indices reach the cladding index (1.46). The cut-off widths for the TE1 and TE2 modes are approximately 250 and 500 nm, respectively. The number of propagating modes N and N^2 are presented in Fig. 3b. Number N increases rapidly with respect to slab

thickness, so that 1 and 10 μm thick slabs already support approximately 5 and 40 modes, respectively. When the waveguide modes are well confined, e.g. when the core dimensions are above 1 μm, the number of modes in a SOI waveguide with a square cross-section can be approximated with N^2. The results in Fig. 3 clearly indicate that SOI slabs and rectangular SOI waveguides must have core dimensions well below 1 μm in order to provide SM operation and that SOI waveguides can have tens or even hundreds of modes already at dimensions below 10 μm.

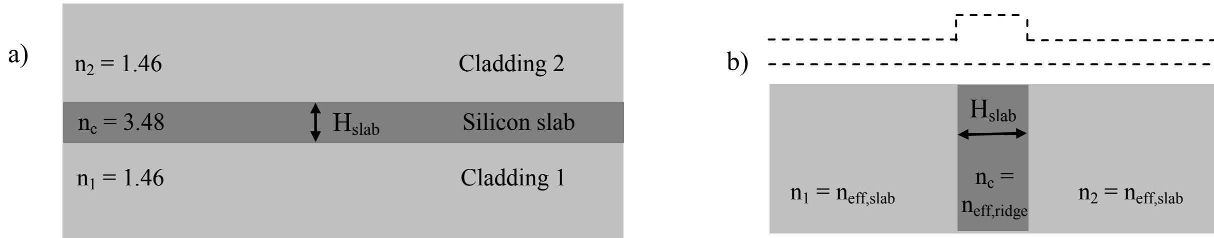

Fig. 2. Schematic cross-section of a 1D SOI slab waveguide with thickness H_{slab}. a) Physical slab structure with a real silicon slab ($n_c = 3.48$). b) Virtual slab structure with calculated effective indices $n_{eff,slab}$ and $n_{eff,ridge}$ as cladding and core indices and H_{slab} equal to ridge width W. This can be used in the effective index approximation of a 2D SOI waveguide, as illustrated by the dashed line.

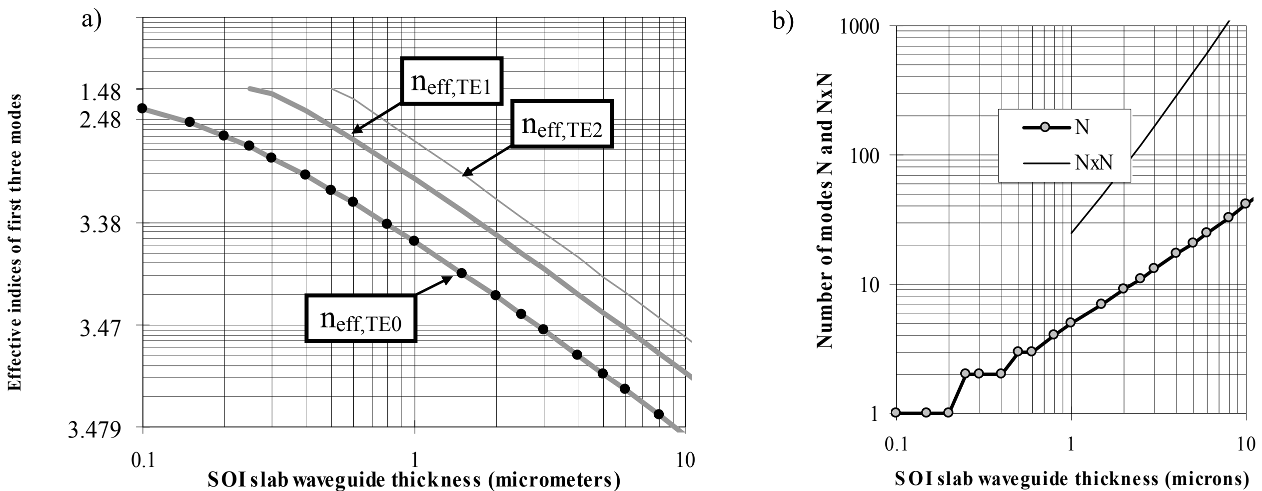

Fig. 3. a) Calculated effective indices of the three lowest TE modes ($n_{eff,TE0\,/\,TE1\,/\,TE2}$) as a function of slab thickness H_{slab} in an SOI slab waveguide. b) Calculated number of propagating waveguide modes N and N^2 as a function of H_{slab}. The latter approximately corresponds to the number of modes in a square waveguide cross-section when the effective index of the mode is close to silicon ($3 \ll n_{eff} < 3.48$).

The combination of extremely high refractive index difference and dimensions above 1 μm was seen to support many propagating modes in SOI slab waveguides. It also confines the propagating modes very efficiently into the silicon core, except for modes that are very close to cut-off. This can be seen in Fig. 4, where the intensity distributions of three lowest order modes are plotted for slab thicknesses 200 nm, 1 μm and 10 μm. The effective index being close to the core index follows directly from the high confinement, as the effective index can be considered to be an weighted average of the propagation media's refractive index.

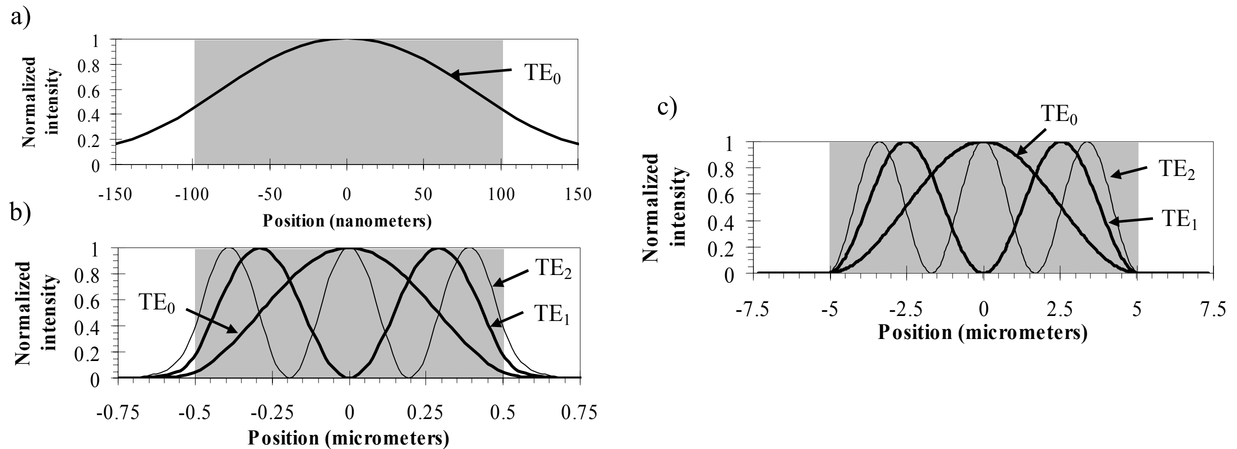

Fig. 4. Calculated intensity distributions of the lowest propagating modes in an SOI slab waveguide with a thickness of a) 200 nm (1 mode), b) 1 µm (5 modes), or c) 10 µm (>40 modes). The gray area illustrates the silicon slab.

3. RECTANGULAR SOI WAVEGUIDES

First theoretical approximation for rectangular SOI waveguides can be based on the effective index method. If the dimensions are well above 1 µm the problem of finding waveguide modes is sufficiently separable with respect to the horizontal and vertical directions. Then the results from Chapter 2 can be readily used to estimate the modal behavior in rectangular waveguides. Based on such an analysis, it can be stated that the rectangular SOI waveguides are multi-moded unless the core dimensions are clearly below 1 µm and that the number of modes increases very rapidly with respect to the dimensions. The fundamental mode is extremely well confined into the silicon core, which leads to some favorable characteristics. For example, the rectangular waveguides can have ultra-small bending radii of a few micrometers[11] and they can even make abrupt changes of course based on total internal reflection (TIR) in so-called waveguide mirrors, as depicted in Fig. 5. With an air or oxide cladding, TIR mirrors can turn the SOI waveguides by more than 90°. Also, arrays of rectangular SOI waveguides can be packed very densely without the risk of any optical or thermal cross-talk between them. This allows for very high miniaturization of PICs on SOI substrates.

Further on, the very high number of modes can be utilized in interferometric components, such as multi-mode-interference (MMI) couplers. The length of an MMI coupler increases with respect to the second power of its width, and the width is limited by the need for a sufficient number of horizontal waveguide modes. In weakly guiding structures a 2×2 MMI coupler's length is typically from a few hundred micrometers to a few millimeters. A rectangular SOI waveguide only needs to have a width of 2.5 µm to support more than 10 horizontal modes. This can lead to MMI couplers with lengths well below 50 µm, enabling very compact PICs.

The very high index difference also poses some important problems that must be solved. Rectangular SOI waveguides tend to be very multi-moded, which seriously limits their applicability e.g. in optical telecommunication and in many interferometric devices. This problem can be tackled by reducing the dimensions of the waveguide to the SM region, but this severely increases scattering losses. A better solution could be to couple light adiabaticly from SM waveguides to rectangular waveguides and back, so that higher order modes are not excited to any relevant extent. This is difficult to realize with traditional waveguide technologies, but it can be obtained with the above mentioned multi-step patterning principle, as is explained in Chapter 6.

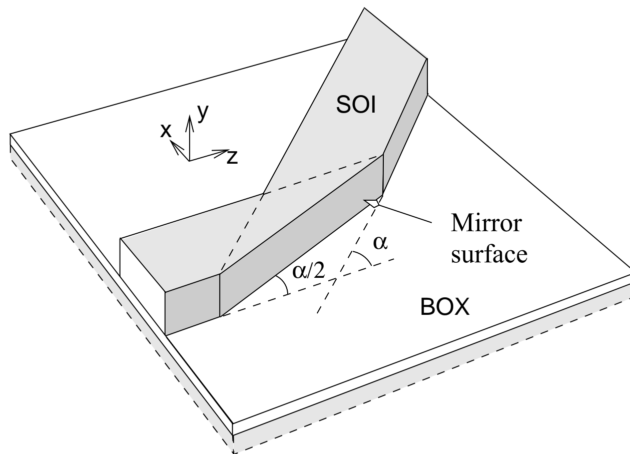

Fig. 5. Schematic view of an abrupt waveguide mirror, which produces total internal reflection between the silicon core and the surrounding cladding (e.g. air or silicon dioxide) and, thus, turns the waveguide by angle α.

Accurate analysis of the rectangular SOI waveguides requires the use of numerical analysis, especially when the core dimensions are close to the single-mode region. Rigorous numerical simulations were applied in a study of modal properties in rectangular SOI waveguides. Simulations were carried out with a commercial software package (*TempSelene* v.4.3) from Kymata Netherlands (currently represented by C2V). The applied algorithm (*BendSolver*) is full-vectorial and capable of calculating both propagating and lossy modes. Simulations verified that the effective index approximation is not valid close to the SM region. The SM limit for a square core was found to be approximately W = H = 350 nm. On the other hand, the SM limit for W was found to be as high as 500 nm for a 250 nm thick silicon core. Calculated intensity distributions of the TE_{00} and TM_{00} modes in three different waveguide cross-sections are presented in Fig. 6. Strong polarization dependency can be clearly observed when the dimensions are reduced beyond the SM limit.

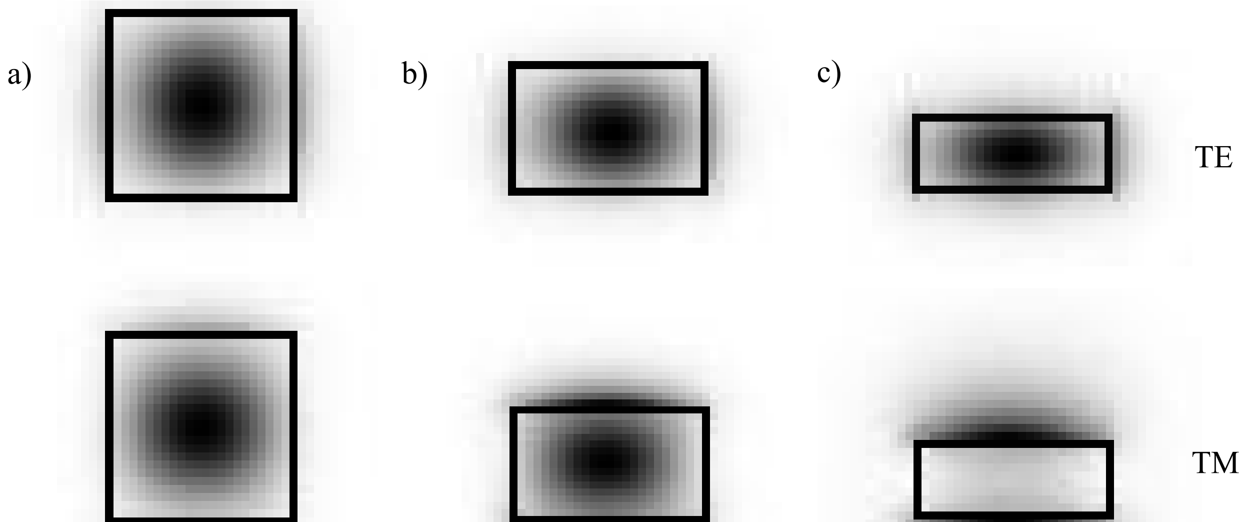

Fig. 6. Simulated intensity distributions of rectangular SOI waveguides separately for TE and TM polarization when the waveguide width is 500 nm and the waveguide height is a) 500 nm, b) 350 nm, or c) 200 nm.

4. SOI RIDGE WAVEGUIDES

4.1 Theory and simulation of ridge waveguides

Ridge type SOI waveguides can be single-moded with both width and height clearly above 10 μm. It should be noted that ridge waveguides are sometimes also referred to as "rib" or "partially etched" waveguides. The thickness of the silicon layer is H within the ridge and h around the ridge. A schematic cross-section of the SOI ridge waveguide with a contour plot of the fundamental mode's intensity distribution is shown in Fig. 7.

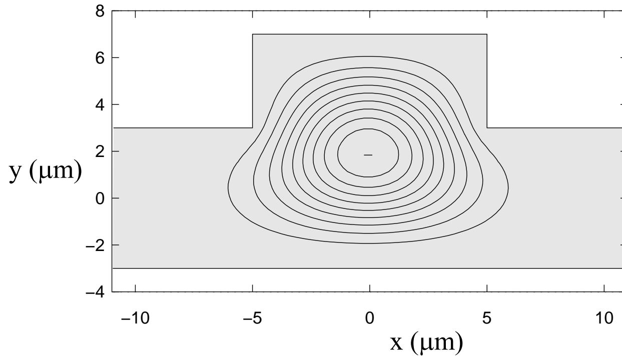

Fig. 7. Schematic cross-section and a calculated intensity distribution of the fundamental mode in a ridge waveguide (H = 10 μm, h = 6 μm, W = 10 μm).

With certain H and h the width W of the ridge is limited by a single-mode condition

$$\frac{W}{H} < 0.3 + \frac{h/H}{\sqrt{1-(h/H)^2}}, \tag{1}$$

as proposed by Soref[4]. This width limitation essentially eliminates the higher order horizontal modes. In practice it assures that the effective index (e.g. $n_{eff,TE10}$) of any higher order horizontal mode in the 2D ridge waveguide is lower than the effective index ($n_{eff,TE0}$) of the fundamental mode in the 1D slab waveguide surrounding the ridge. Thus, all higher order horizontal modes see a negative effective index difference in the horizontal direction and, therefore, leak to the surrounding slab waveguide[10]. On the other hand, propagation of higher order vertical modes is prevented by choosing[4]

$$h/H \geq 0.5. \tag{2}$$

This assures that the lowest intensity maximum of any higher order vertical mode has a negative or zero effective index difference in the horizontal direction and such a mode is always radiative[10]. When the SM limit is approached both horizontal and vertical higher order modes spread into the silicon slab and start to radiate power along the slab away from the ridge. The 1D slab offers these modes an escape port in a similar fashion as a traditional (2D) cladding offers for optical fibers and typical low-index contrast silica waveguides.

According to the effective index approximation, the large refractive index difference is replaced by a much smaller effective index difference in the horizontal direction. As a result, the bending of SM ridge waveguides becomes much more difficult and typically requires a bending radius of several millimeters to avoid harmful bending losses. The strong asymmetry between the horizontal and the vertical direction also tends to cause some geometrical polarization dependency. In particular, the ridge waveguides can be birefringent and the propagation losses in straight and, especially, in curved waveguides can be polarization dependent, as is discussed later.

The two limitations (1-2) together, as proposed by Soref, form a sufficient, but not an exclusive single-mode condition. Single-mode operation can be obtained also when $h/H < 0.5$ if the ridge is sufficiently narrow. Therefore, a detailed analysis of the single-mode conditions was carried out for 10 and 3 μm thick SOI ridge waveguides by using various thickness ratios in the range $0.25 \le h/H \le 0.8$ and by varying the ridge width W in order to locate the maximum width W_{max} for SM operation.

The SM analysis of ridge waveguides was based on rigorous calculations with the above mentioned *TempSelene* simulation software and the same full-vectorial algorithm. All the relevant higher order modes radiate along the silicon slab, so transparent boundary conditions only need to be used in the horizontal direction. Six to ten perfectly matched layers (PMLs) per boundary were used in the horizontal direction to allow higher order modes to spread and radiate into the silicon slab. The calculation grid size was varied between 128×64 and 256×64 and the width of the calculation area was varied between 4 and 8 times H. The rejection of the higher order modes was made by using several different requirements that had to be valid for any propagating mode. The intensity maxima were required to reside below the ridge, the intensity distribution was not allowed to significantly spread out of the calculation area and no significant losses were accepted. These criteria are somewhat dependent on the simulation parameters and, therefore, some results were positioned into a so-called gray-area, instead of putting all the results either to SM or MM region. The true SM limit is expected to lie somewhere within the gray-area. The results are shown in Figs. 8 and 9.

When $0.25 < h/H < 0.4$, the suppression of horizontal TE_{10} and TM_{10} modes requires that W is somewhat smaller than the Soref's maximum width (1). In the same h/H range the elimination of vertical TE_{01} and TM_{01} modes poses a much more strict width limit. SOI ridge waveguides can be SM even when $h/H < 0.3$, but this requires very narrow ridges. At $h/H = 0.3$, for example, 10 and 3 μm thick waveguides are SM when the ridge widths are below 3 and 1 μm, respectively. It should also be noted that higher order vertical modes may appear also when $h/H > 0.5$ if the ridge is sufficiently wide.

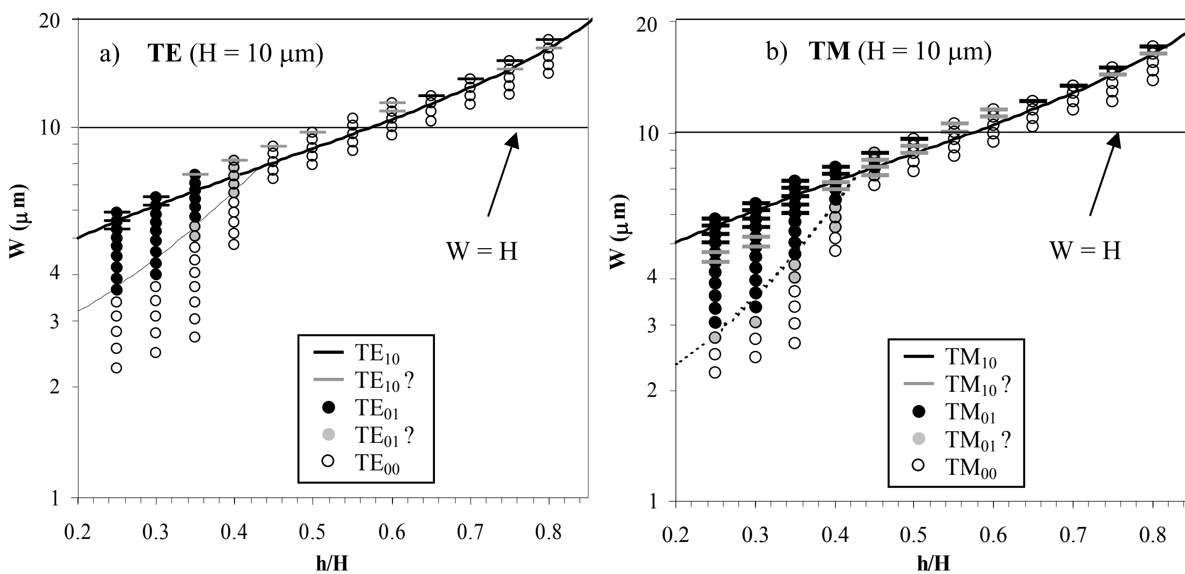

Fig. 8. Simulated SM conditions for 10 μm thick SOI waveguides, separately for a) TE and b) TM polarization. Thick continuous lines represent the maximum width according to Soref's rule, while the thin dashed line represents a new width limit for eliminating the TE_{01} and TM_{01} modes. Circles define simulated structures. Horizontal lines and filled circles indicate higher order horizontal (TE_{10} and TM_{10}) and vertical (TE_{01} and TM_{01}) modes, respectively. Gray color indicates the gray-zone between clearly SM and MM regions.

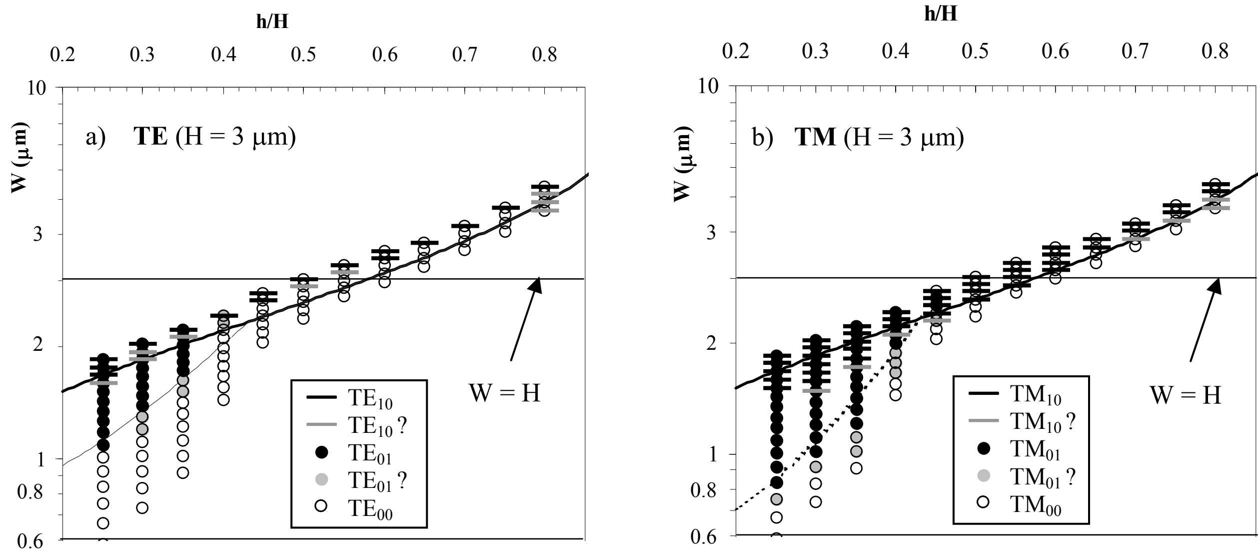

Fig. 9. Simulated SM conditions for 3 µm thick SOI waveguides, separately for a) TE and b) TM polarization. Symbols as in Fig. 8.

As can be seen from Figs. 8 and 9, the SM condition of SOI ridge waveguides is slightly polarization dependent. The waveguides also have a small geometrical birefringence $\Delta n = |n_{eff,TE} - n_{eff,TM}|$ that depends on H, h and W. In typical waveguide structures with H ≈ 10 µm the simulated birefringence is below $5 \cdot 10^{-5}$, but in 1.5 µm thick SOI waveguides it can be as high as $5 \cdot 10^{-3}$.

4.2 Theory and simulation of bends in ridge waveguides

Perhaps the greatest limitation of ridge waveguides is their tendency to cause large bending losses to the propagating light. For example, both measurements and simulations[12] have shown, that in a 10 µm thick ridge waveguide with etch depth of 5 µm, bending radii smaller than 2 cm cause significant losses. This means that high integration densities in PICs are very hard to achieve with thick waveguides.

The amount of bending loss in several bent ridge waveguides was calculated by the same *BendSolver* algorithm as described above. As *TempSelene* can calculate the mode fields in the cylindrical coordinate system, there is no need to use any approximative methods, such as conformal mapping. The software can readily calculate the loss per unit length from the complex propagation constant β that accompanies every mode field. Three waveguides with thicknesses H of 10 µm, 3 µm and 1.5 µm, all with etch depth of H/2, were considered. The Soref's SM condition (1) was used to determine the ridge widths W, resulting in values of 8.8 µm, 2.6 µm, and 1.3 µm, respectively. The calculation parameters used were essentially the same as those given in subsection 4.1. Results from the calculations are presented in Fig. 10.

From the results it can be seen, that bending losses are high for the 10 µm thick ridge waveguide, but that they diminish rapidly as the waveguide is made smaller. Further reduction to the bending loss can be obtained by using larger ridge widths than the ones given by Soref's equation, or by using deeper than H/2 etched waveguides. Despite these alterations to the geometry, the waveguide can still operate in the SM region, because higher order modes are more susceptible to radiate away from the ridge. Finally, it should be noted that the bending loss has a very strong polarization dependency.

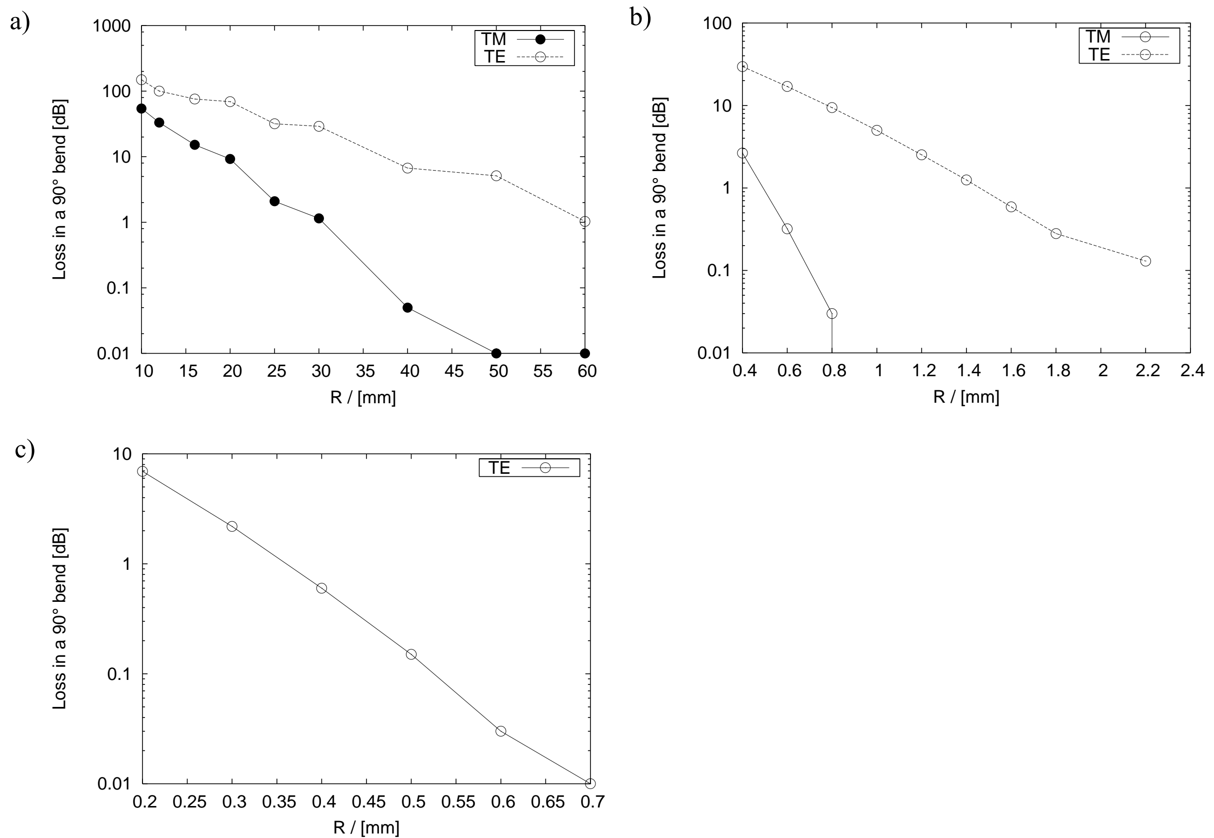

Fig. 10. Simulated bending losses for standard ridge waveguides with thickness H equal to a) 10 μm, b) 3 μm and c) 1.5 μm.

4.3 Fabrication and measurements

Several different waveguides were fabricated with thickness H typically in the range of 8 to 10 μm, etch depth H–h ≈ H/2, width W ranging from 6 to 14 μm and cladding material being thermal oxide (TOX), low-temperature oxide (LTO), TEOS oxide or air (i.e. no cladding). The BOX thickness of the bonded SOI wafers was 1 μm. The waveguide structures were patterned with standard UV-lithography. An oxide hard mask was used for etching the waveguide structure into silicon by inductively coupled plasma (ICP). In the very beginning of the waveguide etching process continuous etching was used. Then the etching continues with alternating passivation and etching steps (etching gas SF_6, passivation gas C_4F_8) to ensure side-wall verticality. The durations of the etching and passivation cycles were both 5 s. After the removal of the residual mask TOX, LTO or TEOS cladding was optionally grown on top of the waveguide. Finally, the waveguides were diced into chips and the endfacets were polished to optical quality.

One problem of characterizing SOI waveguides is to perform accurate propagation loss measurements, since the total propagation loss is comparable to the insertion and coupling losses in short waveguides. Therefore, up to 72 cm long spiral waveguides with bending radii varying between 27 and 42 mm were fabricated to measure the propagation losses accurately. In the measurement setup the laser light was polarized and butt-coupled into a waveguide with polarization-maintaining fiber (PMF). One axis of the PMF was aligned parallel to the chip surface, i.e. horizontally. This ensured that the polarization modes of the input fiber were coupled directly to the polarization modes of the waveguide with minimum cross-talk (below –25 dB). The transmitted light was coupled into a multimode fiber (MMF) and guided to a detector. The setup enabled transmission measurements for both TE and TM polarization. A fiber-to-fiber reference transmission was measured by directly butt-coupling the PMF and MMF. To obtain an exact value for the excess loss of

a waveguide, both the Fresnel reflection loss 3 dB (including both facets) and the theoretical fiber-to-waveguide modal coupling loss (only input facet) were subtracted from the insertion loss.

The measured propagation loss for a 14 μm wide SM spiral waveguide was 0.30±0.05 dB/cm for both TE and TM polarization. It is expected that this loss is still somewhat effected by the spiral bends and that an equally long straight waveguide would provide a lower loss value. However, the roughness of the waveguide side-walls still has the greatest contribution to the measured loss.

The birefringences of the waveguides were measured using the fixed analyzer method[13]. The experimental measurement setup is shown in Fig. 11. Light from a broadband light source was polarized and butt-coupled into the waveguide with a PMF. Polarization axis of the PMF was rotated so that light polarized at a 45° angle was launched into the waveguide. Optical powers coming out of the waveguide in two orthogonal linear polarization states ±45° were measured with a rotatable polarizer as a function of wavelength by using an optical spectrum analyzer. Either one spectrum or a ratio of the two spectra (polarization extinction ratio, PXR) could be used to calculate the birefringence. Waveguide birefringence induces a periodic transmission (or PXR) curve as a function of frequency. The period is equivalent to a phase difference of 2π (one beat length). The birefringence Δn can be calculated using equation

$$\Delta n = m\frac{c}{\Delta f\, L} = m\frac{\lambda_1 \lambda_n}{\Delta\lambda L}, \qquad (3)$$

where m represents the number of periods included in a frequency range Δf, or a corresponding wavelength range $\Delta\lambda = \lambda_n - \lambda_1$, between two transmission (or PXR) maxima (λ_1 , λ_n) and L is the length of the waveguide.

Main problem of the method is that wavelength dependence of the birefringence has an effect on the results, especially when the birefringence is low, because measurements require the use of a broad spectrum. However, wavelength dependence was not observed in our SOI waveguide measurements in the wavelength range from 1350 to 1600 nm.

Figure 12a shows measured PXR spectra from straight waveguides with LTO and TEOS claddings. Periodic response of the transmission signal is well seen in the case of LTO. Birefringence value of $6{\cdot}10^{-4}$ was obtained using equation (3). It can be seen that TEOS cladding produces a clearly lower birefringence than LTO. Approximately one half of a period is seen in the TEOS spectrum, which lead to an estimated birefringence of $1{\cdot}10^{-4}$. The fixed analyzer method could not provide an accurate birefringence value for a waveguide with air cladding because the associated spectrum showed less than one half of a period, which indicates a birefringence of less than $1{\cdot}10^{-4}$. Measured birefringence for a straight waveguide with TOX cladding was similar to the results for LTO and it is shown in Fig. 12b as a function of W. A maximum of $6.8{\cdot}10^{-4}$ and a minimum of $1.5{\cdot}10^{-4}$ were obtained with waveguide widths 6 and 2 μm, respectively.

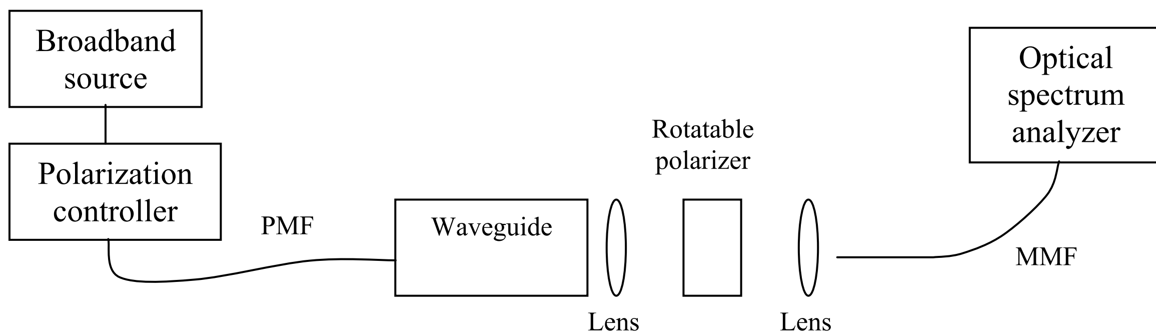

Fig. 11. Measurement setup used to determine waveguide birefringencies.

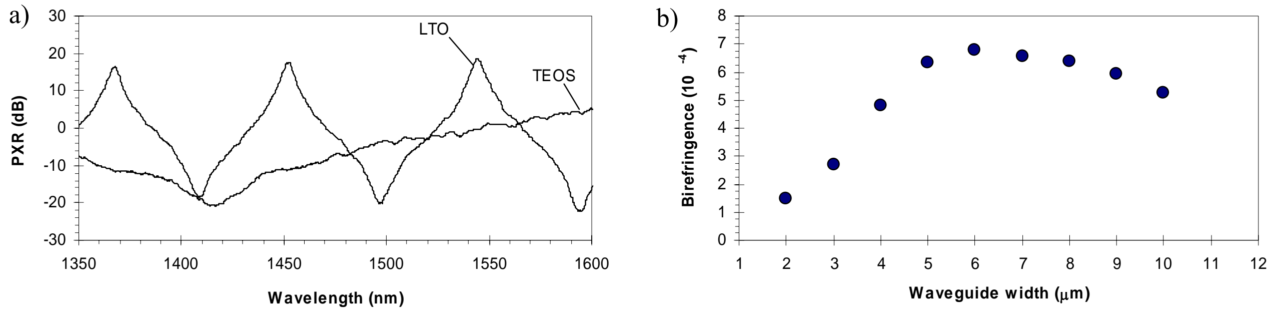

Fig. 12. a) Measured PXR spectra from two 4 cm long waveguide samples with LTO and TEOS claddings (H ≈ 9 μm, W = 8 μm). b) Measured birefringence as a function of waveguide width in a 71 mm long sample chip with TOX cladding (H ≈ 9 μm).

5. THERMO-OPTICAL SWITCHING IN SOI RIDGE WAVEGUIDES

Typical TO switches made from silica or polymers typically have a maximum frequency below 1 kHz. This is mostly due to their poor thermal conductivity, relatively large core size and thick cladding, which is necessary to optically insulate the waveguide from the heating electrode. Thick SOI ridge waveguides have good thermal conductivity and a thin top cladding between the heating electrode and the silicon core. These characteristics lead to faster switching operating, but also to a somewhat higher power consumption than what is seen in the well insulated and slow switches.

To study the potential of SOI waveguides in optical switching, a TO switch based on a 9 μm thick SOI ridge waveguide was fabricated and characterized. The switch was implemented by using a 2x2 Mach-Zehnder interferometer (MZI) layout and it was operated by using both conventional square wave modulation and a new interferometric modulation technique. The cross-section of the SOI waveguide with an aluminum heater on top is shown in Fig. 13a. Detailed design and fabrication of the switch are published elsewhere[14,9]. The switch is in a cross state (off), when the heating elements are not operated. It turns into a bar state (on) when a temperature difference corresponding to a phase difference of $\Delta\phi$ = 180° is applied between the two waveguide branches by operating at least one of the heaters. The optimum bar- and cross-states can be obtained only when the directional couplers (DCs) are identical and their lengths correspond to perfect 50:50 (-3 dB) power division.

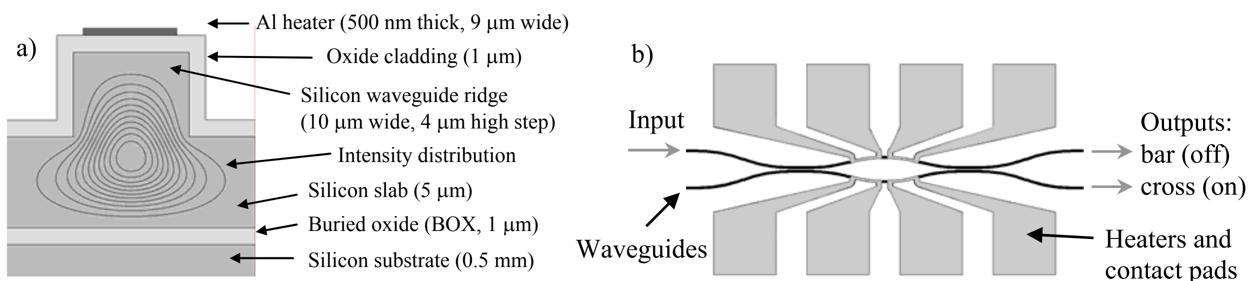

Figure 13. a) Cross-section of a SOI ridge waveguide with an aluminum heater on top of the ridge. The intensity distribution of the fundamental mode is again shown with contour lines. b) A schematic layout (top-view) of the 2x2 MZI switch.

Before carrying out the switching measurements, the switches were characterized optically without heating them. This showed strong polarization dependency and slightly non-ideal DC lengths. Therefore, all the following results are obtained with TE polarized input light and the switches have a maximum extinction ratio (ER) of 17 dB (98:2). During

the switching, this is an optimum value that represents perfect phase modulation. The polarization dependency and the ER can be improved without a significant change in the modulation frequency. The heating power P in the active waveguide branch was then adjusted to P_{on} so that a static on-state was optimized, resulting in P = P_{on} = 300 mW. The maximum frequency for full phase modulation (~99%) with P = P_{on} was approximately 10 kHz. For lower phase modulation depths, e.g. 90% or 50%, the frequency can be clearly above 10 kHz. This already represents an order of magnitude improvement with respect to commercial TO switches.

The details of the new modulation method are presented elsewhere[9], but the basic principle is explained in the following and presented in Fig. 14a. Instead of heating just one waveguide branch, both branches of the MZI are used for heating. In the off state they are heated with equal power, while in the on state only one of the branches is heated. Further on, both the rise and fall time are remarkably shortened by applying a high heating power peak to the other branch and by dropping the heating power of the other branch to zero. The new method increases the frequency very efficiently with respect to power consumption and it can be applied to increase the operational frequency or the response time of other interferometric components as well. In case of the fabricated SOI switch, the switching speed was pushed up to 167 kHz. This was the maximum for the very simple and inexpensive control electronics used. Even at 167 kHz the ER was still better than 13 dB (95:5), i.e. close to the optimum. Average total heating powers were 120 mW and 350 mW during off- and on-states, and 760 mW and 1.13 W during the 3 μs long fall- and rise-times, respectively. In random modulation all alternatives are equally popular and the average heating power is 590 mW.

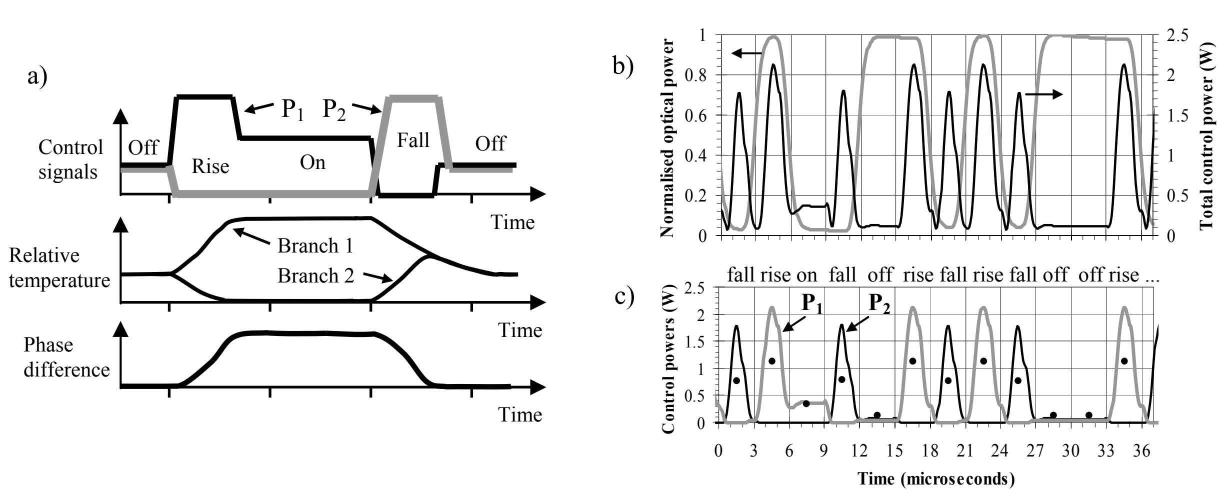

Fig. 14. a) Schematic principle of the new modulation method. Measured results at 167 kHz: b) Optical response (cross-state output) and total heating power. c) Heating powers of the two branches (P1, P2), and an average power for every 3 μs time span (black dots). Optical signal has a 2 μs delay with respect to P1 and P2 (labels on top refer to heating pulses).

6. MULTI-STEP PATTERNING OF SOI WAVEGUIDES

Traditionally, optical waveguides are patterned by using a single mask layer. Other mask layers may be used to define heaters etc, but typically they do not contribute to the basic waveguiding. Using a single mask layer to define optical waveguiding is sufficient for most applications and it is much more simple to realize than aligning different mask layers with respect to each other with the required accuracy.

However, the use of more than one mask layer in the patterning of a single SOI waveguide cross-section has significant advantages, as is explained in the following. The principle is called multi-step patterning and its potential is illustrated by presenting four different SOI waveguide structures that have significant advantages over traditional waveguides. The

main advantages of these multi-step waveguides are the potential for extreme miniaturization and the ability to efficiently couple light between different types of waveguides and fibers.

First, two different structures for converting a ridge waveguide into a rectangular waveguide (or vice versa) are shown. For simplicity, only two mask layers have been used. However, one can also use more mask layers, either in a single waveguide cross-section or by connecting waveguides with different mask layer pairs, one after another. The two structures are schematically presented in Fig. 15. The first transformation occurs between a ridge waveguide and a smaller rectangular waveguide, while the second transformation involves ridge waveguides and rectangular waveguides of equal height. Both of them can be used to combine the advantages of ridge waveguides (SM, thick, low loss) and rectangular waveguides (tight bends, mirrors, short MMIs).

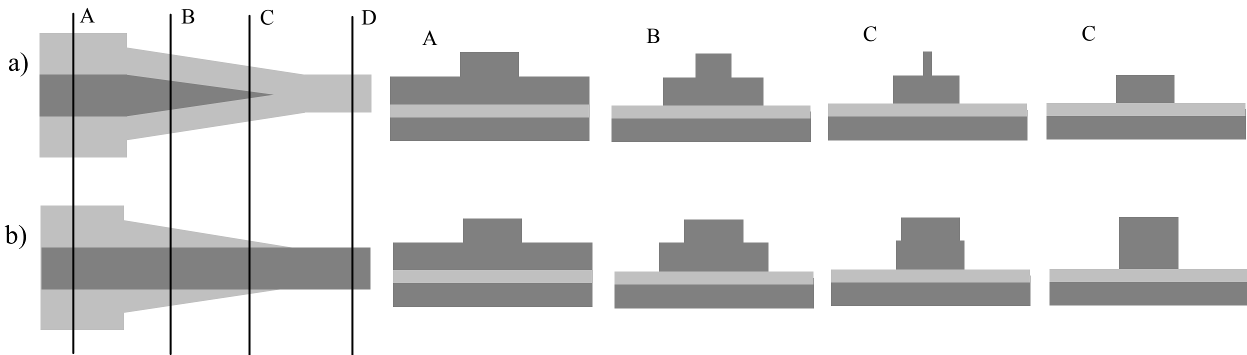

Fig. 15. Two different 3D waveguide tapers between a rectangular and a ridge waveguide. The height of the ridge is a) greater than or b) same as the height of the rectangular waveguide. The layouts on the left describe the structures as seen from the top and the cross-sections A, B, C and D are shown on the right.

The changing of the waveguide cross-sections must be carried out adiabatically, i.e. in a sufficiently small angle with respect to propagation. Depending on the type and the size of the waveguide, this may require relatively long tapering areas, such as tens or even hundreds of micrometers. The alignment between the mask layers must be carried out accurately, but the alignment tolerances can be partially relaxed by using appropriate processing steps. In the 3D tapers shown in Fig. 15 the definition of the waveguide can be transferred from one mask layer to another, so that both mask layers have a relevant contribution to the waveguiding only in the tapering region. The sharp tip in Fig. 15a will have a finite width due the finite lithographic resolution. However, according to the simulations the effect of the tip on the fundamental mode becomes negligible when the tip width becomes much smaller than the width and the height of the underlying rectangular waveguide. It should be noted that these 3D tapers also allow for efficient coupling between a PhC waveguide and a SM ridge waveguide. In the miniaturization of PICs the input waveguides and local mode strippers can be formed of SM ridge waveguides, while the bends, waveguide mirrors, couplers and other such structures can be realized densely with small rectangular waveguides.

The third type of transformation connects two ridge waveguides that have different heights. This transformation is described schematically in Fig. 16. It shows a similar sharp tip as in Fig. 15a, but also here the finite width of the tip becomes negligible with a sufficiently wide shallow ridge. The main application of this structure is to change the height of a waveguide without losing the SM behavior. Several successive tapers can be used to obtain very large height differences. Larger waveguides are especially useful for low-loss propagation of longer distances and for coupling with hybrid integrated waveguides, fibers and lasers. The smaller waveguides, on the other hand, are better for realizing ultra-small PICs and fast modulators or switches.

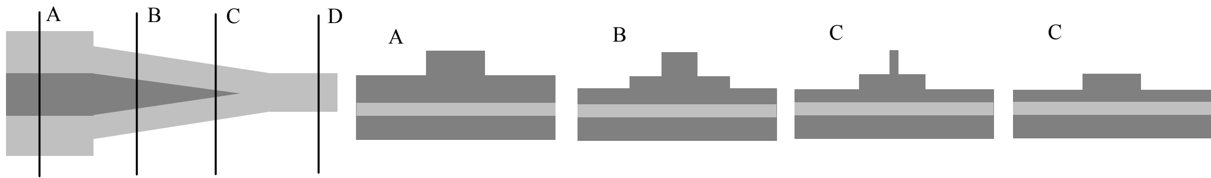

Fig. 16. A 3D waveguide taper connecting two ridge waveguides with different heights. The layout on the left describes the structure as seen from the top and the cross-sections A, B, C and D are shown on the right.

The fourth example of multi-step SOI waveguides is an asymmetric bend. By etching a shallow groove next to the SM waveguide ridge the effective index difference of the fundamental mode can be locally increased. This allows to realize small waveguide bends without forcing the waveguide to MM operation. The distance and width of the groove can be tuned along the bend to obtain an optimum for the transmission without launching the higher order modes. A schematic layout of the structure is shown in Fig. 17, together with contour plots of the fundamental mode. It can be clearly seen that the very high bending loss of the ridge waveguide can be completely suppressed by using the groove.

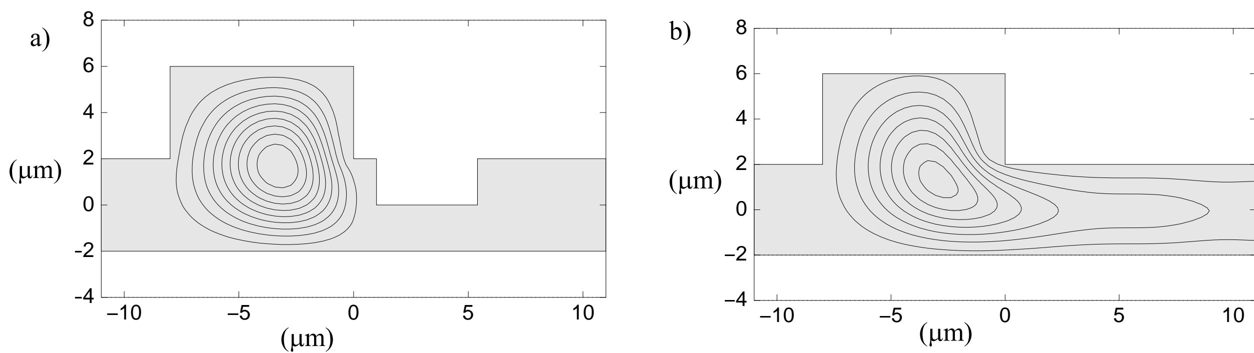

Fig. 17. Cross-sections and calculated intensity distributions of SOI waveguides with a bending radius of 10 mm a) with and b) without an additional groove.

According to the simulations[12] carried out in this work there is a lot of potential in realizing extremely compact optical circuits based on multi-step SOI waveguides. The use of additional etch steps requires the use of additional lithography masks and process steps, but the advantages should clearly overcome the associated extra efforts in fabrication. The basic principle of multi-step patterning can be applied to thick (e.g. 10 μm) as well as thin (e.g. 1 μm) waveguides.

7. CONCLUSIONS

Silicon-on-insulator waveguide technology has strong potential in providing ultra-compact, highly efficient and low-cost PICs in the future. Further development of the fabrication technology will shortly provide the means to realize efficient coupling from standard fibers and thick SOI ridge waveguides to very thin SOI waveguides (ridge or rectangular) as well as to photonic crystal structures fabricated in SOI. The high bending losses in thick SOI waveguides can be eliminated by applying additional grooves to the outer sides of the waveguide bends. Waveguide arrays and devices such as MMI couplers and switches can be made very small by taking advantage of the excellent confinement and high number of modes in rectangular waveguides. The advantages of SOI technology become more and more apparent when the integration and miniaturization level of PICs is increasing. It will have applications not only in optical telecommunication, but also in optical interconnections and, perhaps, in sensor technologies as well.

When developing the SOI waveguide technology one must keep the roughness of the etched silicon surfaces very small to avoid any significant scattering losses and the roughness must even be reduced from the present values when the waveguides dimensions are reduced to the sub-micron range. However, the present SOI waveguide technology can already provide losses that are competitive with other waveguide technologies, such as the 0.3 dB/cm propagation loss measured from bent waveguides within this work. Waveguide birefringence is also an important issue, especially in small waveguides, and the selection of an appropriate cladding material appears to be crucial in keeping it low.

ACKNOWLEDGEMENTS

This work was partly supported by The European Space Agency under ESTEC Contract Number 17703/03/NL/PA and Tekniikan Edistämissäätiö (Technology Development Fund, Finland). Markku Rönö, Kimmo Solehmainen, and Kai Kolari are acknowledged for their valuable contribution to the work.

REFERENCES

1. B. Jalali, "Silicon-on-insulator photonic integrated circuit (SOI-PIC) technology", *SPIE Proc.* **2997**, pp. 60-71, 1997.
2. K. Hosomi, T. Katsuyama, "A dispersion compensator using coupled defects in a photonic crystal", *IEEE J. Quantum Electron.* **38**, pp. 825-829, 2002.
3. S. Yliniemi, T. Aalto, P. Heimala, P. Pekko, K. Jefimovs, J. Simonen, T. Uusitupa, "Fabrication of photonic crystal waveguide elements on SOI", *Proc. SPIE* **4944**, pp. 23-31, 2003.
4. R. A. Soref, J. Schmidtchen, K. Petermann, "Large single-mode rib waveguides in GeSi-Si and Si-on-SiO_2", *IEEE J. Quantum Electron.* **27**, pp. 1971-1974, 1991.
5. T. Zinke, U. Fischer, B. Schüppert, K. Peterman, "Theoretical and experimental investigation of optical couplers in SOI", *Proc. SPIE* **3007**, pp. 30-39, 1997.
6. P. D. Trinh, S. Yegnanarayanan, F. Coppinger, B. Jalali, "Silicon-on-insulator (SOI) phased-array wavelength multi/demultipelexer with extremely low-polarization sensitivity", *IEEE Photon. Technol. Lett.* **9**, pp. 940-942, 1997.
7. T. Aalto, S. Yliniemi, P. Heimala, P. Pekko, J. Simonen, M. Kuittinen, "Integrated Bragg gratings in silicon-on-insulator waveguides", *Proc. SPIE* **4640**, pp. 117-124, 2002.
8. A. Cutolo, M. Iodice, A. Irace, P. Spirito, L. Zeni, "An electrically controlled Bragg reflector integrated in a rib silicon on insulator waveguide", *Appl. Phys. Lett.* **71**, pp. 199-201, 1997.
9. T. Aalto, M. Kapulainen, S. Yliniemi, P. Heimala, and M. Leppihalme, "Fast thermo-optical switch based on SOI waveguides", *Proc. SPIE* **4987**, pp.149-159, 2003.
10. T. Aalto, P. Heimala, S. Yliniemi, M. Kapulainen, and M. Leppihalme, "Fabrication and characterization of waveguide structures on SOI", *Proc. SPIE* **4944**, pp.183-194, 2003.
11. A. Sakai, T. Fukazawa, T. Baba, "Low loss ultra-small branches in a silicon photonic wire waveguide", *IEICE Trans. Electron.* **E85-C**, pp.1033-1038, 2002.
12. M. Harjanne, T. Aalto, "Design of tight bends in silicon-on-insulator ridge waveguides", Accepted for publication in *Physica Scripta*
13. Y. Namihira, J. Maeda, "Comparison of various polarisation mode dispersion measurement methods in optical fibres", *Electron. Lett.* **28**, pp. 2265-2266, 1992.
14. T. Aalto, P. Heimala, P. Katila, "Integrated optical switch based on SOI-technology", *Physica Scripta* **T79**, p. 123-126, 1999.

PUBLICATION IV

Fast thermo-optical switch based on SOI waveguides

In: Photonics West 2003, San Jose, USA, 27–29 January, 2003.
Integrated Optics: Devices, Materials, and Technologies VII,
Proceedings of SPIE, Vol. 4987, pp. 149–159, 2003.
Reprinted with permission from the publisher.

Fast thermo-optical switch based on SOI waveguides

Timo Aalto*[a], Markku Kapulainen[a], Sanna Yliniemi[a,b], Päivi Heimala[a], and Matti Leppihalme[a,b]

[a]VTT Centre for Microelectronics, [b]Optoelectronics laboratory, Helsinki University of Technology

ABSTRACT

Thermo-optical silicon-on-insulator (SOI) waveguide switch has been fabricated and characterized. The switch is based on a 2x2 Mach-Zehnder interferometer and 9 microns thick ridge waveguides. The extinction ratio of the switch is 17 dB with ultra-slow modulation and it is limited by the unoptimized directional coupler lengths. Thermo-optical switching with conventional on/off modulation was demonstrated up to 10 kHz. The average power consumption was 150 mW and the extinction ratio was 15 dB in 10 kHz square wave modulation. By using a novel modulation principle the maximum frequency was rised up to 167 kHz, while still maintaining the 15 dB extinction ratio in square wave modulation. With random binary modulation at 167 kHz frequency (3 μs per bit) the extinction ratio remained above 13 dB and the average power consumption was 590 mW. The obtained frequency limits for square wave modulation correspond to a maximum of 1% deviation from the attainable extinction ratio limits. With less strict extinction ratio requirements the maximum frequencies can be much higher. The new modulation method can be used to radically speed up interferometric switches with a tolerable increase in the power consumption.

Keywords: Silicon-on-insulator, SOI, waveguide, thermo-optical switch, phase modulation, Mach-Zehnder interferometer

1. INTRODUCTION

Inexpensive and sufficiently fast optical switches are one of the key elements when the optical communication technology continues its expansion from the backbone networks to the access networks. Switches close to the end users must be inexpensively mass produced. Optical switches can be roughly divided into two categories based on their frequency range. Fast switches operate above 1 MHz and they are typically based on nonlinear effects, electro-optical modulation or current injection modulation. Slow switches operate below 1 MHz. Actually, they are typically based on thermo-optical (TO) modulation or micro-electro-mechanical systems (MEMS) that operate well below 10 kHz. The slow switches, and especially the thermo-optical switches, are typically much less expensive than the fast switches. There is clearly a lack of inexpensive switches that can operate in the 10-1000 kHz range. Currently available TO switches typically have a maximum frequency of 1 kHz or less.

In scientific papers there have been some examples[1,2,3] of thermo-optical switches that operate above 10 kHz. Fischer et al, for example, have demonstrated a thermo-optical 1x1 Mach-Zehnder (MZI) switch with 5 μs rise time and 150 mW power consumption by using silicon-on-insulator (SOI) technology[2]. However, their small waveguide structure was not optimized for fiber coupling, the optical wavelength was 1300 nm and the continuously modulated operation was not reported.

* timo.aalto@vtt.fi; phone +358-9-456 6694; fax +358-9-456 7012; http://www.vtt.fi/tte/research/tte6/;
VTT Centre for Microelectronics, P.O. Box 1208 (Tietotie 3, Espoo), FIN-02044 VTT, Finland;

Integrated Optics: Devices, Materials, and Technologies VII, Yakov S. Sidorin, Ari Tervonen, Editors, Proceedings of SPIE Vol. 4987 (2003) © 2003 SPIE · 0277-786X/03/$15.00

Silicon-on-insulator technology offers a relatively inexpensive method to fabricate thermo-optical switches. The high thermo-optical constant ($1.86 \cdot 10^{-4}$ K^{-1}) and good thermal conductivity of silicon can make SOI switches faster than most other TO switches. SOI technology can also be used to integrate different optical, electrical and micromechanical functions onto a common substrate. The advantages and disadvantages of SOI waveguides have been discussed in detail elsewhere[4,5,6].

In this work, TO switches have been realized based on SOI ridge waveguides with a large cross-section[6]. The waveguides have a modal fiber coupling loss clearly below 1 dB (<0.3 dB for optimized design), and a propagation loss below 0.5 dB/cm. Due to a thermal oxide cladding the waveguides are polarization dependent, but this property should be eliminated by choosing an appropriate cladding material, as the results from some polarization independent SOI waveguides indicate[7]. The switches are implemented by using a 2x2 MZI layout and the optical wavelength is 1550 nm. The devices have been operated by using both conventional modulation and a novel interferometric modulation technique. The continuously modulated 167 kHz operation of a TO switch with a large waveguide core and a 15 dB extinction ratio is the fastest result so far reported. The novel modulation principle is now proposed and demonstrated for the first time, and it can be applied to radically increase the operational frequency or the response time of other interferometric switches as well.

2. BACKGROUND ON THERMO-OPTICAL SWITCHING

Thermo-optical switches are often assumed to be limited clearly below the 10 kHz frequency due to the slow thermal conduction in optically transparent materials. In general, TO switches can be made faster by reducing the waveguide size. Unfortunately, this normally leads to higher optical losses, both due to the size mismatched fiber-waveguide interconnections and the increased scattering losses. Thermal conductivity between the heater and the waveguide should be maximized, but this is normally limited by the need for sufficient optical insulation. In low-index contrast (low Δn) waveguides the distance between the core and the heater element must be several micrometers. Increasing the thermal conductivity around the heated waveguide makes the switch faster, but it also increases the power consumption. This leads to a trade-off between the speed and the power consumption. In many waveguide structures the requirement for sufficient optical confinement also limits the possibility to increase thermal conductivity between the waveguide core and the underlying substrate.

In addition to the waveguide structure, also the switching structure, or the principal layout, effects the characteristics of a switch. Typical TO switches are based on a 1x1, 1x2 or a 2x2 MZI structure. Larger matrices are obtained by cascading these fundamental switching blocks[8]. The extinction ratio of a switch can be improved by directing the signal through more than one fundamental switching block in each switching node[8]. Two successive switches with 20 dB extinction ratios produce a total extinction ratio of 40 dB. The disadvantages of this principle are increased power consumption and larger device area. In general, the 2x2 switch is more difficult to realize than the 1x1 switch, or a modulator, while the 1x2 switch lies somewhere in between. This is due to the increased number of input and output ports and the requirement for even transmission between different ports. In a 1x1 switch, or in a modulator, the modulation can be based on absorption, while this is not possible in an interferometric 1x2 or 2x2 switch.

There are several tricks that can be used to increase the switching speed or to reduce the response time of the switch without modifying the actual switch structure. Firstly, the switching speed can be significantly increased if one satisfies with a lower output extinction ratio or, in another words, lower modulation depth. For example, a 3 dB extinction ratio can be achieved with a much higher frequency than a 20 dB extinction ratio. Secondly, single transitions between different switching states may be obtained with very short rise or fall times, but these do not automatically guarantee acceptable operation in continuously modulated operation. For example, an ultra-short rise time is not very useful if the fall time is much longer. In some cases the convergence of successive transitions may also cause e.g. heat build-up that

limits the maximum frequency. Finally, surprisingly fast operation may be obtained by using square wave modulation and so called overdriven switching (or overshooting)[9]. Unfortunately, this principle does not support any controlled switching operations.

Due to the multitude of parameters and switching principles one should be careful when comparing different switching solutions. In addition to the maximum switching speed itself, one should also pay attention to the type of the switch (1x1, 1x2, 2x2, ...), type of modulation (e.g. random or square wave), the insertion loss, the extinction ratio (or the modulation depth), the polarization characteristics, the power consumption and the price.

3. DEVICE DESIGN

A detailed description of the device design has already been published elsewhere[10]. Therefore, only a short summary and update of the design will be given here. It should be noted that the mask layout has not been optimized after the initial design, thus leaving plenty of room for future improvement with respect to e.g. extinction ratio and device size. The waveguide width in the old lithography mask is W = 10 μm. The SOI wafers used in this work had a slightly thinner SOI layer (9 μm) than the wafers used in the original design (10 μm)[10]. Therefore, the vertical dimensions of the waveguide were slightly modified to maintain single-moded operation. The silicon core is surrounded by 1 μm thick optically insulating oxide layers and the thin film heater is on top of the ridge. The SOI ridge waveguide structure is presented schematically in Fig. 1a.

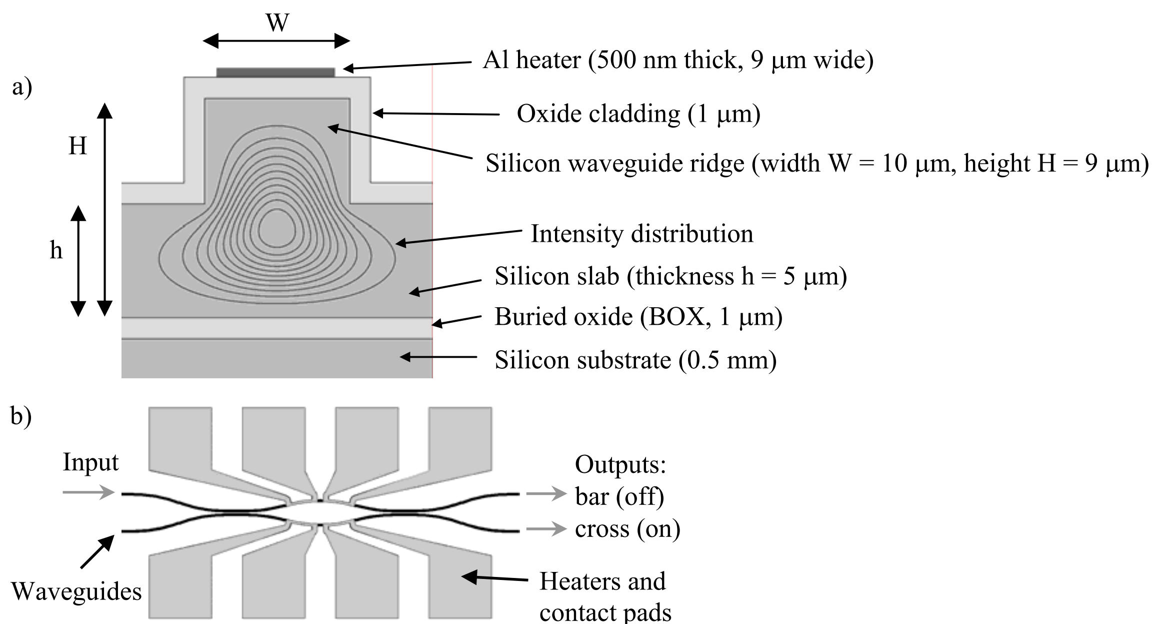

Figure 1: a) Cross-section of the SOI ridge waveguide with an aluminum heater on top of the ridge. The intensity distribution of the fundamental mode is shown with contour lines. b) A schematic layout (top-view) of the 2x2 MZI switch.

Ridge type silicon-on-insulator waveguides have a very large refractive index contrast (high Δn) between the silicon core (n ≈ 3.5) and the surrounding oxide (or air) cladding (n ≈ 1.5 or 1). Nevertheless, they can be single-moded (SM) even when the width and the height are both several micrometers. This is because the ridge (width W, total thickness H)

is surrounded by a slab waveguide (thickness h) that offers an "escape path" for the higher order modes. The SOI ridge waveguide is single-moded when both the conditions[11]

$$\frac{W}{H} < 0.3 + \frac{h/H}{\sqrt{1-(h/H)^2}} \quad \text{and} \tag{1}$$

$$h/H \geq 0.5 \tag{2}$$

are satisfied. In the fabricated waveguide switch the width, the ridge height and the slab height were W ≈ 9 μm, H ≈ 9 μm, and h ≈ 5 μm, respectively. Therefore, the device is operating at the boundary between single- and multi-moded operation. The validity of the above mentioned single-mode conditions can be, and has been, verified both by solving the propagating modes of different ridge waveguides numerically and by observing the output of realized ridge waveguides with an IR-camera. The modal fiber coupling loss between the waveguide and a standard single-mode fiber is clearly below 1 dB[6,10]. This can be suppressed down to 0.3 dB by optimizing the waveguide cross-section[10].

The waveguide switch consists of two cascaded waveguide couplers with thermo-optic heaters on both waveguide arms connecting the two couplers. A schematic layout of the 2x2 MZI switch is shown in Fig. 1b). The coupling coefficient for directional couplers is difficult to calculate accurately, because it is affected by the coupling between the bent waveguides, the etch depth, the linewidth changes (during the process), etc. Therefore, several directional couplers with different waveguide spacings and lengths were designed to determine their coupling behavior experimentally. Five different directional coupler lengths were used to define five different switch versions on the mask. These lengths determine the attainable extinction ratio of the switch.

The 2x2 MZI switch is in a cross state (off), when the heating elements are not operated. It turns into a bar state (on) when a temperature difference corresponding to a phase difference of $\Delta\phi = 180°$ is applied between the two waveguide branches by operating one or more heaters. The optimum bar- and cross-states can be obtained only when the directional couplers are identical and their lengths correspond to perfect 50:50 (-3 dB) power division.

According to the thermal modelling[10], a 3 K temperature change is enough to switch the output state of the device. The rise (0%→90%) and the fall (100%→10%) times were both estimated to be 200 μs and the electrical power consumption was estimated to be 120 mW. The response times correspond to a maximum frequency of approximately 2.5 kHz. Calculated cross-sections of two temperature change distributions during waveguide heating are plotted in Fig. 2. The cooling takes place with the same speed, but then the temperature change distributions are much more flat. Heat conducts very efficiently from the heater into the silicon ridge and then spreads horizontally along the silicon slab. Silicon has a relatively high TO constant ($1.86 \cdot 10^{-4}\ K^{-1}$) and good thermal conductivity, while the oxide cladding is very thin. This results in a rapid optical phase change in the waveguide. Finally, heat diffuses through the thin buried oxide (BOX) layer into the silicon substrate that behaves as a small heat sink. The exact temperatures, diffusion times and heating powers are strongly dependent on the boundary conditions. These, on the other hand, depend on the actual environment around the chip. Modifications in the airflow and in the bonding of the chip to an underlying support plate may cause significant changes in the exact values.

In conclusion, according to the design and simulations, the SOI waveguide switch can be modulated much faster than most other TO switches. This is due to the good thermal conductivity between the heater, the core and the substrate, which is difficult to realize for low Δn waveguides. Only 1 μm thick oxide layers are sufficient to confine the waveguide optically, while the SOI layer acts as an efficient heat spreader[10]. The corresponding increase in the power consumption is unavoidable, but owing to the efficient heat confinement into the waveguide core, the power increase is very reasonable with respect to the increased frequency.

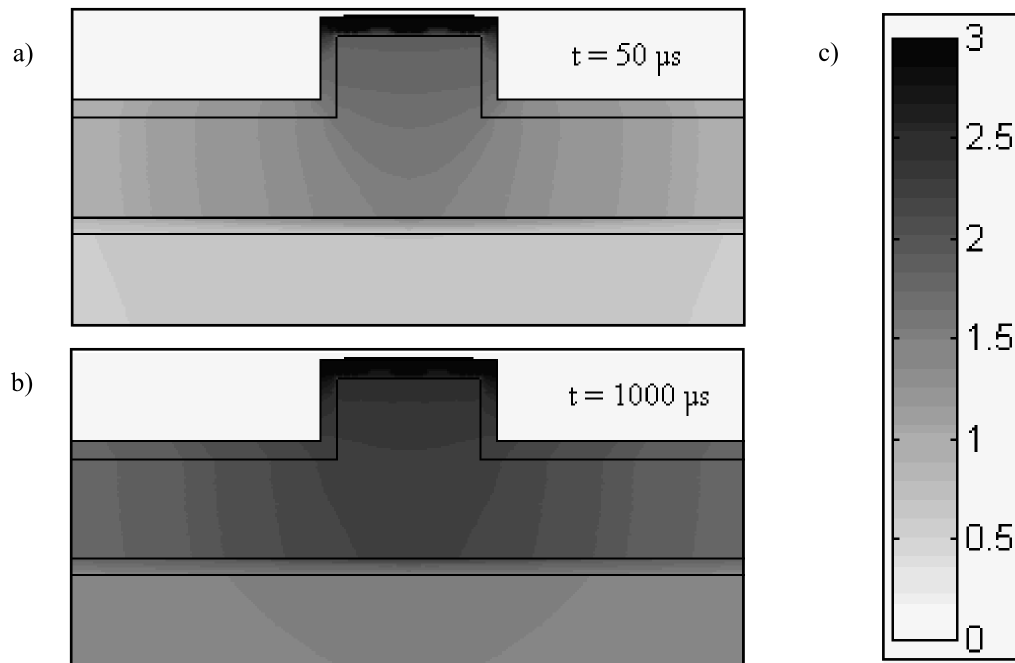

Figure 2: Calculated cross-sections of two temperature change distributions. The heat is generated in the thin film heater lying on top of the waveguide ridge and the total heating power is 10 mW. a) Situation 50 μs after the heating has started. b) Situation 1 ms after the heating has started (stabilized situation). c) Temperature change scale.

4. FABRICATION

Bond-and-etchback SOI (BESOI) wafers were used for fabricating the SOI waveguide switches. The active silicon layer thickness was 9.3 μm and the buried oxide layer thickness was 1 μm. This BOX thickness was enough to prevent any leakage of optical power into the underlying silicon substrate.

The switch fabrication was done in two phases. First, passive SOI waveguide structures were defined and second, thermal control was introduced by fabricating heating structures on top of the waveguides.

Waveguide fabrication was started with growing a 500 nm thick oxide layer using plasma-enhanced chemical vapor deposition (PECVD). This oxide layer was used as a hard mask in silicon etching. The waveguide structure was patterned using standard photolithography and the pattern was dry etched into the hard mask. Then the structure was etched into SOI using inductively coupled plasma (ICP). The ICP etching process was started with a long etch step with continuous passivation. Then the etching continued with alternating passivation and etching steps (etching gas SF_6, passivation gas C_4F_8). This was done to ensure side-wall verticality. The durations of the etching and passivation cycles were both 5 s. After removal of the resist and the passivation polymers in oxygen plasma, the oxide mask was removed by wet etching in buffered hydrofluoric acid. A scanning electron microscope (SEM) image of a cleaved test waveguide endface after ICP etching and mask removal is shown in Fig. 3. It clearly shows the high verticality and smoothness of the etched side-walls.

After the ridge waveguide fabrication an approximately 1 μm thick thermal oxide (TOX) was grown on top of the waveguide. This oxide served as an upper cladding for the waveguide, insulating the waveguide optically from the

heating elements. Thermal oxidation also reduced any surface roughness that might be present on the waveguide surface after ICP etching, and thinned the SOI layer down to 9 μm. A 500 nm thick Al layer was sputter deposited. It was patterned using standard photolithography and dry etching to form the heaters and their contact pads. After the dicing and the polishing the optical chips were glued on top of supporting plates with thermally conducting glue. Then the contact pads were wire bonded to provide the necessary electrical contacts and the chips were ready for the measurements.

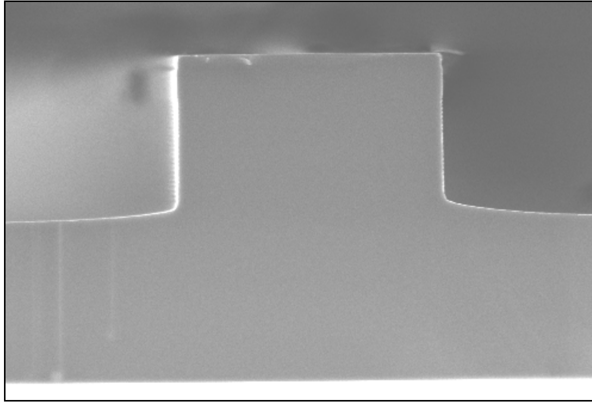

Figure 3: SEM image of an SOI waveguide cross-section after the ICP etching. The total height H, etch step H-h and width W of the waveguide are approximately 9 μm, 4.3 μm and 8 μm, respectively. These are similar, but not exactly the same dimensions as in the switch.

5. NEW MODULATION PRINCIPLE

Traditional modulation is based on turning the heating power simply on and off. In some cases bias voltages are used to stabilize the power consumption or to optimize the off-state of a nonideal switching structure. However, there are only two different heating states in traditional modulation. The advantage of this method is simple control electronics, but the exponential stabilization ($\Delta T = \Delta T_{\infty} (1-e^{-t/\tau}))$ of the temperature difference seriously limits the attainable frequency. The purpose of the new modulation principle is to remove this limit by optimizing the time-dependent heating powers in both waveguide branches. The principle is mainly focused on binary switching operation, but it may also be applicable for analog switch control.

In the new modulation principle the switching operation is divided into four different spans (time intervals) that each correspond to a single transition between two successive control bits. The spans are the on-span (binary 1→1), the fall-span (1→0), the off-span (0→0), and the rise-span (0→1). The heating power patterns in both waveguide branches (P_1, P_2) are optimized separately within each span, as illustrated schematically in Fig. 4. The duration of each span is the same as the duration of one control bit, but the selection of the span is based on two bits, instead of one.

The control powers are optimized according to the following logic. The static on-span remains unchanged compared to the traditional modulation ($P_1 = P_{on}$, $P_2 = 0$, $\Delta\phi = 180°$). The static off-span, on the other hand, is biased so that both waveguide branches are heated with approximately equal power ($P_2 \approx P_1 = P_{bias}$, $\Delta\phi = 0°$). This increases the average power consumption, but it also radically increases the switching speed, as will be shown below. Both the off- and the on-spans are static with respect to time, so that the switching state may remain stable for long periods of time (e.g. for binary ...111111111111...). During the rise-span, P_1 forms a high power peak, while P_2 drops from P_{bias} to zero. The

resulting temperature difference is a sum of the heating of the first waveguide and the cooling of the second waveguide. This generates a very fast rise time for the phase difference ($\Delta\phi$ = 0° →180°) between the waveguides. The fine structure of P_1 is optimized so that the phase difference reaches and maintains the allowed phase range as soon as possible. Similarly, during the fall-span P_1 drops from P_{on} to zero, while P_2 forms a high power peak. Therefore, while the first branch cools down, the second branch heats up, until the temperatures meet ($\Delta\phi$ = 180°→0°). Then both branches cool down, while maintaining the phase difference ($\Delta\phi \approx$ 0°) within an allowed range. If the switching is optimized for a given frequency f, then the operational frequency can be easily reduced by inserting additional on- and off-type delays between all the spans. It should also be noted that the modulation frequency corresponds to two spans, not one.

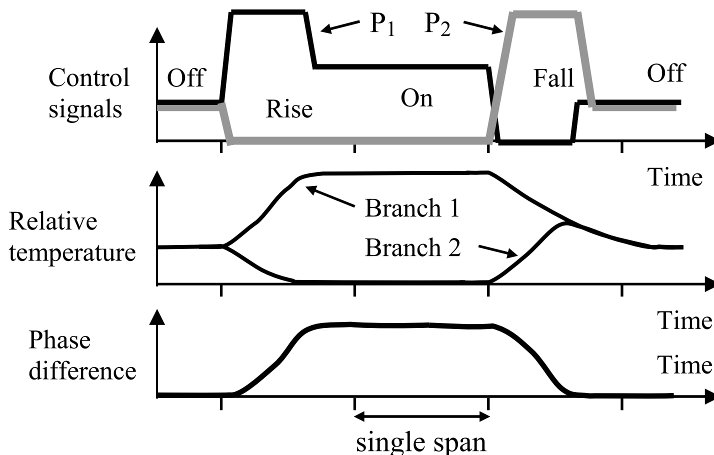

Figure 4: Schematic of the novel modulation principle.

The main advantage of the proposed principle is that the exponential temperature stabilization does not limit the operation and the maximum frequency can be radically increased. The increased complexity in the control electronics is not a serious problem if some kind of simple control electronics is anyway used to control the switch. With suitable software the optimization is not very difficult and fine tuning between similar devices can be carried out very fast.

6 RESULTS

The fabricated waveguides and waveguide switches were characterized optically by directly butt-coupling a polarization maintaining fiber (PMF) to the input end and a multi-moded fiber (MMF) to the output end of each waveguide. The MMF was connected to a fast photodetector. One axis of the PMF was carefully aligned parallel to the chip surface, i.e. horizontally. This ensures that the polarization states of the input fiber are coupled directly to the polarization states of the waveguide with minimum cross-talk (below -25 dB). Input power from a 1550 nm laser was then coupled very accurately to either polarization axis of the PMF and a transmission maximum from the PMF to the MMF was located by iteratively aligning both the input and the output fiber with respect to the waveguide.

6.1 Results without modulation

Before carrying out the switching measurements, the waveguides, switches and some separate directional couplers were characterized without heating them. This showed that the waveguides were single-moded and that the couplers were strongly polarization dependent. The latter is due to the thermal oxide cladding that induces a stress distribution into the

silicon core. The waveguides and couplers maintain the polarization state with an extinction ratio better than 15 dB, so they could be used to realize polarization maintaining or polarizing devices. However, for the majority of applications, the devices should be polarization independent. Such SOI ridge waveguides have indeed been realized[7], so the switches reported here could be made polarization independent by optimizing the fabrication process. All the following results are obtained with TE polarized input light (electric field along the substrate plane).

Preliminary characterization also revealed that even the best switch had slightly non-ideal DC lengths. This is not surprising, since the coupler length was varied only coarsely, as already discussed in Chapter 3. The best switch was chosen for the switching experiments and it had a maximum extinction ratio (ER) of 17 dB (98:2). During the phase modulation (switching), this is an optimum value that represents 100% phase modulation ($\Delta\phi = N\times180°$).

6.2 Results with traditional modulation

The switch was first tested by using traditional modulation with a square wave signal generator. The heating power P in the active (heated) waveguide branch was adjusted so that the on-state was optimized for very slow modulation ($f \ll 1$ kHz, $P = P_{on}$, $\Delta\phi = 180°$). The power consumption in the on-state was $P_{on} \approx 300$ mW. The transmission and the extinction ratio were found to be the same for both the bar and the cross-state of the switch with slow modulation. Therefore, the following measurements were carried out by measuring only the cross-path transmission through the switch. Optimized heating with very slow modulation determined the limits for the attainable transmission variation. The maximum frequencies for square wave modulation were determined by requiring a maximum of 1% deviation from the target transmission in both switching states. This is a very strict requirement and in an ideal switch structure it would correspond to an output extinction ratio of 20 dB. Due to the nonideal directional couplers, it only corresponds to 15 dB (97:3) extinction ratio in these measurements.

The maximum frequency for square wave modulation was found to be approximately 10 kHz. The measured result is shown in Fig. 5. Much faster modulation was obtained with extinction ratios smaller than 15 dB (e.g. 100 kHz for 3dB modulation). Both the maximum frequency and the power consumption were somewhat higher than the simulated values. This is probably due to the differences in boundary conditions.

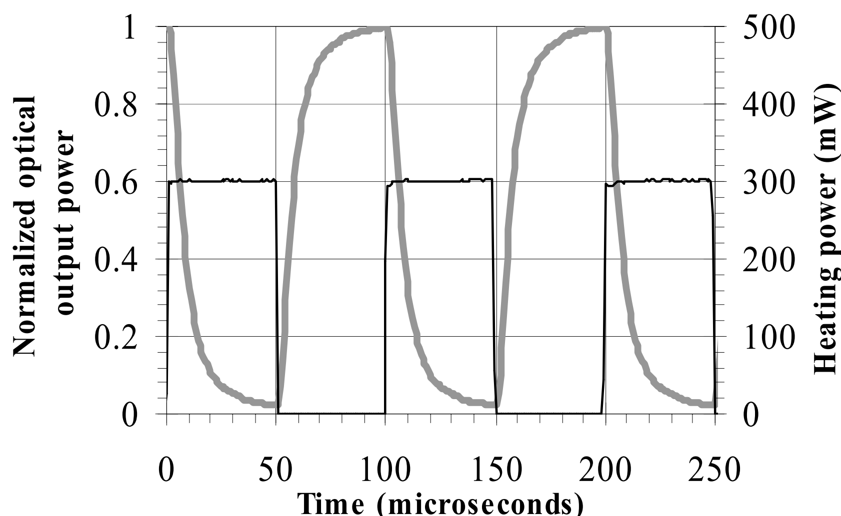

Figure 5: Normalized optical output power (thick gray line) for the cross-path through the thermo-optical switch and a control signal for the heating (black line) as a function of time at 10 kHz modulation. Deviation from the optimum (static) transmission minimum and maximum is below 1%.

6.3 Results with the new modulation principle

The proposed modulation principle was tested by applying it to the thermo-optical SOI waveguide switch described above. The control electronics was built from basic electronic components, and software was developed to control the system. The control circuit for one heating resistor consisted of one 16F84 microprocessor connected to an 8-bit digital to analog converter (DAC) made from an operation amplifier and a resistor network. The DAC's output was connected to the heating resistor via a power transistor to provide sufficient output current. For operating both branches of the switch, two of these circuits were built. The total cost of electronics was less than $25, the two microprocessors being the most expensive parts. The desired voltage patterns were generated by the software and sent via the computer's parallel port to the microprocessors' input ports. After receiving the complete patterns the processors started to repeat them until new patterns were transmitted.

The fall- and the rise-spans were optimized by adjusting P_1 and P_2 in 1 μs time steps. Shorter time steps would ease the optimization at high frequencies, but the used control electronics could not handle any shorter steps. Already at 1 μs steps the DAC strongly distorts fast voltage transients and generates sharp voltage peaks. Each span should include at least three time steps for any meaningful optimization, so the maximum frequency with 1 μs time steps is $f_{max} = (2 \cdot 3\ \mu s)^{-1} = 167$ kHz. Due to the simple and inexpensive electronics, the voltage patterns had very non-ideal shapes, but the feasibility of the new modulation principle could still be demonstrated, as will be shown below.

After appropriate optimization, $\Delta\phi$ could be changed between 0° and 180° in less than 3 μs, as can be seen from the optical response shown in Fig. 6. With square wave modulation the 15 dB extinction ratio was still achieved at the 167 kHz frequency that corresponds to 3 μs long spans and, thus, the limits of the control electronics. If a much lower extinction ratio would be accepted, such as 3 dB, then the maximum frequency could probably be rised close to the MHz regime. Unfortunately, the available control electronics was not sufficiently fast for such tests. The modulation at 167 kHz was tested with various different bit sequences, including back and forth transitions, as well as long chains of successive ones or zeros. The internal structure of each span remained constant in these experiments. For all bit sequences the extinction ratio remained above 13 dB (95:5). An example of the optical response with respect to a bit sequence at 167 kHz is shown in Fig. 6.

At 167 kHz operation the average total heating powers (including both branches) during the off-, on-, fall-, and rise-spans were 120 mW, 350 mW, 760 mW, and 1130 mW, respectively. With respect to square wave modulation, the power consumption is increased due to the high power peaks that correspond to changes in the switching state (rise- and fall-spans). In random modulation all spans are equally popular and the average heating power becomes 590 mW and in ultra-slow (...000001111111...) modulation the average heating power drops to 230 mW. Square-wave (...01010101...) modulation produces a worst-case average power of 950 mW. Relatively high peak powers are necessary for high frequency modulation, but because of the unoptimized electronics they became unnecessarily high in these measurements.

Any frequency between 10 kHz and 167 kHz can be obtained by optimizing the fall- and rise-spans with respect to the power consumption and the required minimum extinction ratio. When certain basic frequencies have been optimized, one can obtain the intermediate frequencies simply by inserting additional delays between the spans. This allows for rapid frequency fine tuning. Some sample frequencies were optimized to estimate the dependence of average heating power on the frequency. In this experiment, square wave modulation was used and a 15 dB extinction ratio was required for both switching states. The on- and off-spans again corresponded to static operation and single rise- and fall-spans were required to produce a stable output state (no overdriving). Table 1 summarizes the results at various frequencies between 10 kHz at 167 MHz. The average power consumption with random modulation was found to vary approximately linearly with respect to the frequency f, and an estimation for the power can be obtained from the formula $P_{ave} \approx 116\ \text{mW} + f \cdot 2.8\ \text{mW/kHz}$.

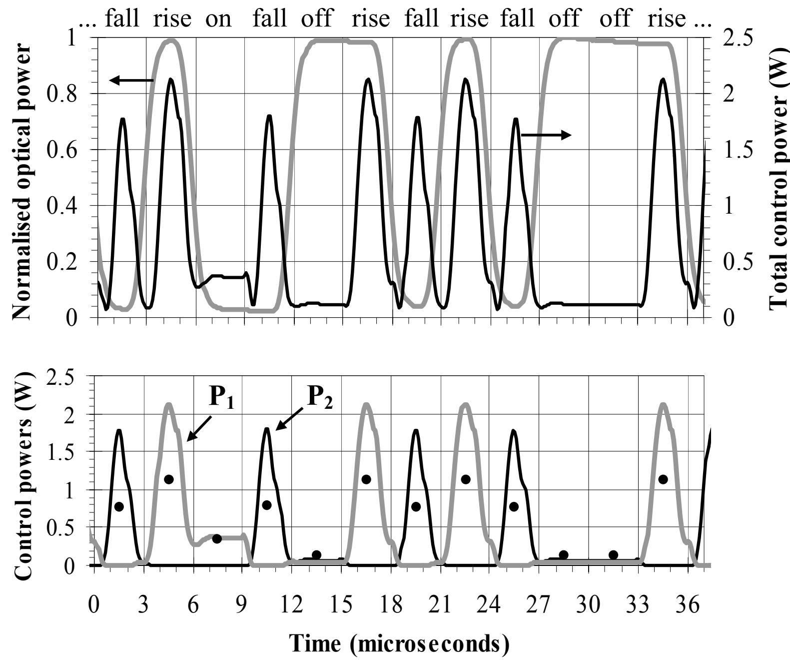

Figure 6: Measured switching at 167 kHz (3 μs/bit). Upper plot: Optical response (cross-path output) and total heating power. Lower plot: heating powers P_1, P_2, and the average heating power for each span (black dots). Optical signal has a 2 μs delay with respect to the heating power (span labels on top refer to the heating pulses).

Table 1: Summary of square wave switching characteristics at various frequencies by using the traditional modulation (10 kHz) and the novel modulation. A maximum of 1% deviation was required with respect to the attainable response range that was limited by the physical switch structure (nonideal coupler lengths). A fixed off-state (bias) is assumed, except for the 10 kHz modulation (no bias).

Case	Span length (μs)	Frequency (kHz)	Average power 1[1] *(random)* (mW)	Average power 2[2] *(worst-case)* (mW)	Average power 3[3] *(slow)* (mW)	Average power 4[4] *(lin. fit)* (mW)	Peak power (mW)
1[5]	50.0	10.0	150	150	150	144	300
2	6.3	79.4	331	427	235	338	608
3	5.3	94.4	371	506	235	380	787
4	4.3	116.0	436	638	235	441	1352
5	3.3	151.6	528	822	235	540	1848
6	3.0	167.0	590	945	235	584	2180

[1] With random modulation.
[2] With back and forth modulation (...10101010101...).
[3] With ultra-slow modulation (...00000111111...).
[4] Estimation based on the linear fit of random modulation.
[5] With traditional square wave modulation (...10101010101...).

7. CONCLUSIONS

By using a simple and inexpensive 2x2 MZI switch based on SOI technology, traditional TO modulation at 10 kHz frequency was obtained with 150 mW average power consumption. With a novel modulation principle the modulation

frequency was then pushed up to 167 kHz. The extinction ratio still remained at 15 dB for square wave modulation and it was 13 dB for random binary modulation. The extinction ratio is limited below 17 dB due to the nonideal coupler lengths, so the measured extinction ratios deviate only 1-3% from the attainable limits. The average power consumption with random modulation was 590 mW at 167 kHz. We expect that a reduction of the core size, optimization of the thermal insulation, improved electronics and less strict extinction ratio requirements can improve the frequency to power ratio and increase the frequency to the MHz range. The results indicate potential in realizing inexpensive thermo-optical switches in the 1-1000 kHz frequency range by using SOI technology. The very successful first testing of the proposed new modulation principle also encourages further testing with other interferometric switch structures. The basic principle could be used to speed up many existing switches in many different frequency ranges.

ACKNOWLEDGEMENTS

Mikko Harjanne, Markku Rönö, Mikko Söderlund, and Joona Koponen are acknowledged for their valuable contribution to the work.

REFERENCES

1. G. Cocorullo, M. Iodice, I. Rendina, and M. Sarro, "Silicon thermooptical micromodulator with 700-kHz, –3-dB bandwidth", *IEEE Photon. Technol. Lett.* **7**, pp. 363-365, 1995.
2. U. Fischer, T. Zinke, B. Schüppert, and K. Petermann, "Singlemode optical switches based on SOI with large cross-section" Electron. Lett., 30 (1994), 406-408.
3. S. A. Clark, B. Culshaw, E. J. C. Dawnay, and I. E. Day, "Thermo-optic phase modulators in SIMOX material", *Proc. SPIE* **3936**, pp. 16-24, 2000.
4. B. Jalali, "Silicon-on-insulator photonic integrated circuit (SOI-PIC) technology", *SPIE Proc.* **2997**, pp. 60-71, 1997.
5. T. Zinke, U. Fischer, B. Schüppert, K. Peterman, "Theoretical and experimental investigation of optical couplers in SOI", *Proc. SPIE* **3007**, pp. 30-39, 1997.
6. T. Aalto, S. Yliniemi, P. Heimala, P. Pekko, J. Simonen, M. Kuittinen, "Integrated Bragg gratings in silicon-on-insulator waveguides", *Proc. SPIE* **4640**, pp. 117-124, 2002.
7. P. D. Trinh, S. Yegnanarayanan, F. Coppinger, B. Jalali, "Silicon-on-insulator (SOI) phased-array wavelength multi/demultipelexer with extremely low-polarization sensitivity", *IEEE Photon. Technol. Lett.* **9**, pp. 940-942, 1997.
8. A. Himeno, K. Kato, and T. Miya, "Silica-based planar lightwave circuits", *IEEE J. Sel. Topics in Quantum Electron.* **4**, pp. 913-924, 1998.
9. H. Nishihara, M. Haruna, and T. Suhara, *Optical IntegratedCircuits*, McGraw-Hill, New York, 1989.
10. T. Aalto, P. Heimala, P. Katila, "Integrated optical switch based on SOI-technology", *Physica Scripta* **T79**, p. 123-126, 1999.
11. R. A. Soref, J. Schmidtchen, K. Petermann, "Large single-mode rib waveguides in GeSi-Si and Si-on-SiO_2", *IEEE J. Quantum Electron.* **27**, pp. 1971-1974, 1991.

PUBLICATION V

Sub-μs Switching Time in Silicon-on-Insulator Mach–Zehnder Thermooptic Switch

© 2004 IEEE. Reprinted, with permission, from *Photonics Technology Letters*, Vol. 16, No. 9, pp. 2039–2041, 2004.

Sub-μs Switching Time in Silicon-on-Insulator Mach–Zehnder Thermooptic Switch

Mikko Harjanne, Markku Kapulainen, Timo Aalto, and Päivi Heimala

***Abstract*—We have demonstrated both rise and fall times below 1 μs with 10%–90% modulation in a silicon-on-insulator thermooptical Mach–Zehnder switch. The switch is based on 9-μm-thick and 10-μm-wide single-mode rib waveguides. Very fast switching was achieved by using a differential control method. The switch was driven with a digital signal processor accompanied by simple electronic circuitry.**

***Index Terms*—Integrated optics, optical switches, optical waveguides, silicon-on-insulator (SOI) technology, thermooptic (TO) effects.**

I. INTRODUCTION

SILICON-ON-INSULATOR (SOI) waveguides are very promising for realizing dense photonic integrated circuits [1]. The transparency of silicon in the infrared spectral region is very high. A typical SOI waveguide has a silicon core (refractive index $n = 3.5$) surrounded by a cladding oxide, with n less than two. Therefore, the silicon core has a very high index difference with respect to the cladding, which strongly confines the electric field into the silicon layer. This means that cladding oxide layers can be made relatively thin (<1 μm) when compared, e.g., with silica-on-silicon waveguides where the required cladding oxide thickness is typically over 10 μm. SOI waveguide technology is compatible with electrical integrated circuit technology and micromechanics.

Despite the large refractive index difference, the silicon waveguide can be made single-moded even with large waveguide dimensions using a rib structure [2]. This makes SOI waveguide technology compatible with fiber-based telecommunication and interconnection devices. Large SOI waveguides have been used to demonstrate, e.g., optical couplers [3], wavelength multiplexers [4], and waveguide gratings [5], [6].

Fast modulators based on free-carrier dispersion and absorption effects have been demonstrated in silicon. Modulation frequencies as high as 1 GHz have recently been demonstrated [7]. Drawbacks of free-carrier effects are higher manufacturing costs and losses in optical switching. An alternative, particularly for low-loss, low-cost, and low-frequency applications, is to use the thermooptic (TO) effect for optical switching or modulation. SOI technology offers a relatively inexpensive method to fabricate TO switches. The high thermooptical constant ($1.86 \cdot 10^{-4}\mathrm{K}^{-1}$) and good thermal conductivity of silicon can make SOI switches faster than most other TO switches.

Manuscript received April 21, 2004; revised May 17, 2004.

M. Harjanne is with Helsinki University of Technology, Espoo FIN-02015, Finland (e-mail: Mikko.Harjanne@vtt.fi).

M. Kapulainen, T. Aalto, and P. Heimala are with VTT Information Technology Microelectronics, Espoo FIN-02044, Finland.

Digital Object Identifier 10.1109/LPT.2004.833896

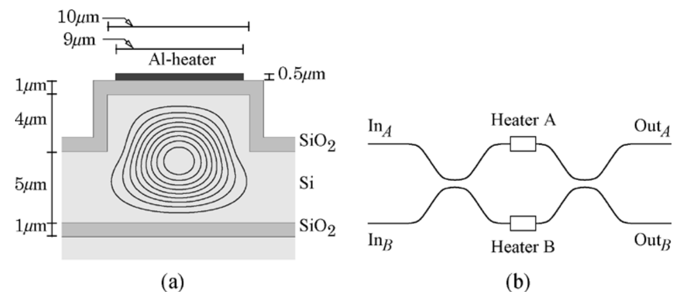

Fig. 1. (a) Cross section of the processed rib waveguide with structure dimensions. Field intensity contours are equispaced and run from 10% to 90%. (b) Schematic structure of the MZI used for measurements.

In this work, a TO switch has been realized based on SOI rib waveguides. Switching time below 1 μs was achieved by using a differential modulation technique [8].

II. SWITCH

The fast switching scheme was demonstrated with an existing 2×2 TO Mach–Zehnder interferometer (MZI) switch. Detailed information of the design and fabrication process of the switch is published in [8]. The switch is constructed of 9-μm-thick SOI rib waveguides with rib width of 10 μm and etch depth of 4 μm, as illustrated in Fig. 1(a). The buried oxide layer and the thermal oxide (TOX) cladding layer were both 1 μm thick. These waveguides have good coupling to standard single-mode fibers, and are also single-moded according to theory [2], computer simulations [9], and measurements.

The MZI switch structure is presented in Fig. 1(b). A TO-MZI consists of two identical 3-dB couplers and a heating resistor in one or both optical branches. The heaters are used to change the index of refraction, and hence, cause a phase difference $\Delta\varphi$ between the two optical branches. When branches have equal optical lengths, that is $\Delta\varphi = 0$, the switch is in a cross state. In this case, signal at input A comes out from output B and vice versa.

With a certain temperature difference, $\Delta\varphi = \pi$ between the branches, and the switch is in a bar state, so that signal at input A is seen at output A. The amount of heat required for this depends on several factors such as heater and waveguide dimensions, as well as thermal conductivities of materials.

In our implementation, both optical branches are equipped with 1-mm-long heating resistors having electrical resistance of approximately 9 Ω. The two 3-dB couplers were found to have nonideal coupling lengths, which led to a maximum of 15-dB power extinction ratio (ER). The fact that the maximum ER was obtained when heating was OFF suggests that the couplers are

1041-1135/04$20.00 © 2004 IEEE

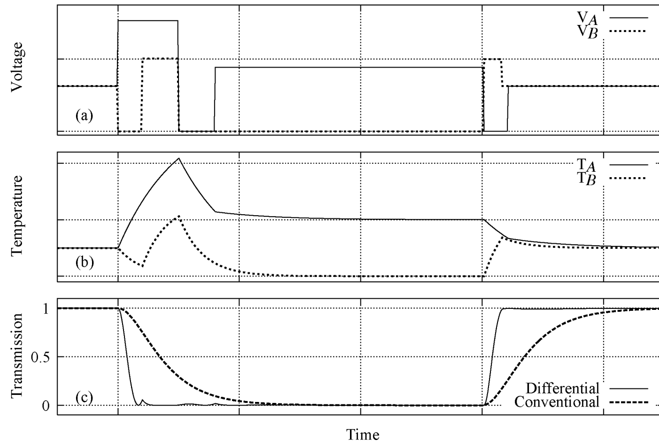

Fig. 2. Differential control method. (a) Control voltages for the two heaters A and B. (b) The resulting waveguide temperatures. (c) Optical power transmission to cross port with the differential (solid) and conventional control (dashed).

identical, and the optical power measured from the cross port is related to $\Delta\varphi$ as

$$P_X \sim \frac{1}{2}\left(1 + cos(\Delta\varphi)\right). \qquad (1)$$

The switch is somewhat polarization-dependent due to the stress induced by the TOX cladding. This polarization dependency can be lowered by using a tetraethylorthosilicate layer instead of TOX [9].

III. Control Method

In a TO MZI switch, the phase difference required for operating the switch is induced by heating the waveguide with a thin-film heater. The conventional way is not to apply any heating when the switch is in the cross state, and to use a constant heating voltage when switch is changed to the bar state. This leads to an exponential temperature stabilization during both state changes, which limits the achievable switching time.

When using an MZI-structure having heaters at both branches, such as in Fig. 1(b), switching times can be significantly reduced by driving both heaters simultaneously with different signals [8]. Fig. 2 shows the basic principle of this switching method.

A bias heating, equal in both branches, can optionally be used during the cross state to reduce the cooling time when switching from bar to cross state. The biasing adds the power consumption of the device, but this drawback is usually compensated by the shortened switching time.

To have a fast temperature change, a high voltage pulse is applied to heater A, and heater B voltage is dropped to zero. If there would be no further action, $\Delta\varphi$ would go over π, but by applying a smaller corrective pulse to heater B at exactly the same time as $\Delta\varphi = \pi$, the overshoot can be compensated. This leads to a stepwise optical response and leaves both waveguides above their target temperatures. However, the heaters cool down together along exponential curves, keeping $\Delta\varphi$ essentially the same. If the two waveguide branches cool down at different rates, some fine-tuning can be added to the heater voltages in order to keep $\Delta\varphi$ at π during the cooling period.

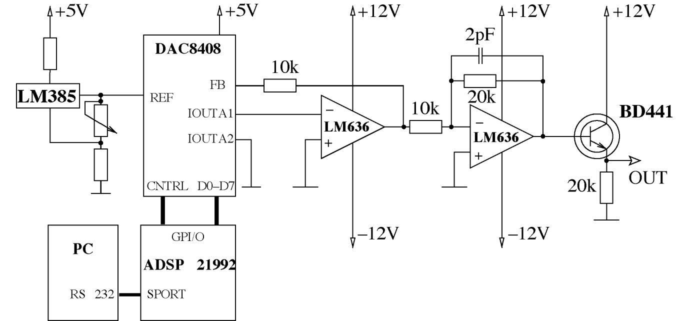

Fig. 3. Schematic representation of the control circuit.

The change from bar to cross state is handled similarly; a high-voltage pulse is applied to heater B and at the same time voltage at heater A is set to zero. When the branch temperatures coincide, both heaters are set to their cross state bias voltages. Again, some fine-tuning of voltages may be needed to compensate different cooling rates.

The temperature curves in Fig. 2(b) were calculated from the heater voltages in Fig. 2(a) by difference equation

$$T_n = T_{n-1} - \frac{(T_{n-1} - V_n K)}{\tau \Delta t} \qquad (2)$$

where V_n is heater voltage during the nth time step, K is the experimentally determined relation between voltage and temperature, Δt is the time-step length, and τ is the temperature time constant which can be different for cooling and heating, as well as for the two branches. As the phase is linearly dependent on temperature, the cross port transmissions, shown in Fig. 2(c), could be calculated from the temperatures by using (1).

IV. Measurement Setup

To demonstrate the feasibility of the differential control method, a controller shown in Fig. 3 was constructed. The heating patterns were designed on a personal computer, and these were then sent to the memory of a digital signal processor (ADSP-21 992) via serial cable. The processor was programmed to send the data as fast as possible to an 8-bit digital-to-analog (D/A) converter (DAC 8408). The low-level output of the converter was amplified with operational amplifiers to a range of 0–6.5 V, and then buffered by high-power transistors. This setup could generate 330-ns voltage pulses with a slew rate of 16 V/μs.

The processor in the setup is capable of receiving new patterns from the computer at the same time as it repeatedly sends the previous pattern to the D/A converter. This allowed for a near real-time observations of switch operation when changes were made to the heating pattern.

All measurements were made at 1550-nm wavelength with transverse-electric-polarized light. The laser light was butt-coupled to the waveguide with a polarization maintaining fiber. Power at the output was gathered from the cross-state port with a multimode fiber, and measured with a fast 15-MHz detector.

Optical power extrema were measured by letting $\Delta\varphi$ go below zero and over π at some point during one state change. The measured power was then normalized to this range, so that the nonideal switch structure would not affect the measurement of the switch state.

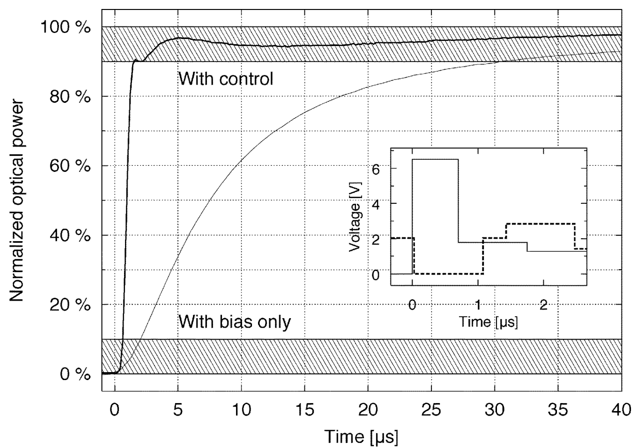

Fig. 4. Cross port signal rise times (change from bar to cross), both with differential heating and when using only bias. Rise times (10%–90%) are 725 ns and 29.2 μs, respectively. The heating patterns are shown in inset.

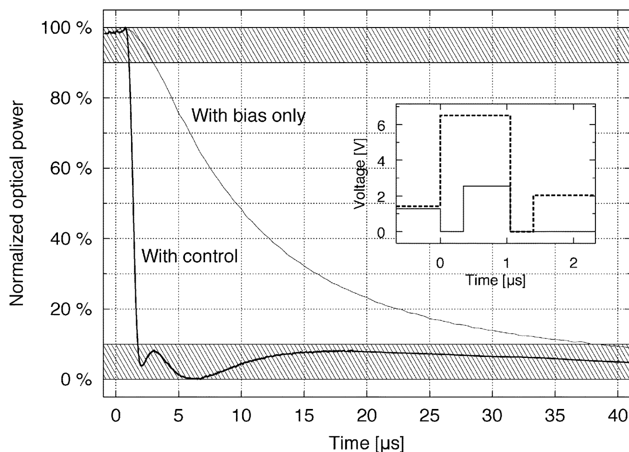

Fig. 5. Cross port signal fall times (change from cross to bar), both with differential heating and when using only bias. Fall times (90%–10%) are for differential control 700 ns and for biased control 35.0 μs.

V. Measurement Results

The proposed method was used to optimize single rise and fall times for the switch. Transition times between 10% and 90% of the achievable power extremes were used as the only optimization criteria, i.e., the power consumption and the power variations below 10% and above 90% were not considered. The optimal heating patterns are shown in Figs. 4 for rise time and 5 for fall time, together with the normalized optical signals obtained with the differential control method. For comparison, normalized optical signals obtained by driving the switch with conventional step-wise control signal also implementing bias are shown in the Figs. 4 and 5.

As seen from Figs. 4 and 5, the differential control method enabled the rise and fall times to be suppressed from 29.2 and 35.0 μs to 725 and 700 ns, i.e., by a factor of over 40 in both cases. The power variations above 90% and below 10% after the rise and fall times are due to the different temperature settling times and the minimum time step of 330 ns allowed by the control electronics, which prohibits the precise timing of the compensation pulse. When compared to the step-wise biased control, the differential control adds the energy consumption by 4.8 and 5.8 μJ for rise and fall times, respectively. For continuous 1- and 10-kHz switching speed, this corresponds to a change in power consumption from 250 mW of the conventional switching to 260 and 360 mW, respectively.

The characteristic behavior of the measurement results with and without the differential control method is in good agreement with that depicted in Section III.

VI. Conclusion

We have achieved rise and fall times of 725 and 700 ns, respectively, with 10%–90% modulation, in an MZI TO-switch with 9-μm-thick rib waveguides by applying a differential temperature control. Switching times were reduced by a factor of over 40 when compared to conventional switching.

With the differential control, the switching speed increase can be freely selected by using appropriately high heating voltages. The switching speed is limited by the heater breakdown point, the speed of controller circuit, and the possible channel temperature heat build-up.

The switch controller used in the demonstration is more complex than is needed in an actual component. With SOI waveguides, the required electronics could well be monolithically integrated with the optical switch, so that the differential control would be totally transparent to the end user.

The proposed method can be used to speed up also other interferometry-based components, providing that both interferometer branches are controllable, and that the switching speed is mainly limited by the speed of the optical effect used.

References

[1] B. Jalali, "Silicon-on-insulator photonic integrated circuit (SOI-PIC) technology," *Proc. SPIE*, vol. 2997, pp. 60–71, 1997.

[2] R. A. Soref, J. Schmidtchen, and K. Petermann, "Large single-mode rib waveguides in GeSi-Si and Si-on-SiO_2," *J. Quantum Electron.*, vol. 27, no. 8, pp. 1971–1974, 1991.

[3] T. Zinke, U. Fischer, B. Schüppert, and K. Peterman, "Theoretical and experimental investigation of optical couplers in SOI," *Proc. SPIE*, vol. 3007, pp. 30–39, 1997.

[4] P. D. Trinh, S. Yegnanarayanan, F. Coppinger, and B. Jalali, "Silicon-on-insulator (SOI) phased-array wavelength multi/demultipelexer with extremely low-polarization sensitivity," *IEEE Photon. Technol. Lett.*, vol. 9, pp. 940–942, July 1997.

[5] T. Aalto, S. Yliniemi, P. Heimala, P. Pekko, J. Simonen, and M. Kuittinen, "Integrated Bragg gratings in silicon-on-insulator waveguides," *Proc. SPIE*, vol. 4640, pp. 117–124, 2002.

[6] A. Cutolo, M. Iodice, A. Irace, P. Spirito, and L. Zeni, "An electrically controlled Bragg reflector integrated in a rib silicon on insulator waveguide," *Appl. Phys. Lett.*, vol. 71, pp. 199–201, 1997.

[7] A. Liu, R. Jones, L. Liao, D. Samara-Rubio, D. Rubin, O. Cohen, R. Nicolaescu, and M. Paniccia, "A high-speed silicon optical modulator based on a metal-oxide-semiconductor capacitor," *Nature*, vol. 427, pp. 615–618, 2004.

[8] T. Aalto, M. Kapulainen, S. Yliniemi, P. Heimala, and M. Leppihalme, "Fast thermo-optical switch based on SOI waveguides," *Proc. SPIE*, vol. 4987, pp. 149–159, 2003.

[9] T. Aalto, M. Harjanne, M. Kapulainen, P. Heimala, and M. Leppihalme, "Development of silicon-on-insulator waveguide technology," *Proc. SPIE*, vol. 5355, pp. 81–95, 2004.

PUBLICATION VI

Efficient Bragg waveguide-grating analysis by quasi-rigorous approach based on Redheffer's star product

In: *Optics Communications*, Vol. 198, pp. 265–272, 2001.
© 2001, Elsevier.
Reprinted with permission from the publisher.

ELSEVIER

1 November 2001

Optics Communications 198 (2001) 265–272

OPTICS COMMUNICATIONS

www.elsevier.com/locate/optcom

Efficient Bragg waveguide-grating analysis by quasi-rigorous approach based on Redheffer's star product

Jani Tervo [a], Markku Kuittinen [a,*], Pasi Vahimaa [a], Jari Turunen [a], Timo Aalto [b], Päivi Heimala [b], Matti Leppihalme [b]

[a] *Vaisala Laboratory, Department of Physics, University of Joensuu, P.O. Box 111, FIN-80101 Joensuu, Finland*

[b] *VTT Electronics, Microelectronics, P.O. Box 1101, FIN-02044 VTT, Finland*

Received 31 May 2001; accepted 28 August 2001

Abstract

We introduce a computationally efficient quasi-rigorous method for the analysis of corrugated planar waveguide structures. The method is based on rigorous diffraction theory of gratings. The computational efficiency is achieved by using Redheffer's star product and the so-called binary method for the involution of the transfer matrix. The developed method enables efficient rigorous analysis of corrugated waveguide structures without any limitations for the corrugation depth. Comparison with the thin-film stack method shows that the proposed method gives similar results for Bragg grating for the fundamental mode when the corrugations are shallow, but the results differ significantly when the corrugations are deep. Furthermore, the quasi-rigorous method also facilities the analysis of the coupling of light from the fundamental mode into the higher waveguide modes. © 2001 Elsevier Science B.V. All rights reserved.

PACS: 42.82.E; 42.79.D; 02.70

Keywords: Waveguide gratings; Rigorous diffraction theory

1. Introduction

Bragg gratings are widely used in the rapidly growing field of optical telecommunications. In general, any perturbation formed as a periodic corrugation or refractive index modulation in an optical waveguide serves as a Bragg grating for some wavelength. Bragg gratings written in a photosensitive fibers as a periodic refractive index variation can be used to make a variety of devices such as filters, add/drop multiplexers, and dispersion compensators [1]. The advantage of the all-fiber devices is that they have low insertion losses. However, if cost efficiency, size reduction or separation of several wavelength channels is important, integrated optical Bragg gratings offer an attractive alternative. Silicon based waveguide technology eases mass production and enables monolithic integration of different gratings in almost arbitrary configurations. Especially in complex systems this eliminates many interconnections, thus reducing work load, costs, power losses, and size. Materials with high refractive index, such as silicon, allow to

* Corresponding author. Tel.: +358-13-251-2110; fax: +358-13-251-3290.

E-mail address: markku.kuittinen@joensuu.fi (M. Kuittinen).

0030-4018/01/$ - see front matter © 2001 Elsevier Science B.V. All rights reserved.

PII: S0030-4018(01)01530-9

realize integrated optical grating components that are smaller than their fiber equivalents. In addition, integrated Bragg gratings offer a couple of completely new possibilities. First, gratings can be fabricated as corrugated structures in materials, which are not photorefractive. Second, other optical devices (couplers etc.), and even electrical components (modulators, control circuits etc.), can be monolithically integrated with the gratings.

The propagation of optical modes in periodic corrugated waveguides can be analyzed accurately by using the Floquet–Bloch theory [2,3]. If the depth of the corrugated structure is much lower than the waveguide thickness, coupled-mode theory [4,5] is widely used for the analysis of waveguide gratings. Wang [6] proposed a simple effective-index/impedance matching technique for solving the mode-coupling problem. Later Verly et al. [7,8] derived the effective-index method for corrugated gratings directly from Maxwell's equations. The effective-index method is known to give results equivalent with coupled-mode theory for shallow surface corrugations [9]. Effective-index method is very similar to the methods used to study reflection and transmission of light from thin-film stack. This thin-film stack approach can be implemented in a computationally efficient form for waveguide gratings by using Rouard's method [10], which is a recursive method used in thin-film coating design. The basic idea of the Rouard's method is the replacement of a thin-film layer characterized by an effective complex reflectivity by a single interface having the same properties. In fact, thin-film stack method is a numerical method for solving the coupled-mode equations and it has shown to be in excellent agreement with the coupled-mode method [10,11]. Coppola et al. have presented analytic approach [12] for analysis of the effects of errors in grating period and shape as well as other fabrication errors, which is an extension of the coupled-mode theory. The idea of this analytic extension is to separate the response of the ideal grating and the response of the errors.

All the methods mentioned above are limited either by the assumption of infinite grating structure or by the small-perturbation (shallow structure) hypothesis. Recently, a rigorous method of bidirectional mode expansion and propagation (BEP) [13,14] has been extended for efficient modeling of periodic structures by implementation of the Floquet theorem [15,16]. The BEP method can be cast into a consistent implementation of the mode-matching method for waveguide structures with strongly corrugated Bragg gratings. Also, some finite-difference beam propagation methods have been applied to the analysis of waveguide gratings [17], but these methods are still computationally rather inefficient, especially if the waveguide grating contains a large number of periods.

In this paper we introduce a computationally efficient quasi-rigorous method for analyzing corrugated Bragg gratings. It has been developed for the simulation of silicon-on-insulator (SOI) waveguide gratings [18–20], but it is applicable to other grating structures as well. The method is based on rigorous diffraction theory of gratings [21] and it is described in detail in Section 2. The comparison between the introduced method and thin-film stack method is given in Section 3, where we also demonstrate that the thin-film stack method cannot predict the reflectance of Bragg gratings with strong corrugations. The new method can be applied also to the error analysis of Bragg gratings. Some results for regular, stitching-type errors are given in Section 3.

2. Computational model

Vahimaa and Turunen [22] introduced an idea on how to apply rigorous grating diffraction theory to the analysis of waveguide gratings (see also Ref. [23]). A similar method has been used by Lalanne and Silberstein [24]. This method is highly accurate but computationally inefficient because the transfer of fields through the structure must be calculated sequentially, period by period. In this paper we describe how the S-matrix transfer algorithm with the star product [25,26] can be applied to reduce the computational effort from $\sim N$ to $\sim \log_2 N$, where N is the number of grating periods.

Let us consider the three-dimensional structure illustrated in Fig. 1. We assume that the ridge waveguide is etched by an amount h so that $J/2$ identical periods, where J is an even integer, are

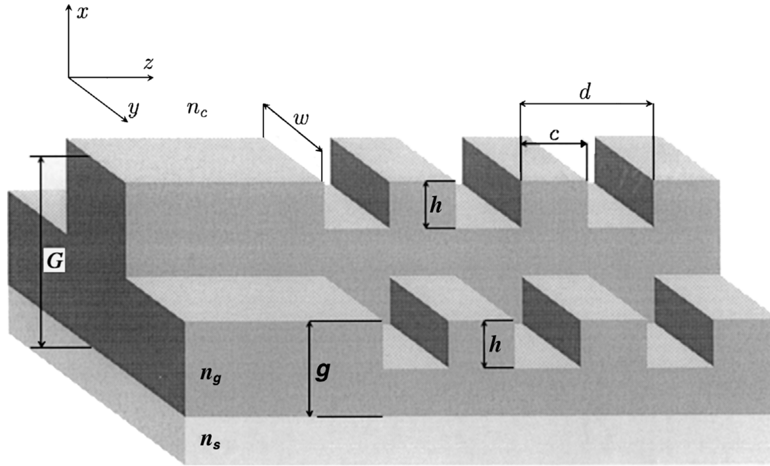

Fig. 1. Three-dimensional structure of an etched ridge-waveguide grating.

formed. If we assume that the constant width w of the guiding part is, at least, a few wavelengths, we may approximate this structure by a two-dimensional structure illustrated in Fig. 2, where n_{eff} is the effective refractive index of the ridge part calculated in the y-direction as described in Ref. [28]. In Fig. 2 we have already assumed that the structure is periodic, with period D, in the x-direction to make the use of the grating theory possible. To minimize the interaction between the fields in adjacent periods the artificial absorbers have to be added between the periods. The optimal selection for an absorber would be an optimized Bérenger layer [29], but in numerical simulations we noticed that Gaussian absorber, which does not require optimization, is sufficient. Moreover, the period D is assumed to be large enough to prevent the evanescent tails of the guided modes from interacting with the absorbers.

As explained in Ref. [21], the field expression in the jth layer in the case of TE-polarization is of the form

$$E_j(x,z) = \sum_{m=1}^{\infty} \left\{ a_m^j \exp\left[\mathrm{i}\gamma_m^j (z - z_j) \right] + b_m^j \exp\left[-\mathrm{i}\gamma_m^j (z - z_{j+1}) \right] \right\} X_m^j(x), \tag{1}$$

where a_m^j and b_m^j are the unknown amplitudes of the mth mode propagating in the positive and the negative z-directions, respectively, and γ_m^j are the propagation constants of the modes obtained by solving the eigenvalue equations as explained in Ref. [21]. Here the function $X_m^j(x)$ represents the transversal distribution of the mth mode. Applying the periodicity, $X_m^j(x)$ may be expanded as a Fourier series

$$X_m^j(x) = \sum_{q=-\infty}^{\infty} P_{mq}^j \exp(\mathrm{i}2\pi q x/D), \tag{2}$$

with the qth Fourier coefficient given by

$$P_{mq}^j = \frac{1}{D} \int_0^D X_m^j(x) \exp(-\mathrm{i}2\pi q x/D)\, \mathrm{d}x. \tag{3}$$

These coefficients P_{mq}^j are actually solved eigenvector coefficients from the eigenvalue problems, see Ref. [21]. In rigorous grating diffraction theory, the input and output regions are assumed to be homogeneous materials. However, in our model for waveguides both the input and output regions are periodically modulated, and the field expressions in these regions are similar to Eq. (1):

$$E_0(x,z) = \sum_{m=1}^{\infty} \left\{ a_m^0 \exp\left(\mathrm{i}\gamma_m^0 z \right) + b_m^0 \exp\left[-\mathrm{i}\gamma_m^0 (z - z_1) \right] \right\} X_m^0(x) \tag{4}$$

in the input region and

$$E_{J+1}(x,z) = \sum_{m=1}^{\infty} a_m^{J+1} \exp\left[\mathrm{i}\gamma_m^{J+1} (z - z_{J+1}) \right] X_m^{J+1}(x) \tag{5}$$

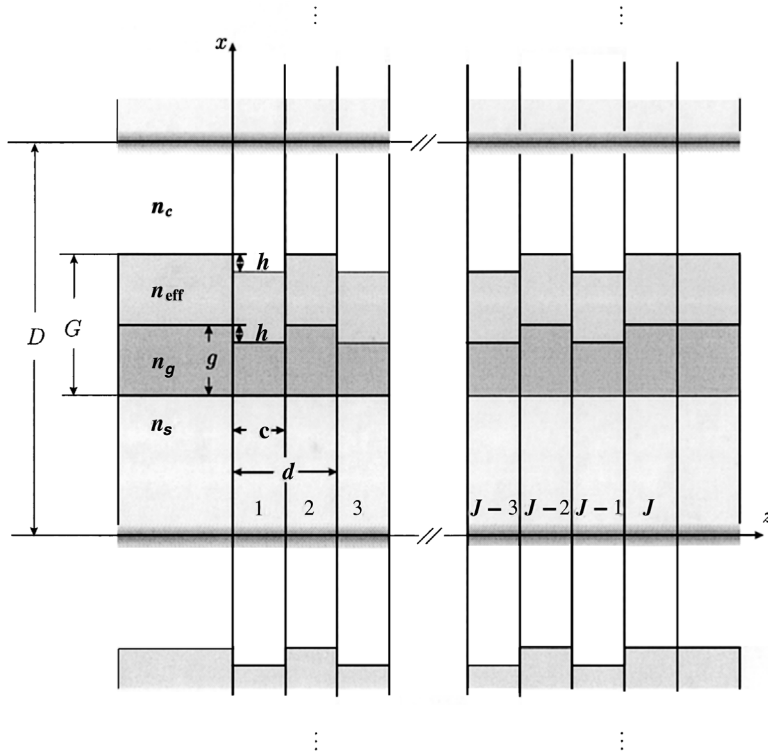

Fig. 2. Two-dimensional approximation of the geometry in Fig. 1.

in the output region. We note here that in Eq. (4) the first term in summation represents incoming field and the second term represents reflected field.

To solve the mode amplitudes a_m^j and b_m^j we use the requirement of the continuity of the electric field as well as its z-derivative at the boundary between the layers j and $j+1$, which yields

$$\begin{bmatrix} \boldsymbol{a}_{j+1} \\ \boldsymbol{b}_j \end{bmatrix} = \mathbf{S}_j \begin{bmatrix} \boldsymbol{a}_j \\ \boldsymbol{b}_{j+1} \end{bmatrix}, \tag{6}$$

where

$$\boldsymbol{S}_j = \begin{bmatrix} \mathbf{P}_{j+1} & -\mathbf{P}_j \\ \mathbf{P}_{j+1}\boldsymbol{\Gamma}_{j+1} & \mathbf{P}_j\boldsymbol{\Gamma}_j \end{bmatrix}^{-1} \begin{bmatrix} \mathbf{P}_j\mathbf{E}_j & -\mathbf{P}_{j+1}\mathbf{E}_{j+1} \\ \mathbf{P}_j\boldsymbol{\Gamma}_j\mathbf{E}_j & \mathbf{P}_{j+1}\boldsymbol{\Gamma}_{j+1}\mathbf{E}_{j+1} \end{bmatrix}. \tag{7}$$

The elements of the column vectors $\boldsymbol{a}_j$ and $\boldsymbol{b}_j$ are a_m^j and b_m^j, respectively. Here $\boldsymbol{\Gamma}_j$ and $\mathbf{E}_j$ are diagonal matrices with elements γ_m^j and $\exp[\mathrm{i}\gamma_m^j(z_{j+1} - z_j)]$, respectively, while the elements of the matrix $\mathbf{P}_j$ are defined in Eq. (3). Therefore, all the matrices $\mathbf{S}_j$ can be formed once the eigenvalue problem of each layer is solved. One should notice that Eq. (7) is valid also at $z = z_1$ and $z = z_{J+1}$. In the latter case, however, $\mathbf{b}_{J+1} = 0$.

If only the amplitudes $\boldsymbol{b}_0$ and $\boldsymbol{a}_{J+1}$ are of interest, one may combine the matrices $\mathbf{S}_j$ by using Redheffer's star product [30] as described by Li [26]:

$$\begin{bmatrix} \boldsymbol{a}_{J+1} \\ \boldsymbol{b}_0 \end{bmatrix} = \mathbf{S}_0 * \mathbf{S}_1 * \cdots * \mathbf{S}_J \begin{bmatrix} \boldsymbol{a}_0 \\ 0 \end{bmatrix}. \tag{8}$$

Here the star product for $2N \times 2N$ matrices $\mathbf{C}$ and $\mathbf{D}$ is defined as

$$\begin{aligned} \mathbf{C} * \mathbf{D} &= \begin{bmatrix} \mathbf{c}_{11} & \mathbf{c}_{12} \\ \mathbf{c}_{21} & \mathbf{c}_{22} \end{bmatrix} * \begin{bmatrix} \mathbf{d}_{11} & \mathbf{d}_{12} \\ \mathbf{d}_{21} & \mathbf{d}_{22} \end{bmatrix} \\ &= \begin{bmatrix} \mathbf{d}_{11}(\mathbf{I} - \mathbf{c}_{12}\mathbf{d}_{21})^{-1}\mathbf{c}_{11} & \mathbf{d}_{12} + \mathbf{d}_{11}\mathbf{c}_{12}(\mathbf{I} - \mathbf{d}_{21}\mathbf{c}_{12})^{-1}\mathbf{d}_{22} \\ \mathbf{c}_{21} + \mathbf{c}_{22}\mathbf{d}_{21}(\mathbf{I} - \mathbf{c}_{12}\mathbf{d}_{21})^{-1}\mathbf{c}_{11} & \mathbf{c}_{22}(\mathbf{I} - \mathbf{d}_{21}\mathbf{c}_{12})^{-1}\mathbf{d}_{22} \end{bmatrix}, \end{aligned} \tag{9}$$

where $\mathbf{c}_{mq}$ and $\mathbf{d}_{mq}$ are $N \times N$ submatrices and $\mathbf{I}$ is an unit matrix.

If the structure is periodic so that layers j and $j+2$ are identical, we have $\mathbf{S}_j = \mathbf{S}_{j+2}$ for $j = 1, 2, \ldots, J-3$. Using the associativity of the star product, we may express Eq. (8) as

$$\begin{bmatrix} \boldsymbol{a}_{J+1} \\ \boldsymbol{b}_0 \end{bmatrix} = \mathbf{S}_0 * [(\mathbf{S}_1 * \mathbf{S}_2) * \cdots * (\mathbf{S}_{J-3} * \mathbf{S}_{J-2})] * \mathbf{S}_{J-1} * \mathbf{S}_J \begin{bmatrix} \boldsymbol{a}_0 \\ 0 \end{bmatrix} \quad (10)$$

$$= \mathbf{S}_0 * \mathbf{Z}^{(J-2)/2} * \mathbf{S}_{J-1} * \mathbf{S}_J \begin{bmatrix} \boldsymbol{a}_0 \\ 0 \end{bmatrix}, \quad (11)$$

where $\mathbf{Z} = \mathbf{S}_1 * \mathbf{S}_2$ and $\mathbf{Z}^n$ is an involution in terms of Eq. (9).

Due to the involution the computational effort may be reduced significantly. However, many different approaches to the evaluation of powers exist. Probably the most straightforward method (excluding the direct computation) is known as the binary method [31]. Because this method is fully explained in elementary textbooks of computational mathematics, we discuss it here only briefly.

The loop for calculating $\mathbf{C} = \mathbf{Z}^n$ consists of the following steps:

1. Initialize: Set $\mathbf{C} \leftarrow \mathbf{I}$. If $n = 0$, output $\mathbf{C}$ is the answer and one terminates the algorithm. Otherwise, set $p \leftarrow n$ and $\mathbf{D} \leftarrow \mathbf{Z}$.
2. Multiply: If p is odd, set $\mathbf{C} \leftarrow \mathbf{D} * \mathbf{C}$ and $p \leftarrow p - 1$.
3. Halve p: Set $p \leftarrow p/2$. If $p = 0$, the output is $\mathbf{C}$ and the algorithm is terminated. Otherwise, set $\mathbf{D} \leftarrow \mathbf{D} * \mathbf{D}$ and return to step 2.

This method requires the calculation of no more than $2\log_2 n + 1$ star products and is thus superior to direct computation, especially with large n. For example, with $n = 29\,999$, as in the examples given later in this paper, evaluation of only 24 star products is needed. Of course, three additional products must be calculated when combining the. remaining matrices and one more is needed to form $\mathbf{Z}$. Hence, in this case, a total of 28 star products is needed. One should notice that, by using only values $n = 2^m$, where m is an integer, the number of matrix multiplications can be further reduced remarkably.

The binary method represented here does not always give the smallest possible number of multiplications. However, usually the difference in the number of calculations between different power-raising methods is relatively small and the determination of the best available method is not a simple task. For extensive discussion of the evaluation of powers with different methods, see Ref. [32].

3. Analysis and design results

As the first example we consider the back-reflection efficiency of a SOI waveguide Bragg grating [20] as a function of the wavelength. We assume that the waveguide is silicon on silica, with refractive indices $n_g = 3.48$, $n_c = 1$ (air) and $n_s = 1.46$, respectively. The dimensions of the waveguide and the grating are as follows: width $w = 7$ μm, height $G = 10$ μm, $g = 5$ μm, period $d = 220$ nm, and filling factor $c/d = 0.5$; see Figs. 1 and 2 for the notation. In the two-dimensional approximation used here, the refractive index of the ridge part can be replaced by the effective index calculated in the transverse (y) direction. For the given dimensions $n_{\mathrm{eff}} \approx 3.4782$, i.e., very close to the refractive index of the core. The analysis is carried out for the TE-polarization of the ridge waveguide. However, one should notice that in the selected geometry the effective index of the ridge part must be calculated for TM-polarization.

In the following we will compare results of our quasi-rigorous method with the film-stack method. The latter is based on the calculation of multiple reflections and transmissions from a stack of uniform homogeneous layers, where the refractive index of each layer is the effective index of the fundamental mode in the corresponding waveguide cross-section. In the film-stack method the refractive indices of the both input and output regions are replaced by the effective index of the unmodulated waveguide. We have implemented our film-stack method as described in Ref. [33]. The results of these two methods are shown in Fig. 3 for the grating of 30 000 periods. The reflection peak of

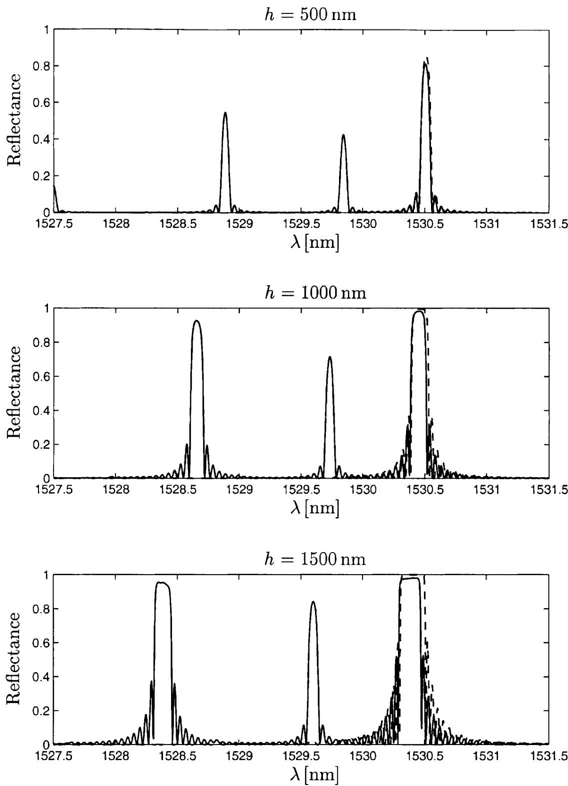

Fig. 3. Reflectances of waveguide Bragg gratings with three different etch depths h, calculated by the method presented here (solid lines) and by the thin-film stack method (dashed lines).

the fundamental guided mode is predicted very accurately by the thin-film stack method, but the efficiency of the modal method is somewhat lower because of the correctly handled losses. Moreover, the modal method predicts additional reflection peaks at shorter wavelengths. These peaks arise because of wavelength-dependent coupling of energy from the fundamental mode to higher-order modes. The wavelength of the reflected higher-order modes can be solved approximately from $\beta = (\beta_0 + |\beta_m|)/2$, where m is the number of the order and $\beta = 2\pi n_{\mathrm{eff}}/\lambda$ [27].

In addition to the above-considered relatively shallow structures we calculated reflection spectra also for strongly corrugated waveguides. As shown in Fig. 4, the difference between the modal method and the thin-film stack method is remarkable for such structures. By comparing Figs. 3 and 4 we

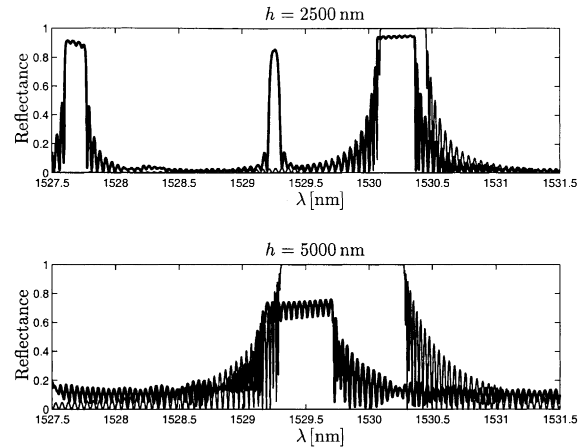

Fig. 4. Same as Fig. 3, but with deeper etch depths. Note, here thick line: presented method, thin line: thin-film stack method.

notice that the reflectance peak is shifted towards lower wavelengths when the etch depth is increased. This phenomenon originates from the fact that etching alters the average effective index of the waveguide.

In addition to the calculations mentioned above, we determined the effect of stitching errors, which typically occur in fabrication of waveguide Bragg gratings by electron beam lithography. We assumed that these errors take place with every 454th period and that they are identical to each other. In computations we can first construct one structure with the error and then multiply these basic blocks together by applying the matrix involution rule. Thus, these regular errors increase the computational effort only by few matrix multiplications. The etch depth used in these calculations was 1.5 μm. The results for two different errors, $\Delta = -10$ nm and $\Delta = +20$ nm (see Fig. 5 for notation), are illustrated in Fig. 6. By comparing Figs. 3 and 6 we immediately see that the reflectance peak of the fundamental guided mode

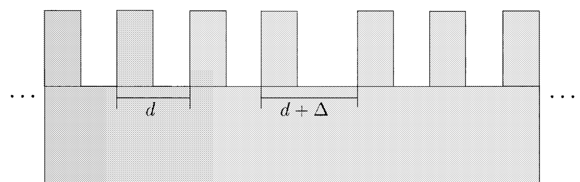

Fig. 5. Definition of the stitching error Δ used in this article.

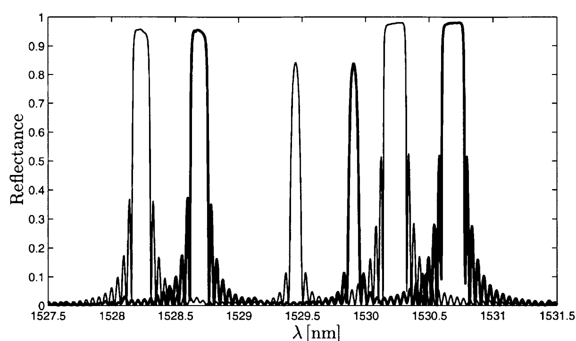

Fig. 6. Same as Fig. 3, but with stitching errors −10 nm (thin line) and +20 nm (thick line).

is shifted towards either shorter or longer wavelengths, depending on the sign of Δ.

4. Conclusions

We have presented a computationally efficient method for the analysis of corrugated waveguide structures, like Bragg gratings. The efficiency of the method is based on the possibility to apply the Redheffer's star product. By using the star product it is possible to construct the electromagnetic field transfer problem in a form of a matrix involution. This matrix involution is then solved using a so-called binary method which enables the solution of matrix involution in a basis of the powers of two. The approach reduces the computational effort of the rigorous analysis method to $\sim\log_2 N$, where N is the number of periods in a Bragg grating. The extension of the rigorous method for the analysis of the three-dimensional waveguide structures is straightforward, but mainly due to the computer memory limitations, it is not reasonable at this moment.

In this paper we have shown that the thin-film stack method gives rather accurate results when the corrugation of the waveguide is shallow. However, when the groove depth of the corrugation exceeds two tenths of the waveguide thickness, the results given by the thin-film stack method differ remarkably from the results given by the quasi-rigorous approach. One of the main benefits of the new numerical method is that it enables the analysis of coupling of light from the fundamental mode into higher-order modes. We have shown that this coupling, which occurs at shorter wavelengths than the fundamental-mode Bragg reflection, can be very strong. Thus, in wavelength-division-multiplexing systems this coupling will determine the free spectral range of the system. Furthermore, we have demonstrated that the presented quasi-rigorous method is a suitable tool for the analysis of regular, stitching type errors. Method can also be used for the analysis of other fabrication errors, like undercutting or tilted sidewalls. In these cases one has to divide a single period up into thin layers and then proceed as with the multilayer structure in rigorous diffraction problems. When the problem is solved for the single period, the star product and matrix involution can be applied as described in this paper.

Experimental work on the demonstration of the results is underway and we expect to publish characterization results of fabricated Bragg gratings on silicon waveguides elsewhere.

Acknowledgements

The authors wish to thank Lifeng Li for fruitful discussions concerning field propagation problems. Jani Tervo thanks the Emil Aaltonen Foundation and the Finnish Academy of Science and Letters for generous grants. This work was supported financially by the Academy of Finland.

References

[1] R. Ramaswami, K.N. Sivarajan, Optical Networks: A Practical Perspective, Morgan Kaufmann, San Francisco, 1997.
[2] S.T. Peng, H.L. Bertoni, T. Tamir, Opt. Commun. 10 (1974) 91–94.
[3] S.T. Peng, T. Tamir, IEEE Trans. Microwave Theory Tech. MTT-23 (1975) 123–133.
[4] A. Yariv, IEEE J. Quant. Electron. QE-9 (1973) 919–933.
[5] A. Hardy, IEEE J. Quant. Electron. QE-20 (1984) 1132–1139.
[6] S. Wang, J. Appl. Phys. 44 (1973) 767–780.
[7] P. Verly, R. Tremblay, J.W.Y. Lit, J. Opt. Soc. Am. 70 (1980) 964–968.

[8] P. Verly, R. Tremblay, J.W.Y. Lit, J. Opt. Soc. Am. 70 (1980) 1218–1221.
[9] K.A. Winick, Appl. Opt. 31 (1992) 757–764.
[10] L.A. Weller-Brophy, D.G. Hall, J. Opt. Soc. Am. A 2 (1985) 863–871.
[11] L.A. Weller-Brophy, D.G. Hall, J. Opt. Soc. Am. A 4 (1987) 60–65.
[12] G. Coppola, A. Irace, A. Cutelo, M. Iodice, Appl. Opt. 38 (1999) 1752–1758.
[13] G. Sztefka, H.-P. Nolting, IEEE Photon. Technol. Lett. 5 (1993) 554–557.
[14] G. Guekos (Ed.), Photonic Devices for Telecommunications, How to Model and Measure, Springer, Berlin, 1998, pp. 50–56.
[15] J. C̃tyroký, S. Helfert, R. Pregla, Opt. Quant. Electron. 30 (1998) 343–358.
[16] J. C̃tyroký, J. Opt. Soc. Am. A 18 (2001) 435–441.
[17] J. Shibayama, T. Takahashi, J. Yamauchi, H. Nakano, J. Lightwave Technol. 18 (2000) 427–442.
[18] B. Jalali, SPIE Proc. 2997 (1997) 60–71.
[19] M. Naydenkov, B. Jalali, Proc. 1999 IEEE International SOI Conference, 1999, pp. 56–66.
[20] J. Tidmarsh, S. Fasham, P. Stopford, A. Tomlinson, T. Bestwick, LEOS'99, IEEE Lasers and Electro-Optics Society 1999, 12th Annual Meeting, 1999, pp. 497–498.
[21] J. Turunen, Diffraction theory of microrelief gratings, in: H.P. Herzig (Ed.), Micro-Optics: Elements, Systems and Applications, Taylor & Francis, London, 1997 (Chapter 2).
[22] P. Vahimaa, J. Turunen, in: Diffractive Optics and Micro-Optics, OSA Technical Digest Series, vol. 10, Optical Society of America, Washington, DC, 1998, pp. 69–71.
[23] P. Vahimaa, M. Kuittinen, J. Turunen, J. Saarinen, R.-P. Salmio, E. Lopez Lago, J. Liñares, Opt. Commun. 147 (1998) 247–253.
[24] P. Lalanne, E. Silberstein, Opt. Lett. 25 (2000) 1092–1094.
[25] L. Li, J. Opt. Soc. Am. A 11 (1994) 2829–2836.
[26] L. Li, J. Opt. Soc. Am. A 13 (1996) 1024–1035.
[27] T. Mizunami, T.V. Djambova, T. Niiho, S. Gupta, J. Lightwave Technol. 18 (2000) 230–235.
[28] H. Kogelnik, Theory of dielectric waveguides (Chapter 2), in: T. Tamir (Ed.), Integrated Optics, Springer, Berlin, 1979, pp. 62–66.
[29] D. Jimènez, C. Ramírez, F. Pérez-Murano, A. Guzmán, Opt. Commun. 159 (1999) 43–48.
[30] R. Redheffer, Difference equations and functional equations in transmission-line theory, in: E.F. Beckenbach (Ed.), Modern Mathematics for the Engineer, McGraw-Hill, New York, 1961 (Chapter 12).
[31] B. Datta, A.N. Singh, History of Hindu Mathematics, second ed., Asia Publishing House, Bombay, 1962, pp. 75–77.
[32] D.E. Knuth, The Art of Computer Programming, vol. 2: Seminumerical Algorithms, second ed., Addison-Wesley, Reading, MA, 1981.
[33] M.G. Moharam, D.A. Pommet, E.B. Grann, T.K. Gaylord, J. Opt. Soc. Am. A 12 (1995) 1077–1086.

PUBLICATION VIII

Method for the rotational alignment of polarization-maintaining optical fibers and waveguides

In: *Optical Engineering*, Vol. 42, Issue 10, pp. 2861–2867, 2003.
© SPIE – The International Society for Optical Engineering 2003.
Reprinted with permission from the publisher.

Method for the rotational alignment of polarization-maintaining optical fibers and waveguides

Timo T. Aalto
VTT Microelectronics
P.O. Box 1208 (Tietotie 3 Espoo)
FIN-02044 VTT
Finland
E-mail: timo.aalto@vtt.fi

Mikko Harjanne
Helsinki University of Technology
Optoelectronics Laboratory
P.O. Box 3500 (Tietotie 3 Espoo)
FIN-02015 Espoo
Finland

Markku Kapulainen
VTT Microelectronics
P.O. Box 1208 (Tietotie 3 Espoo)
FIN-02044 VTT
Finland

Abstract. A novel method has been developed for measuring the rotational angle of a fiber's or a waveguide's polarization axis with respect to a reference angle. The reference angle is the polarization axis of the measuring device. The method also gives the true polarization extinction ratio of the measured fiber or waveguide. The method is suitable for the characterization and rotational alignment of polarization-maintaining waveguides and fibers. In particular, the method can be used to rotationally align the fiber-waveguide interconnections during waveguide characterization. The measuring device is either a linear polarizer or a polarization splitter that is accurately rotated with respect to the device under test. According to the experiments with a polarization-maintaining fiber, the method is very easy and inexpensive to implement, and the angular accuracy can be better than 0.2 deg. © *2003 Society of Photo-Optical Instrumentation Engineers.* [DOI: 10.1117/1.1600730]

Subject terms: optical waveguide; polarization-maintaining fiber; characterization; fiber-waveguide coupling; polarization; polarization axis; polarizer; polarization splitter.

Paper AWGE014 received Jan. 24, 2003; revised manuscript received Mar. 12, 2003; accepted for publication Mar. 24, 2003.

1 Introduction

Most of applications in optical telecommunication are based on using randomly polarized light, because the available polarization-maintaining fibers (PMFs) are clearly too expensive for long transmission links. The polarization-dependent loss (PDL) and the polarization mode dispersion (PMD) of devices are minimized to have sufficiently static operation during the polarization fluctuations that cannot be avoided in optical networks. The widely used single-mode fibers (SMFs) cannot maintain the polarization state of the light because of their negligible polarization extinction ratio (PXR). However, they have a weak birefringence that changes as a function of temperature, wavelength, and stress along the fiber. This induces time-dependent variations in both state of polarization and PMD of the fiber's output. Due to their statistical behavior, these fluctuations have a finite probability of becoming very strong.[1] When the data rates rise, the polarization problems become more difficult to handle. At very high data rates, active compensator devices can be used to eliminate the PMD caused by long fiber links.[2–4] They may also be used to stabilize the polarization to a fixed polarization state.[5]

Inside the network nodes, there are two possibilities for handling polarization problems. The devices can be made either sufficiently polarization independent or sufficiently polarization maintaining. In the former case, randomly polarized light may be used, while in the latter case, only well-defined polarization is used. In either case, it is essential to be able to accurately characterize the polarization properties of the devices.

The polarization characteristics of optical devices are often determined by using a polarization scrambler at the input, so that the maximum power variation at the output gives the PDL of the device. Reliable results require that the polarization scrambler scan the whole Poincaré sphere very densely. According to another method, the principal states of polarization (PSPs), or the polarization eigenmodes for continuous waves, are first determined from the device and input light is then coupled selectively to one PSP at a time.[4] The PDL can then be detemined as the ratio of two output powers, corresponding to the two different input polarizations. By comparing the power ratio of the two principal states of polarization at the output, one can also determine the polarization extinction ratio of the device for both input polarizations. This method is not very practical in the characterization of standard single-mode fibers and other such devices that do not have fixed principal states of polarization. However, in many other devices that have some kind of structural symmetry (see Fig. 1), the PSPs correspond to fixed linear polarization states that are identical at the input and output. This does not necessarily require a good PXR value. Such fixed principal states of polarization are referred to as the polarization modes or the polarization axes of the device, and they exist in all polarization-maintaining fibers and in many integrated optical components. In a PMF, the polarization modes lie along the so-called slow and fast axis, while in many integrated optical waveguides they lie horizontally [transverse-electric (TE) or quasi-TE mode] and vertically [transverse-magnetic (TM) or quasi-TM mode] with respect to the substrate.[3,5]

 © 2003 Society of Photo-Optical Instrumentation Engineers

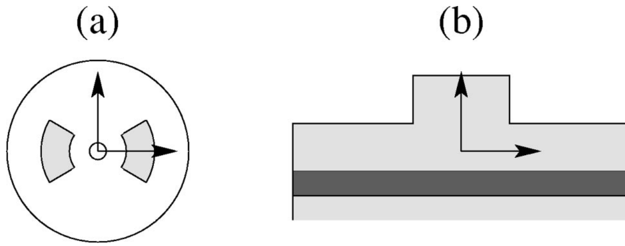

Fig. 1 Schematic cross sections of structures with fixed PSPs: (a) polarization-maintaining fiber and (b) integrated optical waveguide.

Table 1 Jones matrices of some ideal components (β_i = propagation constant, z = longitudinal coordinate, and α = rotational angle).

Fiber/waveguide	Rotational junction	Polarizer
$\begin{bmatrix} \exp(i\beta_1 z) & 0 \\ 0 & \exp(i\beta_2 z) \end{bmatrix}$	$\begin{bmatrix} \cos(\alpha) & \sin(\alpha) \\ -\sin(\alpha) & \cos(\alpha) \end{bmatrix}$	$\begin{bmatrix} \cos^2(\alpha) & \cos(\alpha)\sin(\alpha) \\ \cos(\alpha)\sin(\alpha) & \sin^2(\alpha) \end{bmatrix}$

When using polarization modes to characterize components, the input light must be carefully coupled to only one polarization mode at a time. As a PMF is typically used for input coupling, the rotational alignment between the device and the PMF input must be very accurate. Furthermore, when using different polarizing and polarization-maintaining components in any characterization, communication, or sensing systems, all the interconnections must be rotationally aligned with high precision to minimize the polarization cross talk between different polarization modes.

Several methods for the rotational alignment of a PMF have already been proposed.[6–9] They are typically based on changing the phase difference between the polarization modes continuously and by simultaneously rotating a polarizer in front of the PMF. The phase difference can be varied, e.g., by heating,[6,7] stretching, or pressing the fiber, or by tuning the wavelength.[8,9] Each of these methods requires a long piece of fiber, a long measurement time, simultaneous variation of several measurement parameters, or some complicated and expensive equipment, such as a polarization analyzer or a tunable laser. The accuracy of the methods typically varies between 0.2 and 1 deg. There are also other methods that rely on optical observation of the fiber end, but these typically have an accuracy of 1 deg or worse.

A novel method for accurate determination of rotational angles between different polarizing and polarization-maintaining components is described and demonstrated. The method is applicable to such fibers and waveguides that have fixed principal states of polarization and a finite polarization extinction ratio. When compared to earlier methods, the new method is particularly simple and inexpensive to implement.

2 Jones Matrix Theory

There are two alternative ways to analyze polarization by using matrix algebra, namely, the Stokes and Jones methods. Both of them define the states of polarization as vectors, and the polarization changes due to optical components as matrices. The Stokes vectors and the associated Müller matrices take into account both the polarized and depolarized light, while the Jones vectors and matrices can only handle polarized light. In this work, the Jones vectors and matrices are used for mathematical simplicity, but all the results can be converted into Stokes vectors and Müller matrices.[10,11]

When the Jones vectors and matrices are used, some basic assumptions and approximations are made. First, light is assumed to be fully polarized. Second, light is described only by two complex values that represent two transverse and orthogonal components of a harmonic plane wave. We assume that the PSPs of the optical components are linear polarization states, and the two complex values represent the two polarization eigenmodes, e.g., the slow and fast axis of a PMF [see Fig. 1(a)] or the TE and TM modes of a waveguide [see Fig. 1(b)]. These complex values can be represented as a Jones vector

$$\mathbf{J}=\begin{bmatrix} E_1 \exp(i\varphi_1) \\ E_2 \exp(i\varphi_2) \end{bmatrix} = E_1 \exp(i\varphi_1)\begin{bmatrix} 1 \\ \exp(i\Delta\varphi)/r \end{bmatrix}, \tag{1}$$

where $r=E_1/E_2$ is the ratio of the amplitudes E_1 and E_2, and $\Delta\varphi=\varphi_2-\varphi_1$ is the phase difference between the two polarization components. The common factor in the latter expression can be dropped out if the absolute power and the absolute phase are not relevant.

Polarization transformation caused by an optical component or a rotational junction is described by a matrix equation

$$\mathbf{J}_{\text{out}}=\mathbf{M}\mathbf{J}_{\text{in}}=\begin{pmatrix} j_{11} & j_{12} \\ j_{21} & j_{22} \end{pmatrix}\begin{bmatrix} E_{1,\text{in}} \exp(i\varphi_{1,\text{in}}) \\ E_{2,\text{in}} \exp(i\varphi_{2,\text{in}}) \end{bmatrix} = \begin{bmatrix} E_{1,\text{out}} \exp(i\varphi_{1,\text{out}}) \\ E_{2,\text{out}} \exp(i\varphi_{2,\text{out}}) \end{bmatrix}, \tag{2}$$

where $\mathbf{M}$ is the Jones matrix and subscripts "in" and "out" refer to the situation before and after a component or a junction. The Jones vectors and matrices are associated with a certain coordinate system that is aligned with respect to the polarization axes of the fiber, waveguide, or another component. Therefore, rotation of the coordinate system between different components must be carried out by using an appropriate Jones matrix. In the following, such a rotational junction is simply referred to as a junction. The Jones matrices of some ideal components are listed in Table 1.

The true PXR of light that propagates along a fiber (or a waveguide) or that comes out of the fiber is defined to be the ratio of the two amplitudes (E_1,E_2) of the Jones vector squared, and is never less than one. In relative units, PXR $=r^2(E_1\geq E_2)$ or $1/r^2(E_1\leq E_2)$, and in decibel units is

$$\text{PXR}=|20\log(E_1/E_2)|\text{dB}=|20\log(r)|\text{dB}. \tag{3}$$

In real polarization-maintaining fibers (and waveguides), the maximum PXR is typically below 35 dB due to the finite polarization cross-talk inside the fibers. However, the main limiting factor for the PXR in optical systems is the

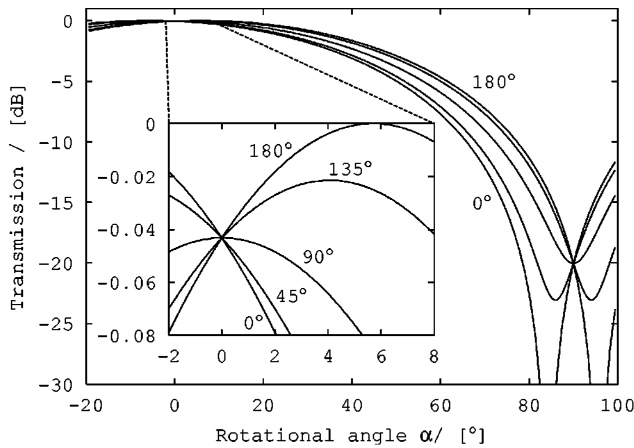

Fig. 2 Calculated transmission through an ideal polarizer when $PXR_{in} \equiv 20$ dB.

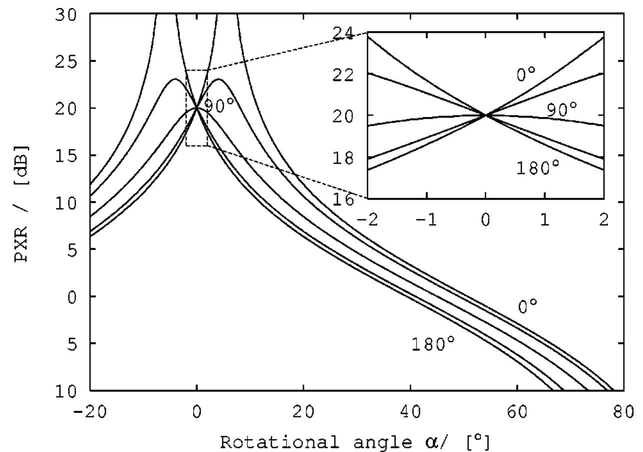

Fig. 3 Calculated PXR_{out} after a rotary joint (angle α) when $PXR_{in} \equiv 20$ dB. Each curve has a fixed phase difference (0, 45, 90, 135, or 180 deg).

polarization cross-talk caused by the rotationally misaligned junctions between the fibers (and waveguides). This can be seen by calculating the PXR change in a junction, where a polarization axis on one side of the junction has a rotational angle α with respect to a polarization axis on the other side of the junction. With a given amplitude ratio r, phase difference ($\Delta\varphi$), and angle (α), the Jones vector at the output (excluding the common factor) becomes

$$\mathbf{J}_{out} = \begin{bmatrix} \cos(\alpha) & \sin(\alpha) \\ -\sin(\alpha) & \cos(\alpha) \end{bmatrix} \begin{bmatrix} 1 \\ \exp(i\Delta\varphi)/r \end{bmatrix} = \begin{bmatrix} \cos(\alpha) + \sin(\alpha)\exp(i\Delta\varphi)/r \\ -\sin(\alpha) + \cos(\alpha)\exp(i\Delta\varphi)/r \end{bmatrix}. \quad (4)$$

The output PXR (PXR_{out}) can then be obtained as the ratio of the two output amplitudes squared. The amplitude of the first output polarization component is plotted in Fig. 2 as a normalized function of α with five different values of $\Delta\varphi$ and a fixed input PXR ($PXR_{in} \equiv 20$ dB). The result is identical with the transmission through a polarizer with an angle α. The second polarization component corresponds to a ± 90 deg rotation with respect to the first component. It can be seen from Fig. 2 that the smaller polarization component ($\alpha \approx 90$ deg) varies much more strongly with respect to α and $\Delta\varphi$ than the larger component ($\alpha \approx 0$ deg). Therefore, the smaller component dominates the dependence of PXR_{out} on α and $\Delta\varphi$ with a high PXR_{in}. With some simple algebra, the output PXR becomes

$$PXR_{out} = \left| 10 \log \left[\frac{r^2 + 2r\tan(\alpha)\cos(\Delta\varphi) + \tan^2(\alpha)}{r^2\tan^2(\alpha) - 2r\tan(\alpha)\cos(\Delta\varphi) + 1} \right] \right| \text{dB}. \quad (5)$$

In Fig. 3 the output PXR according to this formula has been plotted for a fixed input PXR ($PXR_{in} = 20$ dB) as a set of curves, so that each curve represents PXR_{out} as a function of α for a given $\Delta\varphi$. It should be noted that the plotted set of curves (not the individual curves) is symmetric and antisymmetric with respect to angles $\alpha = 0$ deg and $\alpha = 45$ deg, respectively. The set of curves has common crossing points wherever $\alpha = \pm N \cdot 90$ deg ($N = 0, 1, 2, 3$), i.e., when any two polarization axes are parallel. At the crossing points, $PXR_{out} = PXR_{in}$. It can also be seen that close to the crossing points PXR_{out} varies particularly rapidly with respect to both α and $\Delta\varphi$, and the maxima of the curves do not associate with any constant angle. With appropriate α and $\Delta\varphi$, the output PXR can be significantly higher than the input PXR. For example, with $\Delta\varphi = \pm N \cdot 180$ deg, $\alpha = \pm a\tan(1/r)$, and $r > 1$, PXR_{out} can reach infinity, corresponding to a linear polarization state. However, with appropriate $\Delta\varphi$, the output PXR may also decrease very rapidly as a function of α.

Successive junctions increase the fluctuation of the PXR_{out}, as can be seen from Fig. 4. In general, the average PXR_{out} degrades and the range of the variation increases as the number of junctions and the magnitude of the angles increase. The results in Fig. 4 are based on the assumption

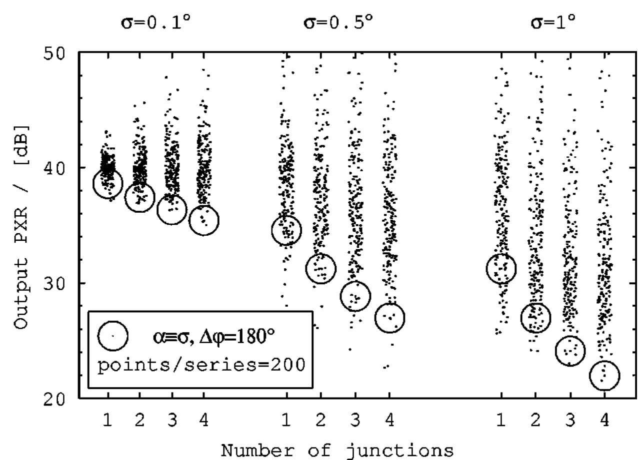

Fig. 4 Statistical analysis of PXR fluctuation after successive junctions. The misalignment (α) in each junction was varied randomly by assuming a normalized distribution and a given standard deviation (σ), while the phase difference ($\Delta\varphi$) was varied randomly in the range 0 to 360 deg. $PXR_{in} = 40$ dB before the first junction, and the number (N) of successive junctions varies from 1 to 4. Circles correspond to $\alpha \equiv \sigma$ and $\Delta\varphi \equiv 180$ deg.

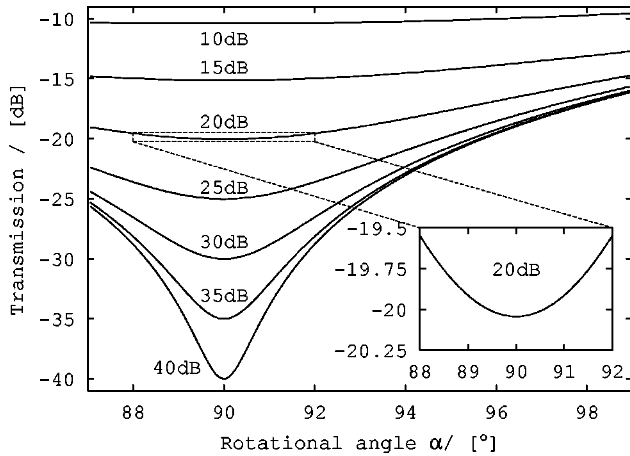

Fig. 5 Calculated transmission of broadband light through an ideal polarizer when the true PXR_{in} varies between 10 and 40 dB.

that both $\Delta\varphi$ and α vary randomly (α according to a normal distribution). The results clarify the need to minimize the misalignments in the junctions when a static and high PXR_{out} is needed.

When the rotational angle of a fiber's polarization axis is measured or optimized, it must first be defined with respect to some physical reference angle of a measuring device, e.g., the transmission or blocking direction of a linear polarizer. Therefore, this reference angle corresponds to the origin of the α scale and to one crossing point of the theoretical set of curves (see Figs. 2 and 3). In the beginning of a measurement, the angle α is unknown and a separate measurement scale (β) must be used to control the possible rotation of a measuring device with respect to the fiber. It is here defined that the origin of the α scale and the associated crossing point of the theoretical set of curves correspond to a certain crossing point angle β_{CP} on the measurement scale (β). If β_{CP} can be determined, then also the fiber's angle $\alpha=\beta-\beta_{CP}$ can be obtained and set to any desired value.

Another definition for the PXR is based on detecting the minimum and maximum transmission (P_{min},P_{max}) of a light beam through a rotated polarizer. This so called free-space PXR (PXR_{FS}) is defined as

$$PXR_{FS}=10\log(P_{max}/P_{min})\text{dB}. \tag{6}$$

As is evident from Figs. 2 and 3, this method cannot be used directly to give reliable results for the PXR or the rotational angle of a fiber, unless the effect of $\Delta\varphi$ is somehow eliminated. However, when a sufficiently broadband light source is used, $\Delta\varphi$ averages out of Eq. (5) and the results correspond to a case where $\Delta\varphi\equiv 90$ deg. This validates the use of Eq. (6) for characterizing a fiber output only when $\Delta\varphi$ averages out of the results. Theoretical curves for broadband transmission through a polarizer with different input PXRs are shown in Fig. 5.

3 Novel Method for Rotational Alignment

Due to the additional dependence of PXR_{out} on $\Delta\varphi$, the determination of PXR and the rotational angle α of a fiber is not experimentally trivial. The simple rotation of a polarizer in front of the fiber can give misleading results if $\Delta\varphi$ is unknown (see Fig. 2). Continuous rotation of a polarizer and a simultaneous scanning of $\Delta\varphi$ can point out an angle ($\alpha\approx N\cdot 90$ deg), where the dependence of PXR_{FS} on $\Delta\varphi$ is at a minimum or the minimum of $PXR_{FS}=f(\Delta\varphi)$ has a maximum. However, the continuous scanning of both α and $\Delta\varphi$ makes the measurement relatively slow, and the accuracy of the method is difficult to estimate. The whole definition of PXR for a fiber (or waveguide) is meaningful only if the PSPs are fixed, but the finding of a minimum or a maximum signal does not guarantee this.

As is shown next, Eq. (5) and the corresponding set of curves (Fig. 3) can be used to easily determine both α and PXR of a fiber (or waveguide). The basic principle of this method is that first, two or more curves, similar to those in Figs. 2 and 3, are measured by varying the measurement angle β in the junction between the fiber and the measuring device. Then the crossing point of the measured curves is determined. This point directly corresponds to β_{CP} and the PXR value of the fiber (PXR_{in}, before the junction). Transitions between different curves are done by somehow changing the phase difference $\Delta\varphi$ of the fiber's output. One advantage of the new method is that one does not need to know $\Delta\varphi$ or to continuously vary it. It is sufficient to induce such changes in $\Delta\varphi$ that at least two measured curves are clearly different. These changes can be realized either by modifying the light guiding properties of the fiber or by tuning the wavelength. The former can be easily done by heating, stretching, or pressing the fiber.

Transmission curves (Fig. 2) can be measured by rotating a polarizer in front of the fiber end. PXR_{out} curves can be obtained by calculating the ratio of transmissions in perpendicular angles (β, $\beta\pm 90$ deg). Alternatively, the PXR_{out} curves can be directly measured by calculating the ratio of two output powers that originate from a rotatable polarization splitter.

The measured curves are not identical with the theoretical curves because of the finite accuracy in optical power and angle (β) measurements, the instabilities of the fiber and the measurement system, the depolarized fraction of light, the finite bandwidth of the light, and the wavelength fluctuations. Therefore, the position of the crossing point may not be explicitly determined. There are several possibilities for postprocessing the results. One may fit the theoretical set of curves to the results, or one may also fit each curve individually by just assuming a fixed crossing point angle β_{CP} and taking into account the possible PXR fluctuations. Also, the measured points can all be connected with interpolated curves. This typically produces several crossing points, and β_{CP} can then be obtained by appropriately averaging them. The measurement error in both α and PXR can be estimated based on the quality of fitting or the variation between the different crossing points. In both cases, the measurement accuracy for β_{CP} can be clearly better than the angular spacing between individual measurement points, unlike in many alternative methods.

4 Results

The functionality of the new method was demonstrated by measuring the angle of a polarization-maintaining fiber's polarization axis with respect to the blocking direction of a

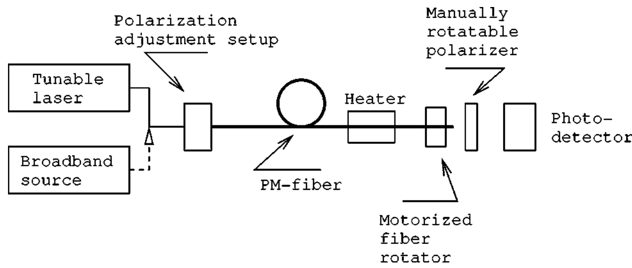

Fig. 6 Schematic layout of the measurement setup.

thin film near-infrared polarizer. The extinction ratio of the polarizer is better than 40 dB around the 1550-nm wavelength. The measured fiber is used as an incoupling fiber in a waveguide characterization setup, so a succesful fiber alignment can be readily exploited in waveguide measurements. Due to the flatness of the waveguide chips, they can be easily aligned with respect to the calibrated angle of the polarizer.

The experimental setup for measuring the fiber is shown in Fig. 6. Light is launched either from a narrowband laser ($\lambda = 1550$ nm) or a broadband LED into a 7-m-long polarization-maintaining fiber (PANDA) via a polarization-adjustment setup. The polarization and power of the light that couples into the fiber can be controlled and stabilized. The light, originating from the bare output end of the fiber, is guided through the manually rotatable polarizer to a photodetector. The line grid of the measurement scale was as high as 2 deg and, therefore, the relative accuracy of the first angle readings was only 0.5 deg. However, to obtain more accurate results, a motorized fiber rotator was constructed to turn the fiber with respect to the polarizer. This improved the accuracy in the last measurements down to 0.05 deg. Before starting the actual measurements, the polarization axes at the output of the fiber were determined coarsely by rotating the polarizer (or the fiber) and maximizing PXR_{FS} with the laser source. Then the accurate angle was determined by measuring sets of curves and locating the crossing points. The phase was varied either by changing the wavelength, by simply moving the fiber on a table, or by heating an approximately 8-cm-long piece of the fiber.

When using wavelength tuning, it was found that only a 1-nm wavelength step is sufficient to cause a 2π phase difference. The required wavelength change is so small that the wavelength dependences of the polarizer and the polarization-adjustment setup do not affect the results. Figure 7 shows both the measured PXR_{out} values and the theoretical curves that are based on Eq. (5) and fitted to the results. The fiber's PXR (PXR_{in}) and the crossing-point angle β_{CP} were used as common fitting paremeters, while $\Delta\varphi$ was fitted separately for each curve. As can be seen from Fig. 7, the theoretical curves and measurement results agree very well. The accuracy of the results is limited by the coarse measurement scale of the manually rotated polarizer. The final accuracy of β_{CP} is slightly better than the 0.5 deg accuracy of the individual angle readings, because an appropriate curve fitting can partially average out the angle reading errors. This was verified by monitoring the fitting quality, while β_{CP} was slightly varied around its optimally fitted value. Detuning β_{CP} by ± 0.5 deg evidently degraded the fitting quality. The accuracy was also successfully confirmed by connecting the measured points with straight lines and by checking that the angular variation between different crossing points was below 0.5 deg.

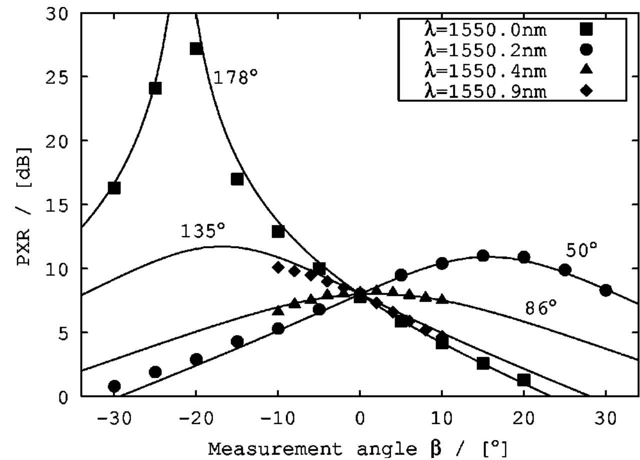

Fig. 7 Measurement results and fitted theoretical curves obtained by wavelength tuning.

The phase difference $\Delta\varphi$ was also tuned by simply moving the fiber on a table. Changing the direction or the amount of the loose fiber loops was sufficient to induce significant phase changes. Movements are also expected to cause slight variation in the PXR value. The phase change does not stabilize immediately after the movements, because the fiber loops experience microscopic movements after repositioning. Therefore, the measured curves, shown in Fig. 8, do not correspond to fully stabilized phase differences and a common PXR. The measurement accuracy is again better than 0.5 deg, and is mainly limited by the accuracy of the rotational scale. This was verified with the same principles as in the case of wavelength tuning.

Heating and motorized rotation of the fiber was found to be the most accurate measurement method. Figure 9 shows PXR_{out} as a function of β with different temperatures when the motorized fiber rotator was used. Only a couple of degrees temperature change is enough to change $\Delta\varphi$ signifi-

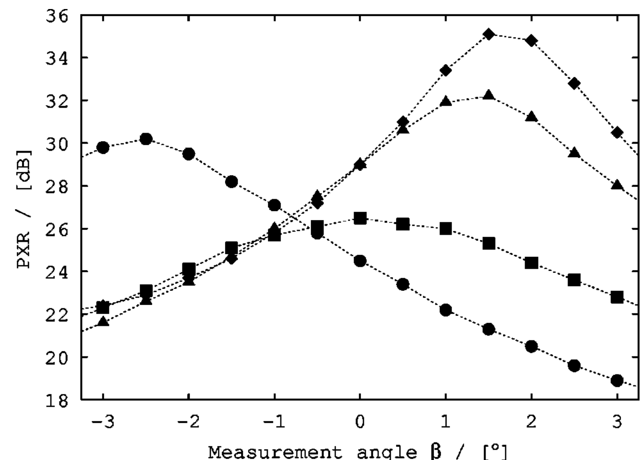

Fig. 8 Measurement results obtained by moving the fiber.

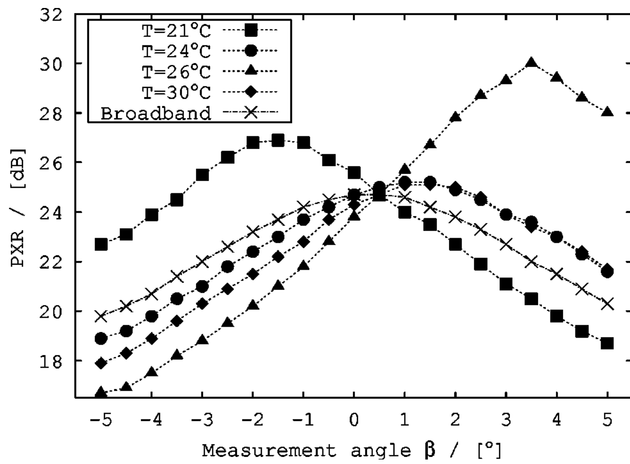

Fig. 9 Measurement results obtained by heating the fiber (filled symbols) and by using a broadband light source (thin crosses). Coarse angle variation.

cantly. Based on the results, the fiber angle was corrected toward the origin of the β scale, and a second set of curves was measured with a finer angular grid. This set of curves is shown in Fig. 10. In both cases, the measurements were carried out at four different temperatures. Based on Fig. 10 and the same criteria as with the previous phase tuning methods, the accuracy of β_{CP} is estimated to be better than 0.2 deg. For comparison, the measurement of each set of curves (Figs. 9 and 10) was followed by a PXR_{FS} measurement. In this procedure, a PXR_{out} curve was measured by using the broadband light source. These results agree well with the new method.

5 Conclusions

The best way to maintain a stable and sufficiently high PXR in a polarization-maintaining optical system is to use highly linear input polarization and very accurately aligned rotational junctions. The required rotational accuracy depends on the number of junctions, the polarization cross-talk induced by the components themselves, the required minimum PXR, and the tolerable PXR fluctuation. For most applications, the accuracy should be better than 0.5 deg, but for some applications the improvement of accuracy down to 0.1 deg is justified.

A novel method for the rotational alignment of polarization-maintaining fibers is presented and demonstrated. The best results are obtained by heating the fiber and by using a motorized fiber rotator. The measurement accuracy is better than 0.2 deg. Also, λ tuning and mechanical movement of the fiber are used to change the phase difference, but these methods were somewhat less accurate (0.5 deg). This is mostly due to the poor rotation accuracy (0.5 deg) of the manually rotated polarizer used in these measurements. By using curve fitting, the final results can be slightly better than the rotation accuracy.

The new method can be readily used in waveguide characterization, where the PMF must be carefully aligned with an integrated optical waveguide. It should also be possible to apply the method to the direct measurement of a waveguide's rotational angle. However, this would require a motorized rotation of the polarizer, because the manual polarizer rotation is less accurate than the straightforward alignment by using a rotationally calibrated flat plate under the chip. For short waveguides, a large amount of wavelength tuning is necessary, and this requires a stable input PXR with respect to λ. When heating a waveguide chip, the

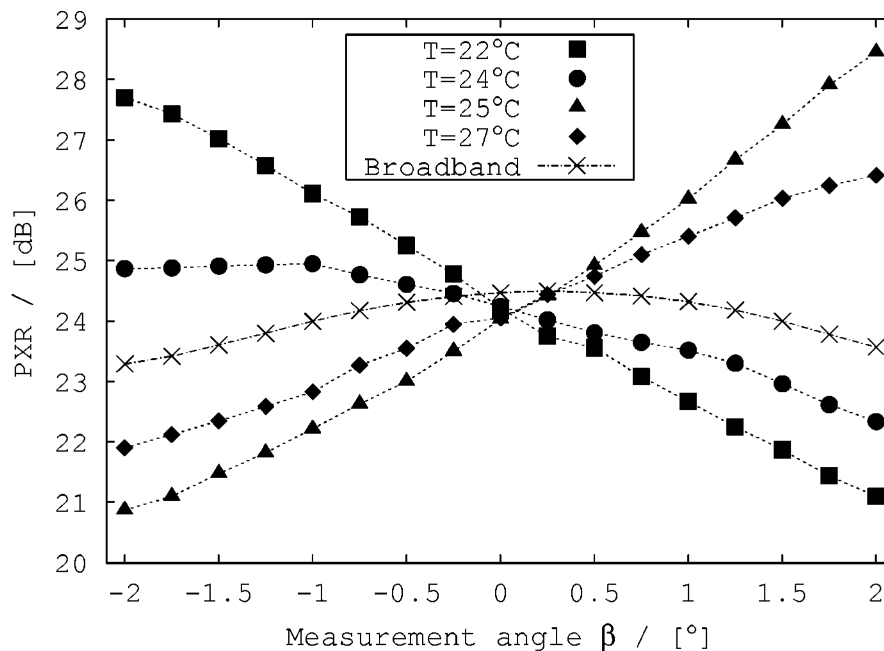

Fig. 10 Measurement results obtained by heating the fiber (filled symbols) and by using a broadband light source (thin crosses). Fine angle variation after angle adjustment.

stability of the input coupling also requires special attention.

Acknowledgments

The authors thank Markku Rönö for his assistance in the work and Jouni Nygård for building the motorized fiber rotator.

References

1. D. Wang and C. R. Menyuk, ''Calculation of penalties due to polarization effects in a long-haul WDM system using a Stokes parameter model,'' *J. Lightwave Technol.* **19**(4), 487–494 (2001).
2. N. Kikichi, ''Analysis of signal degree of polarization degradation used as control signal for optical polarization mode dispersion compensation,'' *J. Lightwave Technol.* **19**(4), 480–486 (2001).
3. F. Heismann, ''Integrated-optic polarization transformer for reset-free endless polarization control,'' *IEEE J. Quantum Electron.* **25**(8), 1898–1906 (1989).
4. H. Sunnerud, C. Xie, M. Karlsson, R. Samuelson, and P. A. Andrekson, ''A comparison between different PMD compensation techniques,'' *J. Lightwave Technol.* **20**(3), 368–378 (2001).
5. W.-Y. Hwang, M.-C. Oh, H. Park, J.-H. Ahn, S. G. Han, and H.-G. Kim, ''Polarization stabilizer using a polarization splitter and a thermooptic polymer waveguide device,'' *IEEE Photonics Technol. Lett.* **10**(12), 1736–1738 (1998).
6. N. Caponio and C. Svelto, ''A simple angular alignment technique for a polarization-maintaining-fibre,'' *IEEE Photonics Technol. Lett.* **6**(6), 728–729 (1994).
7. G. R. Walker and N. G. Walker, ''Alignment of polarization-maintaining fibres by temperature modulation,'' *Electron. Lett.* **23**(13), 689–691 (1987).
8. A. Ebberg and R. Noe, ''Novel high precision alignment technique for polarization maintaining fibres using a frequency modulated tunable laser,'' *Electron. Lett.* **26**(24), 2009–2010 (1990).
9. Y. Ida, K. Hayashi, M. Jinno, T. Horii, and K. Arai, ''New method for polarization alignment of birefringent fibre with laser diode,'' *Electron. Lett.* **21**(1), 18–21 (1985).
10. S.-M. F. Nee, ''Depolarization and principal Müller matrix measured by null ellipsometry,'' *Appl. Opt.* **40**(28), 4933–4939 (2001).
11. D. S. Kliger, J. W. Lewis, and C. E. Randall, *Polarized Light in Optics and Spectroscopy*, Academic Press, Inc., New York (1997).

Timo Aalto received his MSc degree in physics from the Helsinki University of Technology (HUT) in 1998. His major was optoelectronics and he is now doing his PhD studies around the same subject. He has worked at the VTT Center for Microelectronics since 1997. His research interests are the design, simulation, fabrication, and characterization of silicon-based waveguides, and especially silicon-on-insulator waveguides.

Mikko Harjanne received his MSc degree from Helsinki University of Technology (HUT) in 2003, his major being optoelectronics. Since his graduation he has worked at the Optoelectronics Laboratory at HUT.

Markku Kapulainen received his MSc degree in physics from the Helsinki University of Technology (HUT) in 2001. He has worked at the VTT Center for Microelectronics since 2001.

Published by

VTT

Series title, number and report code of publication

VTT Publications 553
VTT–PUBS–553

Author(s)
Aalto, Timo

Title

Microphotonic silicon waveguide components

Abstract

This thesis describes the design, simulation, fabrication and characterisation of microphotonic silicon waveguide components on silicon-on-insulator (SOI) substrates. The focus is on approximately 10 µm thick and single-moded (SM) silicon rib waveguides. In particular, simulation results are given for straight and bent Si waveguides, directional couplers (DCs), thermo-optically (TO) modulated Mach–Zehnder interferometers (MZI), and waveguide gratings. A new analytical SM condition for Si rib waveguides is proposed and the development of a new grating simulation algorithm is reported. The theoretical part of the work also involves inventions relating to multi-step patterning of Si waveguides, modulation of interferometric devices, and measurement of polarisation axes from waveguides and polarisation maintaining (PM) fibers.

Clean room processing of waveguide chips is briefly described. Main process steps are photolithography, electron-beam lithography, thermal oxidation, oxide deposition, oxide dry etching and Si dry etching. Post-processing of the chip is also reported, including dicing, polishing, anti-reflection (AR) coating, fiber pigtailing and wire bonding. The development of fabrication processes for multi-step patterning, waveguide gratings and photonic crystal waveguides is reported, although the optical characterisation of devices based on these three processes is not included in the thesis.

Experimental results are given for Si rib waveguides with different thicknesses (H) and widths (W). The minimum fiber coupling loss with H = 9 µm was 1.3 dB/facet without an AR coating. The AR coating reduced the coupling loss by 0.7–0.8 dB/facet. Minimum propagation loss for a 114 cm long waveguide spiral with H = 9 µm and W = 7 µm was 0.13 dB/cm. With H = 9 µm, the birefringence varied from 0.00063 to <0.0001 depending on the cladding material, and the maximum polarisation extinction ratio for straight waveguides and directional couplers was >15 dB. Furthermore, fast modulation with 15 dB extinction ratio (ER) is reported for TO MZI switches by using both traditional (10 kHz) and novel (167 kHz) modulation methods. Rise and fall times for single switching operations were pushed below 750 ns with 9 dB ER. The setups and methods used in measurements are described in detail, including a novel method for measuring the polarisation axes of waveguides and PM fibers.

Keywords
silicon microphotonics, integrated optics, silicon-on-insulator waveguides, SOI waveguides, waveguide bends, thermo-optical switching, multi-step patterning, polarisation maintaining fibers, polarisation extinction ratio

Activity unit
VTT Information Technology, Tietotie 3, P.O.Box 1208, FIN–02044 VTT, Finland

ISBN			Project number
951–38–6422–7 (soft back ed.) 951–38–6423–5 (URL: http://www.vtt.fi/inf/pdf/)			T3SU00354
Date	Language	Pages	Price
November 2004	English	78 p. + app. 73 p.	D

Series title and ISSN
VTT Publications
1235–0621 (soft back ed.)
1455–0849 (URL: http://www.vtt.fi/inf/pdf/)

Sold by
VTT Information Service
P.O.Box 2000, FIN–02044 VTT, Finland
Phone internat. +358 9 456 4404
Fax +358 9 456 4374

The first demonstrations of silicon transistors around 1950 started the Silicon Age, the successor of the Iron Age. Presently, microelectronic silicon chips exist inside almost every modern electronic product, thus forming the backbone of e.g. Internet and mobile communications. The realisation of optical functions on silicon chips is known as silicon microphotonics. It is an emerging technology that can improve the performance of micro-electronic chips and enable the inexpensive mass production of optical components for numerous applications. It is still far from the maturity of silicon microelectronics, but it has recently gained a lot of interest due to some promising results reported for e.g. light emission and fast modulation based on silicon. This thesis gives an introduction to this fascinating field and describes the development of microphotonic silicon waveguide components at VTT since 1997. The work includes theory, simulations, clean room fabrication, post-processing and device characterisation. Several innovations and some world-class results are reported.

Tätä julkaisua myy
VTT TIETOPALVELU
PL 2000
02044 VTT
Puh. (09) 456 4404
Faksi (09) 456 4374

Denna publikation säljs av
VTT INFORMATIONSTJÄNST
PB 2000
02044 VTT
Tel. (09) 456 4404
Fax (09) 456 4374

This publication is available from
VTT INFORMATION SERVICE
P.O.Box 2000
FIN–02044 VTT, Finland
Phone internat. +358 9 456 4404
Fax +358 9 456 4374

ISBN 951–38–6422–7 (soft back ed.)
ISSN 1235–0621 (soft back ed.)

ISBN 951–38–6423–5 (URL: http://www.vtt.fi/inf/pdf/)
ISSN 1455–0849 (URL: http://www.vtt.fi/inf/pdf/)

Timo Aalto